

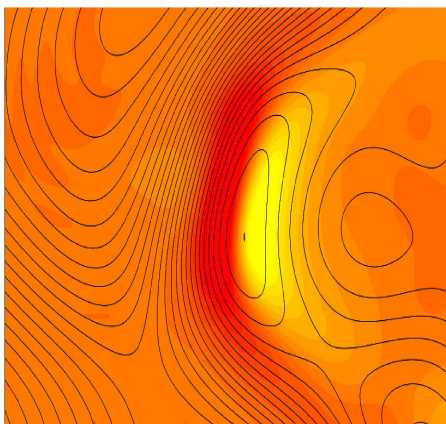
UNIVERSITÀ DEGLI STUDI DI UDINE



DOTTORATO DI RICERCA IN  
SCIENZE DELL'INGEGNERIA ENERGETICA E AMBIENTALE  
XXX CICLO - 2018

# Analysis of drag reduction in viscosity stratified turbulent channel flows

Dr. Somayeh Ahmadi



## BOARD MEMBERS

---

Prof. Roberto MAURI	REVIEWER
Prof. Ruud HENKES	REVIEWER
Prof. Cristian MARCHIOLI	COMMITTEE MEMBER
Prof. Matteo BERNARDINI	COMMITTEE MEMBER
Prof. Srdjan SASIC	COMMITTEE MEMBER
Prof. Alfredo SOLDATI	SUPERVISOR
Dr. Francesco ZONTA	CO-SUPERVISOR

---

Prof. Alessandro TROVARELLI	DOCTORATE CHAIR
-----------------------------	-----------------

---

Author's Web Page:

<http://calliope.dem.uniud.it/>

Author's e-mail:

[ahmadi.somayeh@spes.uniud.it](mailto:ahmadi.somayeh@spes.uniud.it)

Author's address:

Dipartimento Politecnico di Ingegneria e Architettura

Università degli Studi di Udine

Via delle Scienze, 206

33100 Udine – Italia

mobile: +39 366 5024577

web: [www2.diegm.uniud.it/diegm/](http://www2.diegm.uniud.it/diegm/)

---

Cover picture:

Contour plot of the third term of the flow field divergence,  $\partial w / \partial z^+$

black lines are iso-contours of the interface wave elevation

located in the nearby of the wall.

---

Last update:

Udine, February 7, 2018

---

# Acknowledgments

First of all, I would like to express my sincere gratitude to my advisor, Prof. Alfredo Soldati for the opportunity to work on such an exciting project. His guidance and patience provided the right atmosphere in order for me to explore my interests while producing high-quality research. The help of Dr. Francesco Zonta was also greatly appreciated, his attitude to science and discussion with him always brings me wisdom. I am indebted to colleagues of the Lab, for their support.

This is the best time of life, this is the worst time of life with a lot of struggles at the moment of final achievement of my Ph.D, without love and support from my parents I could have never survived from them.

CINECA Supercomputing Centre (Bologna, Italy) is also gratefully acknowledged for generous allowance of computer resources.



---

# Abstract

In this work we study the turbulence modulation in a viscosity-stratified two-phase flow using Direct Numerical Simulation (DNS) of turbulence and the Phase Field Method (PFM) to simulate the interfacial phenomena. Specifically we consider the case of two immiscible fluid layers driven in a closed rectangular channel by an imposed mean pressure gradient. The present problem, which may mimic the behaviour of an oil (fluid 2) flowing under a thin layer of different oil (fluid 1), thickness ratio  $h_2/h_1 = 9$ , is described by three main flow parameters: the shear Reynolds number  $Re_\tau$  (which quantifies the importance of inertia compared to viscous effects), the Weber number  $We$  (which quantifies surface tension effects) and the viscosity ratio  $\lambda = \nu_1/\nu_2$  between the two fluids. For this first study, the density ratio of the two fluid layers is the same ( $\rho_2 = \rho_1$ ), we keep  $Re_\tau$  and  $We$  constant, but we consider three different values of the viscosity ratio:  $\lambda = 1$ ,  $\lambda = 0.875$  and  $\lambda = 0.75$ . Compared to a single phase flow at the same shear Reynolds number ( $Re_\tau = 100$ ), in the two phase flow case we observe a decrease of the wall-shear stress associated with a substantial increase of the volume-flowrate and a strong turbulence modulation in particular in the proximity of the interface. Interestingly, we observe that the modulation of turbulence by the liquid-liquid interface extends up to the top wall (i.e. the closest to the interface) and produces local shear stress inversions and flow recirculation regions. The observed results depend primarily on the interface deformability and on the viscosity ratio between the two fluids ( $\lambda$ ). The investigations in this thesis are also for the the case of capillary wave turbulence to describe Weak Turbulence Theory (WTT) from both theoretical and computational considerations.



---

# Contents

<b>1</b>	<b>Introduction</b>	<b>1</b>
1.1	Motivation . . . . .	1
1.1.1	Viscosity stratification and drag reduction . . . . .	2
1.2	Object of the thesis . . . . .	3
1.2.1	Thesis layout . . . . .	4
<b>2</b>	<b>Methodology</b>	<b>7</b>
2.1	Interface Representation . . . . .	7
2.2	Diffuse and sharp-interface methods . . . . .	9
2.2.1	Phase Field Method . . . . .	10
2.2.2	Gizburg-Landau free energy functional . . . . .	11
2.2.3	Mass conservation . . . . .	15
2.3	The incompressible Navier-Stokes equations . . . . .	15
2.4	Geometry . . . . .	16
2.4.1	Dimensional analysis . . . . .	17
2.4.2	Wall units . . . . .	19
<b>3</b>	<b>Numerical method</b>	<b>21</b>
3.1	Introduction to pseudo spectral method . . . . .	21
3.1.1	Chebyshev pseudospectral Method . . . . .	22
3.2	Numerical Procedure . . . . .	22
3.2.1	Velocity-vorticity formula . . . . .	22
3.3	Cahn-Hilliard equation discretization . . . . .	24
3.3.1	Stability of Cahn Hilliard equation . . . . .	24
3.4	Spectral discretization . . . . .	26
3.5	Discretization and solution of the equations . . . . .	28
3.5.1	Velocity equation . . . . .	28
3.5.2	Vorticity equation . . . . .	32
3.6	Cahn-Hilliard equation . . . . .	32
3.6.1	Simulation parameters and accuracy . . . . .	34
<b>4</b>	<b>Results and Discussion</b>	<b>37</b>
4.1	Benchmark . . . . .	37
4.1.1	Analytical solution for capillary wave . . . . .	38

4.1.2	Non-viscous and viscous fluids . . . . .	39
4.1.3	Test case . . . . .	40
4.2	Turbulent drag reduction . . . . .	42
4.2.1	Numerical Simulation . . . . .	43
4.2.2	Turbulence statistics . . . . .	45
4.2.3	Flow rate . . . . .	45
4.2.4	Mean streamwise velocity profile . . . . .	46
4.2.5	Rms statistics . . . . .	49
4.2.6	Strain rate . . . . .	51
4.2.7	Reynolds stress . . . . .	52
4.2.8	Total shear stress without capillary tensor . . . . .	52
4.2.9	Spanwise vorticity . . . . .	54
4.3	Turbulence Near-wall region . . . . .	55
4.3.1	Boundary layer separation . . . . .	56
4.3.2	Flow near line of separation . . . . .	57
4.3.3	Waves and shear stress at walls . . . . .	60
4.3.4	Near wall Mechanism . . . . .	60
4.3.5	Instantaneous profiles and distributions . . . . .	64
4.3.6	Correlation between the interface deformation and the shear stress . . . . .	69
4.4	Wave turbulence . . . . .	72
4.4.1	Dimensional derivation of capillary wave . . . . .	72
4.5	Wave growth . . . . .	74
4.5.1	WTT of capillary waves . . . . .	74
4.5.2	Spatial spectrum . . . . .	75
4.6	Conclusions . . . . .	79
<b>5</b>	<b>Conclusions and future work</b>	<b>81</b>
<b>A</b>	<b>Appendix A</b>	<b>83</b>
A.1	Aliasing errors . . . . .	83
<b>B</b>	<b>Publications, courses and projects</b>	<b>87</b>
B.1	Referred Journals . . . . .	87
B.2	Referred Conferences . . . . .	87
B.3	Advanced Courses . . . . .	88
	<b>Bibliography</b>	<b>89</b>

---

# List of Figures

2.1	Concentration profile across the diffused interface region with the thickness $\xi$ , (interface located between: $-0.9 < \frac{\phi}{\phi_+} < 0.9$ ).	10
2.2	Regular solution model for free energy . . . . .	13
2.3	Sketch of the computational domain. A thin liquid layer with viscosity $\nu_1$ flows on top of a thicker liquid layer with viscosity $\nu_2$ . . . . .	17
4.1	Initial conditions for the liquid-liquid interface $\eta(x, 0)$ . . . . .	38
4.2	Capillary wave test case in $(z - y)$ plane ; a): Initial position of interface ; b): Computed amplitude of capillary wave, simulation versus linear theory. . . . .	41
4.3	Sketch of the computational domain with details of the flow configuration. A thin liquid layer with smaller viscosity (fluid 1) flows on top of a thick liquid layer with larger viscosity (fluid 2). The thickness ratio between the two liquid layers is $h_2/h_1 = 9$ . The distribution of Turbulent Kinetic Energy (TKE) and the deformed liquid-liquid interface are also shown for visualization purposes. . . . .	43
4.4	Time evolution of the volume flowrate $Q$ , normalized by the reference volume flowrate for the single phase flow $Q_{SP}$ , for the viscosity stratified liquid-liquid flow at $Re_\tau = 100$ and different viscosity ratios $\lambda$ : $\lambda = 1$ , $\lambda = 0.875$ and $\lambda = 0.75$ . The arrow points in the direction of decreasing $\lambda$ (i.e. increasing of the viscosity difference between the two fluid layers). . . . .	46
4.5	Mean fluid streamwise velocity $\langle u_x \rangle$ for the viscosity stratified liquid-liquid flow at $Re_\tau = 100$ . Comparison between simulations at different viscosity ratios $\lambda$ : $\lambda = 1$ ( $-\nabla-$ ), $\lambda = 0.875$ ( $-\square-$ ) and $\lambda = 0.75$ ( $-\circ-$ ) Results from simulation of single phase flow at the same reference shear Reynolds number (SP, $-$ ) are also included for comparison. . . . .	48
4.6	Curvature of the mean fluid streamwise velocity, $\partial^2 \langle u_x \rangle / \partial z^2$ for the viscosity stratified liquid-liquid flow at $Re_\tau = 100$ . Lines as in Fig. 4.5. . . . .	48

- 4.7 Root mean square of fluid velocity fluctuations,  $\langle u'_{i,rms} \rangle$ , for the viscosity stratified liquid-liquid flow at  $Re_\tau = 100$ : a) streamwise component,  $\langle u'_{x,rms} \rangle$ ; b) spanwise component,  $\langle u'_{y,rms} \rangle$ , a) wall-normal component,  $\langle u'_{z,rms} \rangle$ . Lines as in Fig. 4.5. . . . . 50
- 4.8 Wall-normal behavior of the mean strain rate,  $\gamma_{xz} = \partial \langle u_x \rangle / \partial z$  for the viscosity stratified liquid-liquid flow at  $Re_\tau = 100$ . Lines as in Fig. 4.5. . . . . 51
- 4.9 Wall-normal behavior of the Reynolds stress,  $\langle u'_x \rangle \langle u'_z \rangle$  for the viscosity stratified liquid-liquid flow at  $Re_\tau = 100$ . Lines as in Fig. 4.5. . . . . 52
- 4.10 a) Wall-normal behaviour of the shear stress (without Korteweg stress),  $\langle u'_x u'_z \rangle + \lambda \frac{\partial \langle u_x \rangle}{\partial z}$  for the viscosity stratified liquid-liquid flow, lines as in Fig. 4.5; b) Wall-normal behaviour of the viscous shear stress (yellow-dashed line),  $\lambda \frac{\partial \langle u_x \rangle}{\partial z}$ , and the mean strain rate (Solid line),  $\frac{\partial \langle u_x \rangle}{\partial z}$ ,  $\lambda = .875$ ; c) Wall-normal behaviour of the viscous shear stress (yellow-dashed line),  $\lambda \frac{\partial \langle u_x \rangle}{\partial z}$ , and the mean strain rate (Solid line),  $\frac{\partial \langle u_x \rangle}{\partial z}$ ,  $\lambda = 0.75$ : at  $Re_\tau = 100$ . . . . . 53
- 4.11 Contour maps of the spanwise vorticity  $\langle \omega_y \rangle$  for the viscosity stratified liquid-liquid flow at  $Re_\tau = 100$  and different viscosity ratio  $\lambda$ . Panels: a) Single Phase flow; b) liquid-liquid flow at  $\lambda = 1$ ; c) liquid-liquid flow at  $\lambda = 0.875$ ; d) liquid-liquid flow at  $\lambda = 0.75$ . The location of the interface is explicitly indicated (thin black line) for clarity. . . . . 54
- 4.12 Schematic diagram of the self-sustaining cycle [35] . . . . . 56
- 4.13 Velocity profile in the boundary layer over a covered surface, last profile represents reverse flow which is related to separated flow. . . . . 58
- 4.14 Snapshots of the instantaneous liquid-liquid interface for elevation and shear stress at top and bottom wall: a) interface elevation; b) shear stress at top wall; c) shear stress at bottom wall at a given time instant ( $t^+ = 1825$ ), (black line are related to negative and red line are for positive value, respectively). . . . . 61
- 4.15 Probability Density Function (PDF) of the normalised wall shear stress fluctuation  $\tau'_w = (\tau_w - \langle \tau_w \rangle) / \langle \tau_w \rangle$  for all the simulated cases. Panel a) refers at the bottom wall ( $z^+ = 0$ ) while the panel b) refers at the top wall ( $z^+ = 200$ ). The profile for the two phase cases (resp. single phase case) are shown with symbols (resp. solid line). . . . . 62

- 4.16 Probability Density Function (PDF) of the interface elevation  $\eta^+$  for all the simulated cases (different values of  $\lambda$ ). . . . . 64
- 4.17 Panel a): Instantaneous wall shear stress distribution  $\tau_w$  at the top wall ( $z^+ = 200$ ) computed at  $t^+ = 3650$  for the simulation with  $\lambda = 1$ . Red regions identify positive areas of shear stress, i.e. opposite to the direction of the mean stress at that wall ( $\langle \tau_w \rangle < 0$ ). Panel b): detailed inspection of the shear stress distribution in the square region A-A identified in panel a). Panels c-d): Streamwise distribution of the shear stress (panel c) and of the interface elevation (panel d) computed at  $y^+ = 175$ . . . . . 65
- 4.18 Instantaneous flow streamlines corresponding to the region labelled A-A in Fig. 4.17a). The  $x^+ - y^+$  plane is located close to the top wall, at  $z^+ = 199.5$ . Contour maps of the streamwise velocity are also shown: red regions correspond to regions of negative streamwise velocity (flow recirculation) whereas yellow regions correspond to regions of positive streamwise velocity. . . . . 66
- 4.19 Instantaneous flow streamlines corresponding to the region labelled B-B in Fig. 4.17. The  $x^+ - z^+$  plane is located at  $y^+ = 175$ . Contour maps of the streamwise velocity are also shown: red regions correspond to regions of negative streamwise velocity (flow recirculation) whereas yellow regions correspond to regions of positive streamwise velocity. Note that the position of the interface is explicitly indicated by the solid black line. . . . . 67
- 4.20 Contour plot of the two dimensional flow divergence,  $\nabla_{2D} = -\frac{\partial u_z^+}{\partial z^+}$  for the square area labelled A-A indicated in Fig. 4.17. The horizontal slice is located at  $z^+ = 199.5$ . Red regions identify upwellings while yellow regions identify downwellings. Contour lines (solid black lines) of the interface elevation  $\eta^+$  are also shown for comparison. . . . . 68

- 4.21 Instantaneous profiles of the streamwise velocity along the  $z^+$  direction. The red line show an instantaneous streamwise velocity profile at  $x^+ = 630$  and  $y^+ = 175$  along the  $z^+$  direction, wall shear stress at the top wall ( $z^+ = 200$ ) are negative and  $u_x > 0$  across all the channel. By opposite black line show the instantaneous velocity profile at  $x^+ = 430$  and  $y^+ = 175$ , wall shear stress at the top wall are positive, a recirculation phenomena is present and in a small portion of the  $z^+$  axis  $u_x < 0$ . . . . . 69
- 4.22 Joint Probability Density Function (PDF) between the normalized interface deformation  $\eta^+/\eta_{max}^+$  and the corresponding shear stress deviation  $\tau_w' = (\tau_w - \langle \tau_w \rangle)/\langle \tau_w \rangle$ . Panel a) refers to the top wall ( $z^+ = 200$ , i.e. close to the interface). Panel b) refers to the bottom wall ( $z^+ = 0$ , i.e. far from the interface). . . . . 71
- 4.23 Time evolution of the  $\eta_{rms} = \langle \eta(t) \rangle^{1/2}$  for the simulation  $\lambda = 1.0$  (black line), initial stage wave growth as a linear function of  $t$  (dashed line). . . . . 75
- 4.24 Two dimensional wavenumber spectrum  $E(k_x, k_y, t)$  for one time snapshot: at time  $t^+ = 1850$  for three simulations, a)  $\lambda = 0.75$  ; b)  $\lambda = 0.875$  ; c)  $\lambda = 1.0$ , which illustrates the anisotropy in the  $(k_x, k_y)$  space. . . . . 77
- 4.25 Time-averaged wavenumber spectrum  $E(k_x) = \frac{1}{\Delta t} \int_t \eta(k_x, k_y, t) \int_{k_y} dk_y dt$  of interface structure over a period  $\Delta t = 15(s)$  for three simulations: a)  $\lambda = 0.75$  ; b)  $\lambda = 0.875$  ; c)  $\lambda = 1.0$ , in steady state situation. Dashed lines have slopes  $-19/4$ . . . . . 78

---

# 1

## Introduction

### 1.1 Motivation

Fluid transportation inside pipelines and channels requires the application of an external pumping power to win the friction losses at the walls. When the adopted fluid is oil, the resulting pumping power is extremely large due to the large oil viscosity. This has direct implications on the energy consumption which scales roughly with the third power of the of the transported flowrate. One possible strategy to limit this cost is represented by the injection of a low-viscosity fluid, which in most cases is water [44]. The effectiveness of this technique is due to the natural tendency of water to migrate towards the wall (high-shear region) so to lubricate the flow [38]. Since the pumping energy is spent to counterbalance the work done by the wall shear stress, viscous oil can be transported at the largely reduced cost of pumping water.

Due to its importance in the petroleum industry and in the process and chemical engineering, the present flow configuration has been extensively studied and analyzed in the past [21, 7, 21, 45, 58]. Literature in this field is vaste and old, dating back to the seminal industrial patents of [39] and [68]. An exhaustive literature review on the various aspects of the problem, together with an in-depth analysis of patents and solutions already existing is given by [78, 44]. It is important to note that most of the works in this field are based on experiments, and focus mainly on the quantification of global flow properties (flowrate and pressure drops) and on the qualitative characterization of the liquid-liquid interface structure. Obtaining a detailed time and space description of the entire flow field and of the liquid-liquid interface deformation is still an open issue for current experimental techniques. In this context, Direct Numerical Simulation (DNS) can be considered a useful tool to obtain the detailed evolution of the interface deformation together with an accurate description of the flow field in both

phases. Recently, DNS has proven accurate to analyze the complex time dependent three-dimensional dynamics of coupled gas-liquid turbulent flow [54, 67, 122], in particular to examine the physics of wave generation and the corresponding transfer rates of mass, momentum and energy across the interface. Compared to the case of gas-liquid flows, in which the number of DNS is constantly increasing, the case of liquid-liquid flows has attracted relatively less attention [65, 111].

Motivated by this lack of detailed investigations on the problem; we started a systematic investigation with the object of examining the role of the interface in this process.

In this thesis, we have run a series of DNS using a Phase Field Method to characterize the viscosity-stratified liquid-liquid flow inside a turbulent flat channel, and we also want to deepen the interaction between the deformable liquid-liquid interface and the wall turbulence. Our simulations are run starting from a fully-developed velocity field of a single-phase turbulent channel flow. The liquid-liquid interface is defined so to obtain the desired configuration consisting of a thin less viscous layer flowing on top of a thicker and more viscous layer. After the effect of the liquid-liquid interface on the global properties of the flow (mean velocity, volume flowrate), we focus more closely on the interaction between the interface dynamics and the near wall turbulence. In particular, we find that the modulation of turbulence induced by the liquid-liquid interface is so important that wall shear stress inversions and local recirculation regions can be observed. These findings have been properly quantified and have been linked to the topology of the flow and of the deformed interface.

### 1.1.1 Viscosity stratification and drag reduction

As discussed before, confined flows of cocurrent immiscible fluids are often observed in the process and petroleum industry. Important examples include oil-water separators and hydrocarbon transportation pipelines. In these situations, two-immiscible phases (typically oil and water) are driven inside pipelines/channels and interact modifying the overall mass, momentum and heat transfer properties of the system. To optimize the design of these systems it is crucial to determine whether the two phases remain separate (due to density and viscosity stratification) or form emulsions (which are difficult to process/separate). From a practical standpoint, the stratified condition (or even the core annular flow condition) is preferred for two main reasons: the required power to transfer the oil/water flow is lower (due to the lower viscosity of water wetting a wall compared to that of the oil) and oil can be easily separated from water (whereas more complex oil/water

separators must be designed when water is dispersed within the oil phase).

When a base state with separate phases (stratified flow) can be defined, a rigorous linear stability analysis of the governing equations [112, 101] can be done to determine if the base state is stable. Note that this linear analysis can only predict whether small disturbances will grow and their nature. Nonlinear theories are instead needed to determine if wave saturation of small-waveslope waves occurs [10, 90]. However, waves usually become large and form subharmonics that can interact so to produce triadic resonance. In all these cases, no theoretical prediction can be made, and experiments or accurate numerical simulations are required to capture the complex dynamics of liquid-liquid flows.

Technical challenges to obtain detailed information on the velocity/stress field in experiments of immiscible and stratified liquid-liquid flows have hindered the identification of the dominant mechanisms controlling the flow dynamics and have made difficult the development of robust physics-based wave generation models. Direct Numerical Simulation (DNS) is a useful tool for examining the detailed flow physics in such instances, in particular in the proximity of the deformed interface. For this reason, it can be used to provide important insights into the characterization of the interfacial dynamics.

In literature, there exists a number of studies focusing on the dynamics of interfacial waves in air-water two phase flows [67, 122]. However, much less is known about the dynamics of liquid-liquid interfaces [46, 45, 38, 21, 7].

## 1.2 Object of the thesis

In this thesis, we use Direct Numerical Simulations (DNS) to analyze the dynamics of a turbulent viscosity-stratified liquid-liquid flow moving inside a flat channel. A Phase Field approach (Cahn-Hilliard equation) is employed here to describe the liquid-liquid interaction in such configuration. The governing balance equations are solved through a pseudo-spectral method for a given value of the reference shear Reynolds number ( $Re_\tau = 100$ ) and for three different values of the viscosity ratio  $\lambda$  between the two liquid-layers ( $\lambda = 1$ ,  $\lambda = 0.875$  and  $\lambda = 0.75$ ).

Compared with the case of a single phase flow driven by the same pressure gradient, the viscosity stratified liquid-liquid flow is characterized by a larger volume flowrate, as a direct consequence of the conversion of mean kinetic energy into work to deform the liquid-liquid interface. These effects become stronger with increasing the viscosity difference between the

two liquid layers. Obtaining accurate estimates for the relative importance of the different terms of the Navier-Stokes equations is very important to understand the dynamics of turbulent transport in a liquid-liquid channel flow.

Note that one of the main objective of this thesis is to evaluate the influence of the liquid-liquid interface (characterized by a given surface tension) and of the viscosity ratio on the average properties of the flow (chiefly the mass flowrate and the skin friction). To achieve this goal, we have also shown the influence of the interface surface tension  $\sigma$  on the average strain, vorticity and velocity fluctuations. We also focus more closely on the interaction between the interface dynamics and the near wall turbulence. In particular, we find that the modulation of turbulence induced by the liquid-liquid interface is so important that wall shear stress inversions and local recirculation regions can be observed. These findings have been properly quantified and have been linked to the topology of the flow and of the deformed interface. Finally, we study capillary wave turbulence of the liquid-liquid interface from both theoretical and computational considerations.

### 1.2.1 Thesis layout

This thesis is organized as follows:

- **Chap. 2** : The available theories developed to model the presence of a liquid-liquid interface will be discussed. Yet, the theoretical background behind the Phase Field Method (PFM) will be discussed and the final governing equations of the multiphase flow system (i.e Cahn-Hilliard and Navier-Stokes, CH-NS) will be derived. The dimensionless counter part of the governing balance equations will be then presented.
- **Chap. 3** : The numerical technique employed in this study, based on a Pseudo-spectral method to perform a DNS of the CH-NS equations in a closed channel, will be presented.
- **Chap. 4** : The numerical method discussed above is first benchmarked against literature data (Sect. 4.2). In Sect. 4.2 and Sect. 4.3, the results obtained from the direct numerical simulation of viscosity stratified turbulent channel flow are presented and discussed.

In Sect. 4.4, we compute and discuss the behaviour of the interfacial liquid-liquid waves in the framework of Weak Turbulence Theory (WTT).



---

# 2

## Methodology

This chapter is relevant to the fundamentals of Phase Field Method (PFM) is used in our DNS in order to simulate liquid-liquid flow. The available theories developed to model the presence of a liquid-liquid interface will be discussed. Yet, the theoretical background behind the Phase Filed Method (PFM) will be discussed and the final governing equations of the multiphase flow system (i.e Cahn-Hilliard and Navier-Stokes, CH-NS) will be derived. The dimensionless counter part of the governing balance equations will be then presented.

### 2.1 Interface Representation

Numerical methods used for the simulation of multiphase flows, can be classified based on the type of flow modelling (Eulerian, Lagrangian, Mixed), the type of interface modelling (Capturing or Tracking), and the type of spatial discretization (finite difference, finite volume, finite element and others). The most common approach to compute multiphase flows is to capture/track the interface directly on a regular, stationary grid (Eulerian Method). The three methods share common modified Navier–Stokes equations. In moving boundary problems one typically distinguishes between two approaches: interface tracking and interface capturing.

- **Interface tracking** : In interface tracking method, interface is explicitly described by the computational mesh. As consequence, the movement of the interface has to be accounted by adjusting the position of the nodes on the interface. While the movement of the interface nodes is prescribed, e.g. by an underlying velocity field, the adjustment of the inner mesh nodes is arbitrary, while Interface tracking approaches are

known to provide great accuracy, yet their applicability is limited in the case of severe interface motion.

- **Interface capturing methods** : An artificial scalar field is using for an implicit description of the interface capturing methods. The most common representatives of this class of approaches are the level set and the volume of fluid method. These approaches are inherently able to consider problems, where the interface is subjected to topological changes can be considered. Nonetheless, this flexible interface description provides challenges regarding mass conservation and the treatment of discontinuities across the interface.

It is important to choose an accurate method for interface movement numerically, in the following, we briefly describe the Level Set Method (LSM), Immersed Boundary Method (IBM) and Phase-Field Method (PFM) for representing the interface of two immiscible fluids and briefly discusses the advantages and disadvantages of each method.

- **LSM** : It was devised by [81] and it will be used as a simple and versatile method for computing the motion of an interface, which is captured as the zero-level set of a smooth scalar function [82, 84, 102]. At each time step, a reinitialization step is needed to recover to the signed distance function without changing its zero level set. In this method, jump in phase properties across the interface may lead to numerical difficulties. One of the main drawbacks of (LSM) is its lack of mass conservation. This leads to non physical motions of the interface, which severely deteriorate the accuracy and stability of the simulation results [102].
- **IBM** : It is important to stress that the IBM has been introduced far before the (LSM) has been known. Both are completely independent concepts, but they can be combined, this method uses the indicator function, that is nonzero near the interface and zero in the other domain, a methodology for dealing with a body, which does not necessarily have to fit conform a Cartesian grid, but conservation properties of numerical schemes are not trivial. Alignment between grid lines and body surface in boundary- conforming grids allows for better control of the grid resolution in the vicinity of the body and this has implications for the increase of grid size with higher Reynolds numbers.
- **PFM** : Phase-Field Method is an alternative option to capture the evolution of a fluid/fluid interface, which belongs to the class of Eulerian methods, in this method, for numerical accuracy interface thickness must be at least a few grid lengths in size, this method has rapidly

gained popularity over the last two decades in various fields. In the following we will explain this model in detail:

## 2.2 Diffuse and sharp-interface methods

Two main theories exist as far as the nature of the interface of two separated fluid are:

1. Sharp-Interface Model
2. Diffuse-Interface Model

1) It is known that: in sharp interface model fluid equations are posed on each side of the interface and jump conditions are prescribed across the interface. This model, however fails when the fluids interface undergoes singular topological transitions such as pinch off or reconnection, most of researchers have found sharp interface methods have some limitation in simulation of between immiscible fluids, the evolution of sharp interface can be taken by two common methods: front tracking or front capturing. In front tracking it is possible to trace interface position. In front capturing method scalar field will be added and the transition between two fluid can be marked.

Sharp interface models break down whenever the interface thickness is comparable to the length scale and the surface tension is typically assumed to be constant along the surface [61].

2) Diffuse-interface methods considers the interface between the two fluids to have a non-zero thickness endowed with physical properties such as surface tension. In this method interface can be modeled as a three dimensional region and properties of the material vary continuously from their value in one bulk phase to their value in the other bulk phase [61]. In diffuse-interface methods interface between the two fluids to has a non-zero thickness dedicated with physical properties such as surface tension. For a review of the development of diffuse-interface models, it applied to different interfacial phenomena [4]. Phase-field models are particular type of diffuse-interface models that are based on fluid free energy, an idea that can be traced to [106]. More reviews of phase-field models and simulations for microstructure evolution, can be find in [22, 11, 61]. The main drawback of phase-field models is the thickness of the interface. Although in reality there is an existing region, where a property of one fluid changes to the other, the current capability of computers only allows us to have a thickness way much more than the thickness of this region.

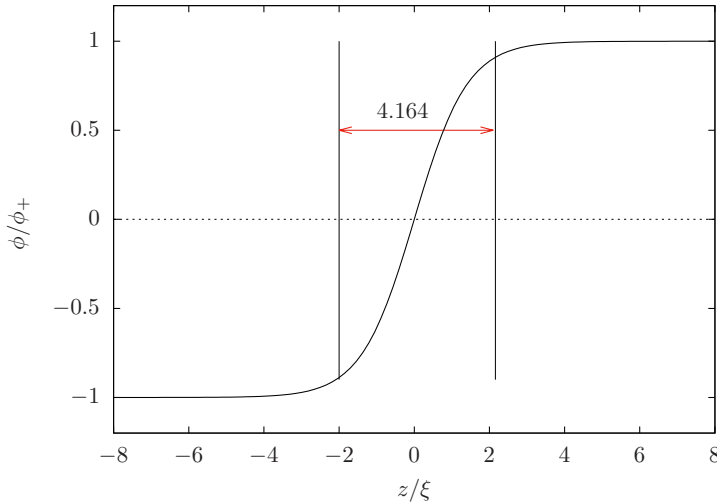


FIGURE 2.1 – Concentration profile across the diffused interface region with the thickness  $\xi$ , (interface located between:  $-0.9 < \frac{\phi}{\phi_+} < 0.9$ ).

### 2.2.1 Phase Field Method

A phase-field model is well suited for studies of morphological evolutions that are described by nonlinear partial differential equations. In the phase-field model, sharp fluid interfaces are replaced by thin but nonzero thickness transition regions, where the interfacial forces are smoothly distributed. The basic idea is to introduce a conserved order parameter (e.g., mass concentration) that varies continuously over thin interfacial layers and is mostly uniform in the bulk phases (see Fig. 2.1).

The fundamental idea of this method is to use an order parameter  $\phi$ , which determines the phases in a multiphase system. This parameter is constant in each bulk phase, e.g.  $\phi = +1$  in one phase and  $\phi = -1$  in the other phase. The interface between phases is represented by a smooth transition region.

In this computation we have two Newtonian fluids in contact with each other. We assume that the binary solution is incompressible, immiscible and isotropic at constant temperature (isothermal) and of constant volume. The interface that separates the two fluid liquids, is supposed not to be a geometric surface but a thin layer that has properties differing from those of the bulk material on either side of the interface. Van der Waals [106] developed in detail the diffuse interface theory and, in particular, and used

his equation of state to predict the interface thickness of a mixture, showing that it tends to infinite when the mixture approaches critical conditions.

### 2.2.2 Ginzburg-Landau free energy functional

The Ginzburg-Landau free energy functional  $\mathcal{F}$  is assumed to be a function of  $\phi$  and its gradient  $\nabla\phi$ . The phase field function  $\phi(x, y, z, t)$  is constant in the bulk of two phases and a smooth transient occurs through the interface. The free energy functional  $\mathcal{F}$  can be expressed as follows:

$$\mathcal{F}(\phi, \nabla\phi) = \int_{\Omega} f_0 + \frac{\epsilon}{2} |\nabla\phi|^2 d\Omega. \quad (2.1)$$

The free energy  $\mathcal{F}(\phi, \nabla\phi)$  is conservative, thermodynamically consistent. The first term on the right-hand side of Eq. (2.1) is the ideal part of free energy and accounts for the tendency of the system to separate into pure fluids clusters. For two immiscible fluids, the phobic behaviour is described by a double-well formulation which shows two minima corresponding to the two stable fluid phases:

$$f_0 = \frac{\alpha}{4} (\phi - \sqrt{\frac{\beta}{\alpha}})^2 (\phi + \sqrt{\frac{\beta}{\alpha}})^2 \quad (2.2)$$

where  $\alpha$  and  $\beta$  are two positive constants defining the properties of the interface. Since the two fluids are allowed to mix into the interfacial layer, they store a mixing energy which is kept in account by the non-local term  $\frac{\epsilon}{2} |\nabla\phi|^2$  of Eq. (2.1). The mixing energy stored into the interfacial layer is controlled by the positive parameter  $\epsilon$ .

Due to choosing type of dissipation the dynamic of  $\phi$ , can be given by Allen-Cahn or Chan-Hilliard types of gradient flow.

Cahn-Allen equations describe the evolution of a non-conserved quantity and commonly used in solidification and nucleation problems. The Cahn-Hilliard theory, on the other hand, describe the evolution of a conserved order parameter and is used in spinodal decomposition problems. In what follows is a derivation of the Cahn-Hilliard equation based on the works of [17, 106, 40].

Keeping in mind that it is possible for phases to differ in other physical quantities such as viscosity or density, if we consider a regular solution model for free energy, as shown in Fig. 2.2, that is in homogeneous situation in region of its phase diagram  $(P, T, \phi)$ , in such a system can lower its free energy by separating into two phases with an interface. For any

composition inside the miscibility gap (between  $\phi = -1$  and  $\phi = 1$ ), a phase separated system is favourable energetically. By going outside the miscibility gap, the system remains homogeneous at equilibrium no matter what the composition. Gibbs distinguished between two types of classic treatment transformations in: those that are small in degree and large in extent: spinodal decomposition and those that are large in degree and small in extent like as nucleation, which explained in following :

- **Spinodal decomposition** : is a mechanism by which a solution of two or more components can separate into distinct phases with distinctly different chemical compositions and physical properties. Compositions between a region of linear instability where  $f_0''(\phi) < 0$  and small fluctuations will grow spontaneously through a process called spinodal decomposition, where the phase separation due is much more defined, and occurs uniformly throughout the material, about this problem, Cahn & Hillard added the forth order of gradient including K to the free energy.
- **Classical nucleation** : is a nonlinear instability situation, for surface area of a sphere drop a nucleus larger than the critical radius will grow and requires the formation of a large enough nucleus of the nucleating phase, one of disadvantage of the classical nucleation model is they are not in agreement with experiment because of dealing with interface as a sharp discontinuity. Here, treating interfacial energy as a constant and modelling the interface as a sharp discontinuity are too simplistic.

The classical expression for the specific Helmholtz free energy can be changed from Eq. (2.1) used in diffuse interface modelling, which was first introduced by [16] to model the evolution of a conserved concentration field during the spontaneous phase separation of a binary fluid.

$$\mathcal{F}(\phi, \nabla\phi) = \int_{\Omega} \left( -\frac{1}{2}\alpha\phi^2 + -\frac{1}{4}\beta\phi^4 \right) + \frac{1}{2}\epsilon |\nabla\phi|^2 d\Omega \quad (2.3)$$

where  $\alpha$  and  $\beta$  are two positive constants that define the interface properties and  $\epsilon$  is the gradient -energy parameter.

The Cahn-Hilliard equation is a non-linear, stiff, fourth order (in terms of  $\phi$ ) equation that satisfies an energy law is :

$$\frac{D\phi}{Dt} = -\nabla \cdot \mathbf{J} \quad (2.4)$$

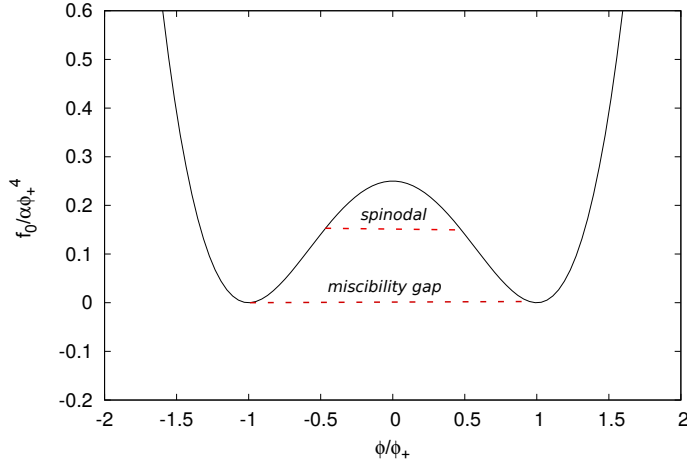


FIGURE 2.2 – Regular solution model for free energy

Here,  $\mathbf{J} = -\mathcal{M}\nabla\mu$  is a phase field flux (i.e. a generalized mass flux) responsible to run the system toward its equilibrium conditions following a chemical potential  $\mu$ . If we substitute the phase flux into Eq. (2.4) and expand it to the total derivative, the convective Cahn-Hilliard equation arrives:

$$\frac{\partial\phi}{\partial t} = -\mathbf{u} \cdot \nabla\phi + \nabla(\mathcal{M}\nabla\mu), \quad (2.5)$$

where  $\mathbf{u}$  is the velocity field,  $\mathcal{M} = \mathcal{M}(\phi)$  is the mobility or Onsager coefficient that controls the interface relaxation time, it changes appropriately as the interface thickness keeps on reducing, regarding to maintain the effective interface force consistent with the required surface tension [71] and  $\mu$  parameter is: chemical potential (for instance some researches [16, 14, 113], also known as partial molar free energy, that controls the interfacial layer behaviour, in purpose of simplicity, the proportionality factor between current and chemical potential gradient, the mobility  $\mathcal{M}$ , should be constant. Eq. (2.5) models the evolution in time of a diffuse interface specially it can represent the advection of the scalar field, where the interface does not degrade by numerical diffusion [40], [19]. Those phenomena are driven by the minimization of the chemical potential  $\mu$  that defined as the variational derivative of the free energy functional  $f[\phi]$  in following:

$$\mu = \frac{\delta\mathcal{F}[\phi(z), \nabla\phi]}{\delta\phi} \quad (2.6)$$

$$f_0 = \frac{\alpha}{4}(\phi - \sqrt{\frac{\beta}{\alpha}})^2(\phi + \sqrt{\frac{\beta}{\alpha}})^2 \quad (2.7)$$

The two fluids are allowed to mix into the interfacial layer, and they store a mixing energy that is kept in account by the non-local term  $\epsilon \nabla \phi^2$ , the positive parameter  $k$  and it is the origin of the surface tension in to the PFM. Introducing the double-well potential Eq. (2.7) into Eq. (2.1), the dimensionless chemical potential difference  $\mu(\phi) = \mu_1 - \mu_2$  for an immiscible binary mixture is obtained:

$$\mu(\phi) = \alpha\phi^3 - \beta\phi - \epsilon \nabla^2 \phi \quad (2.8)$$

The final state is obtained by minimizing the free-energy functional with respect to variations of the function Eq. (2.1) with respect to the variations of the order parameter, namely setting the chemical potential to zero: The integration of above equation for a mono-dimensional planar interface, where  $\phi(z < \pm\infty) = \phi_{\pm}$ , yields two stable solutions  $\phi_{\pm} = \pm\sqrt{\frac{\beta}{\alpha}}$  and  $2\phi_{\pm}$  is the miscibility gap as mentioned in Fig. 2.2 and allows for the description of the interface between the two fluids by a continuously varying concentration profile, in a planar interface, with defining  $z$  being the direction normal to the interface, one easily finds the solution Eq. (2.8) as:

$$\phi(z) = \phi_+ \tanh\left(\frac{z}{\sqrt{2}\xi}\right) \quad (2.9)$$

The capillary width  $\xi = \sqrt{\frac{\epsilon}{\beta}}$  is a measure of the thickness of diffuse interface, in particular 90% of variation in  $\phi$  corresponds to a thickness of  $4.164\xi$  (as shown in Fig. 2.1), contains 98.5% of interface tension [6, 113]. Eq.( 2.9) gives the minimum value for free energy, which has also local minimum regarding to periodic profiles [72]. Regarding to Eq. (2.9), which is valid and stable in all dimensions although the decay rate of perturbations depends on the dimensionality [56], one easily finds that the sharp-interface will be obtained when  $\tanh\frac{z}{\sqrt{2}} \rightarrow \text{sign}(z)$ .

Surface tension  $\sigma$  can be obtained by integral of the free-energy density along the interface:

$$\sigma = \frac{\sqrt{8}}{3} \frac{\epsilon^{\frac{1}{2}} \beta^{\frac{3}{2}}}{\alpha} \quad (2.10)$$

### 2.2.3 Mass conservation

With proper boundary conditions ( $\mathbf{v} \cdot \mathbf{n} |_{\partial\Omega} = 0$ ,  $\mathbf{n} \cdot \nabla\mu |_{\partial\Omega} = 0$ ), where  $\partial\Omega$  is the boundary of domain and  $\mathbf{n}$  is the normal to  $\partial\Omega$  by taking integration of Eq. (2.5) over  $\Omega$ :

$$\frac{d}{dt} \int_{\Omega} \phi d\Omega = 0 \quad (2.11)$$

If we multiply Eq. (2.5) with  $\mu$  and integrate it whole domain  $\Omega$ , we obtain:

$$\frac{d\mathcal{F}}{dt} = -\mathcal{M} \int_{\Omega} (\nabla\mu)^2 d\Omega \leq 0, \quad (2.12)$$

Which confirms Cahn-Hilliard system always tends to minimize  $\mathcal{F}$ . The implications of Cahn-Hilliard diffusion on mass conservation using a phase-field model for simulating two-phase flows in above has been discussed by [114] and they found even though the phase-field variable  $\phi$  is conserved globally drop shrinks spontaneously while  $\phi$  shifts from its expected values in the bulk phases proportional to the interfacial thickness, and they suggested guidelines for minimizing the loss of mass. With a properly chosen mobility parameter, however this process will be much slower than the physics of interest and thus has little ill effect on the simulation.

## 2.3 The incompressible Navier-Stokes equations

In the PFM, the velocity field evolution for a multiphase system is given by a single set of continuity and momentum equations written for the whole system, in which the thermophysical properties are dependent on the order parameter  $\phi$ . Here, Navier-Stokes equations are isothermal and viscous. The system consists of partial differential equations expressing conservation of momentum and mass, respectively, and reads:

$$\rho \left( \frac{\partial \mathbf{u}}{\partial t} + \mathbf{u} \cdot \nabla \mathbf{u} \right) = \rho \nabla \cdot (\nu(\phi)) (\nabla \mathbf{u} + \nabla \mathbf{u}^T) - \nabla p + \nabla \cdot \tau_c \quad (2.13)$$

Here,  $\mathbf{u}$  is the velocity vector,  $p$  the pressure term,  $\rho$  is the fluid density and  $\nu$  is the fluid kinematic viscosity,  $\tau_c$  is stress tensor that is associated with surface tension and is:

$$\tau_c = (|\nabla\phi|^2 \mathbf{I} - \nabla\phi \otimes \nabla\phi) \quad (2.14)$$

Such a stress tensor, called capillary tensor, was defined by Korteweg [55], where uniform distribution of  $\phi$  can induce stresses and convection in fluid [57] and this stress tensor has been added to Navier-Stokes equations. In two immiscible fluids it acts as an effective interfacial tension that relaxes in time by effect of mass diffusion. We assume coupled Cahn-Hilliard-Navier-Stokes system to be isothermic and thermal effects are not included in the solution, which in reality this assumption needs very careful condition. Compared with the Navier-Stokes equations, in Eq. (2.13) only one extra capillary term appears reflecting the interfacial tension. This modification accounts for hydrodynamic interactions, that is, the influence of the  $\phi$ , or the morphology on the velocity field and, hence, describes the spatial variations of the velocity field because of diffused interfaces.

The dimensional form of the continuity equation will be:

$$\nabla \cdot \mathbf{u} = 0 \quad (2.15)$$

Thanks to the conservative nature of the PFM, which avoids interface to diffuse; as a result  $\nabla\phi$  keeps the property of a signed distance and the momentum transfer to the flow field is resolved with high accuracy. The surface tension is defined as the specific energy stored into the interfacial layer; applying the definition to Eq. (2.8), as we also mentioned in Eq. (2.10), since  $\phi$  isn't homogeneous in interface region the surface tension is the excess free energy [20] and it will be:

$$\sigma = \epsilon \int_{-\infty}^{+\infty} (\nabla\phi \cdot \mathbf{n})^2 d\mathbf{n} = \frac{\sqrt{8}}{3} \frac{\epsilon^{\frac{1}{2}} \beta^{\frac{3}{2}}}{\alpha} \quad (2.16)$$

Once the interface thickness  $\xi$  and the equilibrium solutions  $\phi_{\pm}$  are fixed, Eq. (2.16) will allow to determine the free energy parameters  $\alpha$ ,  $\beta$  and proper  $\epsilon$  to reach the desired surface tension value. Although the fictitious enlargement of the interface is necessary related to numerical resolution (at least three mesh points will be considered for interface [95]), we should care about if the diffuse interface is relaxed but not at a equilibrium, interfacial tension would not be constant [113]. The related method for PFM mentioned above has been devised and used by several authors [62, 4].

## 2.4 Geometry

In the most general case, the governing equations of the different constituents have to be coupled together, by using momentum balance equations (Navier-Stokes equations) the physical model equations can be extremely

complex and their solution can require numerical algorithms and computational resources beyond those currently available. By considering PFM; from the numerical point of view the diffuse approximation of the interfaces can overcome some unwelcome features of other approaches: i) larger accuracy is granted in the interface description: the thermodynamically conservative nature of the model avoids the interface detriment and the need of correction techniques; ii) the constitutive law for the capillary stress yields to an accurate description of the interfacial forces; iii) proper scaling of the equation parameters allow to extend the model also to the description of immiscible fluid systems. We consider a turbulent oil-water flow, as sketched in Fig. 2.3. The flow configuration consists of two liquid layers (Oil and water) separated by a deformable interface. The oil and water, which are considered to be incompressible and Newtonian, and flow in same directions. We consider an oil layer with thickness  $h_2 = 1.8h$  flows under a thin liquid layer of water with thickness  $h_1 = 0.2h$ . The origin of the coordinate system is located at the centre of each domain, and the  $x$ ,  $y$  and  $z$  axes point in the streamwise, spanwise and wall-normal directions.

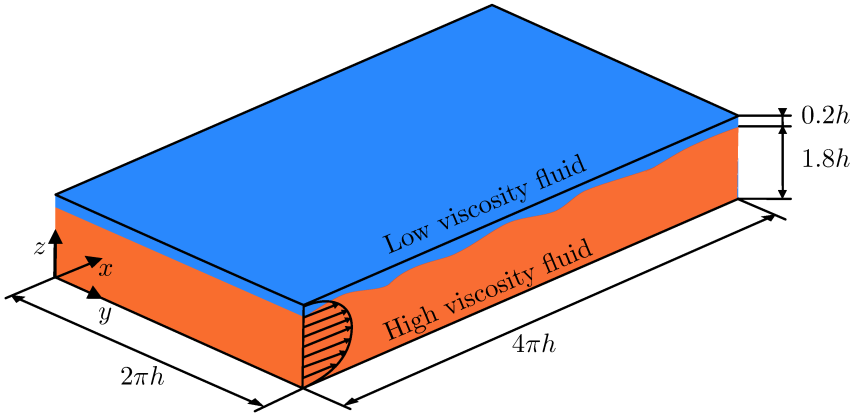


FIGURE 2.3 – Sketch of the computational domain. A thin liquid layer with viscosity  $\nu_1$  flows on top of a thicker liquid layer with viscosity  $\nu_2$ .

### 2.4.1 Dimensional analysis

It is convenient for physical discussions and mathematical transparency to consider a dimensionless form of the equations. In this work, the governing equations Eqs. (2.5), (2.8), (2.13) and (2.15) have been solved on a flat channel geometry, where two infinite parallel walls are deployed at a distance  $L_z = 2h$ . With reference to Fig. 2.3, the governing equations can be

rewritten in a non dimensional form by using the following non dimensional variables (denoted by apex “-”):

$$\mathbf{x}^- = \frac{\mathbf{x}}{h} \quad \mathbf{u}^- = \frac{\mathbf{u}}{U_\tau} \quad t^- = \frac{tU_\tau}{h} \quad \phi^- = \frac{\phi}{\phi_+} \quad p^- = \frac{p}{\rho U_\tau^2} \quad (2.17)$$

$$\nabla \cdot \mathbf{u}^- = 0 \quad (2.18)$$

$$\frac{\partial \mathbf{u}^-}{\partial t^-} + \mathbf{u}^- \cdot \nabla \mathbf{u}^- = -\nabla p^- + \frac{1}{Re_\tau} \nabla^2 \mathbf{u}^- + \nabla \cdot [k(\phi, \lambda)(\nabla \mathbf{u}^- + \nabla \mathbf{u}^{-\mathbf{T}})] + \frac{3}{\sqrt{8}} \frac{Ch}{We} \nabla \cdot \boldsymbol{\tau}_c^- \quad (2.19)$$

$$\frac{\partial \phi^-}{\partial t^-} = -\mathbf{u}^- \cdot \nabla \phi^- + \frac{1}{Pe_\tau} \nabla^2 \mu^- \quad (2.20)$$

$$\mathcal{F}(\phi^-, \nabla \phi^-) = f(\phi^-) + \frac{1}{2} Ch^2 |\nabla \phi^-|^2 = \frac{1}{4} (\phi^- - 1)^2 (\phi^- + 1)^2 + \frac{1}{2} Ch^2 |\nabla \phi^-|^2 \quad (2.21)$$

$$\mu^- = \frac{\delta \mathcal{F}}{\delta \phi^-} = \phi^{-3} - \phi^- - Ch^2 \nabla^2 \phi^- \quad (2.22)$$

Eqs. (2.18-2.19) describe the conservation of mass (continuity) and momentum, with an extra reactive stress (Navier-Stokes) of the system, with  $\mathbf{u} = (u_x, u_y, u_z)$  being the velocity field and  $\tilde{p}$  the corrected pressure field [93]. Eq. (2.20) is the Cahn-Hilliard equation that describes the transport of the order parameter  $\phi$  used to model the binary mixture:  $\phi$  is constant in the bulk fluid regions (where  $\phi = \pm 1$ ) and changes smoothly across the fluid-fluid interface. The free energy functional  $\mathcal{F}(\phi, \nabla \phi)$  of the system Eq. (2.21), is the sum of two different contribution: a double-well potential  $f_0(\phi)$  that accounts for the phobic behavior of the phases and a non-local term that accounts for the effect of surface tension ( $\propto |\nabla \phi|^2$ ). The variation of the free energy functional is called chemical potential  $\mu$  and controls the behavior of the interfacial layer Eq. (2.22). Note that Eqs. (2.19 - 2.20) are coupled through the capillary term  $\frac{3}{\sqrt{8}} \frac{Ch}{We} \nabla \cdot \boldsymbol{\tau}_c$  that describes the momentum exchange between the two phases across the interface.

The term  $k(\phi, \lambda)$  in Eq. (2.19) is introduced to account for the non-uniform viscosity of the system. Viscosity can be written as a linear function of the order parameter  $\phi$  [49, 118]

$$\nu(\phi) = \nu_1 \frac{1 + \phi}{2} + \nu_2 \frac{1 - \phi}{2}. \quad (2.23)$$

The material properties of the two media vary following the same continuous and rapid variation of  $\phi$  across the thin interfacial region. The density and viscosity in the phase-field are linear functions [48, 6]. As a result, using linear interpolation, the viscosity of the two liquids are distributed in the interfacial layer as Introducing the viscosity ratio  $\lambda$ , the viscosity field can be written as the sum of a uniform and a non-uniform part and automatically changes across the interface with a profile similar to the *tanh* function [119, 120]:

$$\nu(\phi, \lambda) = \nu_2 + \nu_2(\lambda - 1) \frac{(\phi + 1)}{2}. \quad (2.24)$$

In dimensionless units, the non uniform part of the viscosity field becomes:

$$k(\phi, \lambda) = \frac{1}{Re_\tau} (\lambda - 1) \frac{(\phi + 1)}{2}. \quad (2.25)$$

The following dimensionless groups appear in Eqs. (2.18)-(2.22):

$$Re_\tau = \frac{u_\tau h}{\nu_2} \quad Pe_\tau = \frac{u_\tau h}{\mathcal{M}\beta} \quad We = \frac{\rho u_\tau^2 h}{\sigma} \quad Ch = \frac{\xi}{h} \quad \lambda = \frac{\nu_1}{\nu_2}, \quad (2.26)$$

Where  $\sigma$  is the surface tension of the liquid-liquid interface,  $\mathcal{M}$  is the mobility, and  $\xi$  the thickness of the liquid-liquid interface within the PFM method. The reference length of the problem is the half channel height  $h$ , whereas the reference velocity is the shear velocity  $u_\tau = \sqrt{\tau_w/\rho}$ , with  $\tau_w$  the shear stress at the wall defined in terms of the viscosity of the thicker liquid layer  $\nu_2$ . The physical meaning of the dimensionless groups is the following. The Reynolds number ( $Re_\tau$ ) is the ratio between the inertial and the viscous forces (defined based on the viscosity  $\nu_1$ ). The Weber number ( $We$ ) is the ratio between the inertial and the surface tension forces. Small values of  $We$  represent a rigid interface, whereas large values of  $We$  represent an highly deformable interface. The Peclet number ( $Pe_\tau$ ) is the ratio between the convective and the diffusive time-scale, and it quantifies the relaxation time of the interface. The larger is  $Pe_\tau$ , the larger is the time required by the interface to adapt to the external forcing. Finally, the Cahn number ( $Ch$ ) is the dimensionless thickness of the interface.

### 2.4.2 Wall units

All of are reported results will be presented in “wall-units” (Variables with a + superscript are expressed), that are defined by using the friction velocity  $u_\tau$  and the kinematic viscosity  $\nu$  of the fluid. The dimensionless variables

are the following:

$$\mathbf{x}^+ = \frac{\mathbf{x}U_\tau}{\nu} \quad \mathbf{u}^+ = \frac{\mathbf{u}}{U_\tau} \quad t^+ = \frac{tU_\tau^2}{\nu} \quad (2.27)$$

Because phase-field do not depend on the fluid scaling variables, it doesn't change when described in wall-units:  $\phi^+ = \phi^-$

---

# 3

## Numerical method

Coupling NS equation with CH has been successfully applied for the simulations of two-phase flow in various researches with several challenges in solving these equations numerically. With considering thickness for interface which cause huge amount of stiffness into the system, which only unconditionally stable numerical scheme can handle it. In this Chapter, the numerical technique employed in this study, based on a Pseudo-spectral method to perform a DNS of the CH-NS equations in a closed channel, will be presented.

### 3.1 Introduction to pseudo spectral method

Numerical flow field simulations based on spectral methods for the solution of the Navier–Stokes (NS) equations has been used in last decades. All related numerical solution procedures are using finite difference or finite element techniques, when spectral methods are employed for Direct numerical Simulation (DNS), they have properties of exponential convergence behaviour and reducing dispersion which are suited for turbulent flow. They have proven to be useful for hydrodynamical problems on periodic domains. Their main advantages are efficiency and accuracy of implementation.

In spectral methods, spatial derivatives are evaluated with the aid of Fourier series or one of their generalizations. What we know about spectral method is:

- The method is easily generalized to higher derivatives
- The error in the computed derivative decreases exponentially with  $N$ , when the number of grid points  $N$  is large if  $f(x)$  is periodic in  $x$ , for

larger  $N$  leads to much more accurate than finite difference methods.

- Since cost of computing scales as  $N^2$  the method uses the existence of a fast method of computing Fourier transform (*FFT*), which the cost is proportional to  $N \log N$ , where  $N$  is the data size.

### 3.1.1 Chebyshev pseudospectral Method

Navier-Stokes equations in the velocity-vorticity  $(\mathbf{u}, \boldsymbol{\omega})$  has been used in many literatures. For instance [31] was the first researcher, who used numerical simulations of the unsteady Navier-Stokes equations with the velocity-vorticity method and finite difference by using Fourier Chebyshev. Chebyshev pseudo-spectral method accounts on high accuracy for fluid dynamics, which keeps the convergence of infinite order. Time-splitting pseudospectral technique developed by [59] to solve the Navier-Stokes equations with a new Chebyshev pseudospectral technique for two-dimensional incompressible flow is extended to three dimensions, the most different between spectral and pseudospectral methods is aliasing errors, but it will not be problematic regarding to damping effects which limits aliasing [33], which with filtering techniques these errors can be eliminated [92]. Since using spectral method had some difficulty about time advancing for viscous flows, pseudo spectral method has been suggested by [73] where, in this method flow variables are expanded into Fourier series in the homogeneous directions and Chebyshev polynomials in the wall normal direction with no-slip condition. What is interesting about Chebyshev polynomial approximation is that errors decreases when it combines with Fast Fourier Transform (FFT) [80].

## 3.2 Numerical Procedure

In this algorithm which is based on [51] the governing Eqs. (2.20) and (2.19) for an incompressible flow can be written in the form of “normal-velocity normal-vorticity”; the Cahn-Hilliard equation is rewritten adopting a particular “operator-splitting” technique.

### 3.2.1 Velocity-vorticity formula

The dimensionless momentum Eq. (2.19) is rewritten as follows (the superscripts have been removed for sake of brevity):

$$\frac{\partial \mathbf{u}}{\partial t} = -\mathbf{S} + \frac{1}{Re_\tau} \nabla^2 \mathbf{u} - \nabla p' \quad (3.1)$$

Where the pressure term  $p$  has two parts including fluctuating and mean components,  $p = p' + \Pi$ . The mean pressure gradient, the non-linear convective terms and the source terms all have been collected in to the  $\mathbf{S}$  term:

$$\mathbf{S} = -\mathbf{u} \cdot \nabla \mathbf{u} - \nabla \Pi + \frac{3}{\sqrt{8}} \frac{Ch}{We} \nabla \cdot \boldsymbol{\tau}_c. \quad (3.2)$$

the fluctuating pressure term  $\nabla p'$  is eliminated by taking the curl of Eq. (3.1), as result the transport equation for the vorticity  $\boldsymbol{\omega}$  arrives:

$$\frac{\partial \boldsymbol{\omega}}{\partial t} = \nabla \times \mathbf{S} + \frac{1}{Re_\tau} \nabla^2 \boldsymbol{\omega} \quad (3.3)$$

Where the identity  $\nabla \times \nabla p' = 0$  has been substituted. Taking twice the curl of Eq. (3.1), substituting the continuity Eq. (2.18) and employing to:  $\Delta \times \nabla \times \mathbf{C} = \nabla(\nabla \cdot \mathbf{C}) - \nabla^2 \mathbf{C}$  the following 4<sup>th</sup>-order equation for the velocity  $\mathbf{u}$  is obtained:

$$\frac{\partial \nabla^2 \mathbf{u}}{\partial t} = \nabla^2 \mathbf{S} - \nabla(\nabla \cdot \mathbf{S}) + \frac{1}{Re_\tau} \nabla^4 \mathbf{u} \quad (3.4)$$

Eqs. (3.3-3.4) are solved for the wall-normal components of the vorticity  $\omega_z$  and velocity  $w$ ; coming back to Eqs. (3.3-3.4) for  $\omega_z$  and  $w$ , respectively, we have:

$$\frac{\partial \omega_z}{\partial t} = \frac{\partial S_y}{\partial x} - \frac{\partial S_x}{\partial y} + \frac{1}{Re_\tau} \nabla^2 \omega_z \quad (3.5)$$

$$\frac{\partial(\nabla^2 w)}{\partial t} = \nabla^2 S_z - \frac{\partial}{\partial z} \left( \frac{S_x}{\partial x} + \frac{S_y}{\partial y} + \frac{S_z}{\partial z} \right) + \frac{1}{Re_\tau} \nabla^4 w \quad (3.6)$$

With choosing right set of boundary conditions,  $\omega_z$  and  $w$  will be obtained and then the stream-wise velocity component  $u$  and the span-wise velocity component  $v$  will compute from the continuity equation and employing vorticity:

$$\frac{\partial \omega}{\partial z} = -\frac{\partial u}{\partial x} - \frac{\partial v}{\partial y}, \quad (3.7)$$

$$\omega_z = \frac{\partial v}{\partial x} - \frac{\partial u}{\partial y}. \quad (3.8)$$

Once the normal velocity and vorticity are computed, the streamwise velocity  $u$ , and the spanwise velocity  $v$ , are then obtained, the fluctuating pressure  $p'$  can be obtained by solving a poisson-type equation where is derived from the momentum equation, because it is derived by taking the

divergence of the momentum equation.

$$\nabla^2 p' = \nabla \cdot \mathbf{S}. \quad (3.9)$$

### 3.3 Cahn-Hilliard equation discretization

Cahn-Hilliard (CH) equations are slightly more complicated, due to the high order operators that accounts in numerical simulation, by expanding Eq. (2.20) we will see 4<sup>th</sup> order operator:

$$\frac{\partial \phi}{\partial t} = -\mathbf{u} \cdot \nabla \phi + \frac{1}{Pe} (\nabla^2 \phi^3 - \nabla^2 \phi - Ch^2 \nabla^4 \phi) \quad (3.10)$$

Regarding to stability of CH Eq. (3.10) can be rewritten in the following way as the same pseudo-spectral solution involved for the momentum equations :

$$\frac{\partial \phi}{\partial t} = S_\phi + \frac{s}{Pe} \nabla^2 \phi - \frac{Ch^2}{Pe} \nabla^4 \phi, \quad (3.11)$$

The operator splitting  $\nabla^2 \phi = s \nabla^2 \phi - (s-1) \nabla^2 \phi$  is similar to that discussed by [113], hence  $s$  is a positive coefficients, which has been explained in Sect. 3.3.1. The convective and the non-linear terms and the terms rising from the operator splitting will be collected in the  $S_\phi$  term:

$$S_\phi = -\mathbf{u} \cdot \nabla \phi + \frac{1}{Pe} \nabla^2 \phi^3 - \frac{s+1}{Pe} (\nabla^2 \phi). \quad (3.12)$$

#### 3.3.1 Stability of Cahn Hilliard equation

Regarding to widely used of CH equation in interface, it is essential to use a accurate numerical schemes when they should satisfy energy laws:

$$\mathcal{F}(\phi^{n+1}) \leq \mathcal{F}(\phi^n) \quad (3.13)$$

Stability and error for a numerical schemes of CH equations has done for instance in [97], while he also has proved spectral methods are suitable for interface problems, which modified potential function and non-linear part can be handled easily, and without stabilized scheme CH equation are stable in special condition, while with stabilized technique this equation is stable and follows energy law, coupling fluid flow with CH equation with considering viscosity effect has done by [69].

Numerical issue in CH equation were reported in many literatures and has been showed only a small case of solvers of fully implicit methods are gradi-

ent stable and energy decreases with time, we can find some researcher [50], who have proposed a conservative, second-order accurate fully implicit discretization of the scheme is strongly non linear and couple where non-linear stabilization term is adding to NS equation to solve based on approximate projection method, they have mentioned that it is not always unconditionally stable and requires restricted time-step size. As [28] mentioned with variables of density and viscosity that are dependent to phase field function coupling of NS and CH equations are challenging, they used a scheme, which is for phase-field simulations of two-phase incompressible flows with large density ratios based on an approximate projection method and velocity correction can be employed also for large viscosity ratio, but there isn't any theoretical proof of discrete energy law.

A semi-implicit time-discrete scheme proposed by many researcher to stabilize Cahn-Hilliard Equations, which called convex-splitting, where acting like the convex part of the free energy functional implicitly and concave part explicitly. In a recent article [24] an algorithm to implement the second order convex splitting scheme for the CH equation based on Fourier pseudo-spectral spatial, which treats the nonlinear term explicitly has been reported, and makes the computational effort more difficult.

Except of unconditionally stable first order temporal discretization schemes [29, 34] have been suggested for the CH equation, by using the special kind of splitting. These schemes are only first order accurate, later on [110] introduced a method to extend higher order accurate for discretization. In [97] has been indicated that first-order semi-implicit scheme are energy stable under reasonable conditions but by adding a stabilizing term  $s$  this condition can be removed, where  $s$  is a stabilizing parameter that should be defined specifically.

Since both Ginzburg-Landau and Cahn Hilliard equations are non-linear and only there is numerical simulation to solve them, Chen et al. [23] employed semi-implicit Fourier spectral method to solve phase field equations, but they only implicit schemes applied for elliptic operator to stability conditions and non-linear terms treated explicitly one of advantages of the Higher order semi-implicit allow us to use larger time step, while we have higher accuracy, they compared error in calculating the order parameter equilibrium profile of an interface and the spatial grid size in the finite different scheme has to be considered four times smaller in spatial method also for time step size, in their results higher order semi-implicit schemes are less stable, one of the limitation of this method was problem with sharp interface because

of using a uniform grid in spatial. Regarding to [63], chemical potential depends on type of numerical algorithm, they have applied periodic boundary condition with using pseudo-spectral method in space, and by considering numerical stability in their result, while chemical potential is sensitive to time step.

### 3.4 Spectral discretization

pseudo-spectral spatial discretization will be applied for solving Eqs. (3.5, 3.6, 3.12) : Fourier transforms will be employed along the two periodic directions of the channel geometry  $x$  and  $y$ , Chebyshev polynomials are adopted to approximate the solution along the wall-normal direction.

In order to avoid convolutions in the Fourier-Chebyshev space, the multiplication of spectral variables (i.e. convective terms) is calculated by transforming back the variables to the physical space, taking the multiplications and the re-transforming to the Fourier-Chebyshev space. This algorithm also called “pseudo-spectral algorithm”. A detail of these methods is given by [18] and [32]. Fourier Transform along periodic directions  $x$  and  $y$  for a signal  $g$  will reads:

$$g(x, y, z) = \sum_{n_x = \frac{-N_x}{2} + 1}^{\frac{N_x}{2}} \sum_{n_y = \frac{-N_y}{2} + 1}^{\frac{N_y}{2}} \hat{g}(k_x, k_y, z) e^{j(k_x x + k_y y)}, \quad (3.14)$$

where  $j = \sqrt{-1}$  is the imaginary unit of the complex representation,  $\hat{g}$  is the Fourier coefficient of the signal in the modal coordinates  $(k_x, k_y)$ ; at this point dependence on the physical coordinate of  $z$  is still available. The two periodic directions are treated with a Fast Fourier Transform (FFT) algorithm imposing periodicity lengths of  $L_x$  and  $L_y$  and projecting the velocity vector on to  $N_x$  and  $N_y$  the Fourier transform, the variables are mapped an a uniform grid in the physical space and the nodes spacing is:

$$\Delta x = \frac{L_x}{N_x - 1} \quad \Delta y = \frac{L_y}{N_y - 1} \quad (3.15)$$

The signal is decomposed in a sum of periodical functions characterized by wavenumber and amplitude; the former represents the frequency of the corresponding harmonic, whereas the latter is the magnitude of the harmonic. Each mode has the wave number along  $x$  and  $y$  by:

$$k_x = \frac{2\pi n_x}{L_x} \quad k_y = \frac{2\pi n_y}{L_y} \quad (3.16)$$

With the knowledge that the Fourier basis is orthogonal, the Fourier transform  $\hat{g}$  yields:

$$\hat{g}(x, y, z) = \frac{1}{N_x N_y} \sum_{n_x = \frac{-N_x}{2} + 1}^{\frac{N_x}{2}} \sum_{n_y = \frac{-N_y}{2} + 1}^{\frac{N_y}{2}} g(x, y, z) e^{-j(k_x x + k_y y)}. \quad (3.17)$$

Along the wall normal direction  $z$ , the transformed signal  $\hat{g}(x, y, z)$  is approximated through the sum of Chebyshev polynoms  $T_n(z)$ :

$$\hat{g}(x, y, z) = \sum_{n_z=0}^{N'_z} h(k_x, k_y, n_z) T_n(z), \quad (3.18)$$

where the prime presents the first term halving. The Chebyshev polynomial of order  $n_z$  in  $z$  direction obtained in following:

$$T_n(z) = \cos[n_z \arccos(z)], \quad (3.19)$$

where  $n_z$  is one of the  $N_z$  Chebyshev modes and  $-1 \leq z \leq 1$ . The orthogonality property keeps also for the Chebyshev polynomials and the inverse transform will be:

$$\hat{h}(k_x, k_y, n_z) = \frac{2}{N_z} \sum_{n_z=0}^{N'_z} \hat{g}'(k_x, k_y, z) T_n(z). \quad (3.20)$$

The variables described in the Chebyshev space are mapped in the physical space, related mapping is:

$$z = \cos\left(\frac{n_z \pi}{N_z}\right) \quad (3.21)$$

With adoption of Chebyshev polynomials for the approximated solution along the wall-normal direction, the spatial discretization will be determined by a large resolution near the wall region: ( $z = \pm 1$ ), where large velocity gradients need to be resolved, all detail of solution can be find in [13]. Finally, adopting the transformations of Eq. (3.14) and Eq. (3.18), the

transformed of a three-dimensional signal reads:

$$g(x, y, z, t) = \sum_{n_x = \frac{-N_x}{2} + 1}^{\frac{N_x}{2}} \sum_{n_y = \frac{-N_y}{2} + 1}^{\frac{N_y}{2}} \sum_{n_z = 0}^{N'_z} \hat{h}(k_x, k_y, n_z, t) T_{n_z} e^{-j(k_x x + k_y y)}. \quad (3.22)$$

The nonlinear terms in Eq. (3.22) are computed in the rotational form [74] to preserve the conservation property of mass, energy and circulation numerically. In addition, the number of collocation points is expanded by a factor of before transforming into the physical space to avoid the aliasing errors involved in computing the nonlinear terms pseudo-spectrally. The related computation also used for Chebyshev transform [13], which has been explained in App. A.

## 3.5 Discretization and solution of the equations

### 3.5.1 Velocity equation

Using the spectral, which presented in Sect. 3.4, Eq. (3.6) arrives:

$$\begin{aligned} \frac{\partial}{\partial t} \left( \frac{\partial^2}{\partial z^2} - k_{xy}^2 \right) \hat{w} &= \left( \frac{\partial^2}{\partial z^2} - k_{xy}^2 \right) \hat{S}_z \\ &\quad - \frac{\partial}{\partial z} (i k_x \hat{S}_x + i k_y \hat{S}_y + \frac{\partial}{\partial z} \hat{S}_z) \\ &\quad + \frac{1}{Re_\tau} \left( \frac{\partial^2}{\partial z^2} - k_{xy}^2 \right) \left( \frac{\partial^2}{\partial z^2} - k_{xy}^2 \right) \hat{w} \end{aligned} \quad (3.23)$$

where  $k_{xy}^2 = k_x^2 + k_y^2$ . The equation above emphasis that the z derivatives are taken in a different way, due to the adoption of Chebyshev polynomials. Eq. (3.23) is discretized in time adopting an hybrid IMPLICIT EXPLICIT (IMEX) scheme: Time will be advanced by using Adams-Bashforth scheme for the non-linear convective terms and implicit Crank-Nicholson scheme for the

linear viscous terms. The time-discretized form of Eq. (3.23) will be:

$$\begin{aligned}
\frac{\hat{w}^{n+1} - \hat{w}^n}{\Delta t} &= \frac{3}{2} \left( \frac{\partial^2}{\partial z^2} - k_{xy}^2 \right) \hat{S}_z^n \\
&\quad - \frac{1}{2} \left( \frac{\partial^2}{\partial z^2} - k_{xy}^2 \right) \hat{S}_z^{n-1} \\
&\quad - \frac{3}{2} \frac{\partial}{\partial z} (ik_x \hat{S}_x^n + ik_y \hat{S}_y^n + \frac{\partial}{\partial z} \hat{S}_z^n) \\
&\quad + \frac{1}{2} \frac{\partial}{\partial z} (ik_x \hat{S}_x^{n-1} + ik_y \hat{S}_y^{n-1} + \frac{\partial}{\partial z} \hat{S}_z^{n-1}) \\
&\quad + \frac{1}{Re_\tau} \left( \frac{\partial^2}{\partial z^2} - k_{xy}^2 \right) \left( \frac{\partial^2}{\partial z^2} - k_{xy}^2 \right) \frac{\hat{w}^{n+1} - \hat{w}^n}{2}
\end{aligned} \tag{3.24}$$

Where superscripts  $n - 1$ ,  $n$ ,  $n + 1$  indicate the three consecutive time levels  $t - \Delta t$ ,  $t + \Delta t$ , respectively and  $\Delta t$ , is the time-step. Eq. (3.24) is rearranged and, introducing the coefficient  $\gamma = \frac{\Delta t}{2Re_\tau}$ , arrives:

$$\begin{aligned}
\left( \frac{\partial^2}{\partial z^2} - k_{xy}^2 \right) \hat{w}^{n+1} &= \frac{3\Delta t}{2} \left( \frac{\partial^2}{\partial z^2} - k_{xy}^2 \right) \hat{S}_z^n \\
&\quad - \frac{\Delta t}{2} \left( \frac{\partial^2}{\partial z^2} - k_{xy}^2 \right) \hat{S}_z^{n-1} \\
&\quad - \frac{3\Delta t}{2} \frac{\partial}{\partial z} (ik_x \hat{S}_x^n + ik_y \hat{S}_y^n + \frac{\partial}{\partial z} \hat{S}_z^n) \\
&\quad + \frac{\Delta t}{2} \frac{\partial}{\partial z} (ik_x \hat{S}_x^{n-1} + ik_y \hat{S}_y^{n-1} + \frac{\partial}{\partial z} \hat{S}_z^{n-1}) \\
&\quad + \left[ \gamma \frac{\partial^2}{\partial z^2} + (1 - k_{xy}^2) \right] \left( \frac{\partial^2}{\partial z^2} - k_{xy}^2 \right) \hat{w}^n.
\end{aligned} \tag{3.25}$$

The discretized continuity Eq. (3.7) is:

$$ik_x \hat{u} + ik_y \hat{v} + \frac{\partial w}{\partial z} = 0, \tag{3.26}$$

substituting Eq. (3.26) into Eq. (3.27) and introducing the coefficient  $\lambda^2 = \frac{(1+\gamma k_{xy}^2)}{\gamma}$  the following is obtained:

$$\begin{aligned}
&-\gamma \left( \frac{\partial^2}{\partial z^2} - \lambda^2 \right) \left( \frac{\partial^2}{\partial z^2} - k_{xy}^2 \right) \hat{w}^{n+1} = \\
&\quad - k_{xy}^2 \left( \frac{3}{2} \hat{S}_z^n - \frac{1}{2} \hat{S}_z^{n-1} \right) \Delta t - k_{xy}^2 \left[ \gamma \frac{\partial^2}{\partial z^2} + (1 - \gamma k_{xy}^2) \right] \hat{w}^n \\
&\quad - \frac{\partial}{\partial z} ik_x \left( \frac{3}{2} \hat{S}_x^n - \frac{1}{2} \hat{S}_x^{n-1} \right) \Delta t - \frac{\partial}{\partial z} ik_x \left( \gamma \frac{\partial^2}{\partial z^2} + (1 - \gamma k_{xy}^2) \right) \hat{u}^n \\
&\quad - \frac{\partial}{\partial z} ik_y \left( \frac{3}{2} \hat{S}_y^n - \frac{1}{2} \hat{S}_y^{n-1} \right) \Delta t - \frac{\partial}{\partial z} ik_y \left( \gamma \frac{\partial^2}{\partial z^2} + (1 - \gamma k_{xy}^2) \right) \hat{v}^n.
\end{aligned} \tag{3.27}$$

$\hat{H}_x^n$ ,  $\hat{H}_y^n$  and  $\hat{H}_z^n$  are as follows:

$$\begin{aligned}\hat{H}_x^n &= \left(\frac{3}{2}\hat{S}_x^n - \frac{1}{2}\hat{S}_x^{n-1}\right)\Delta t + \left[\gamma\frac{\partial^2}{\partial z^2} + (1 - \gamma k_{xy}^2)\right]\hat{w}^n \\ \hat{H}_y^n &= \left(\frac{3}{2}\hat{S}_y^n - \frac{1}{2}\hat{S}_y^{n-1}\right)\Delta t + \left[\gamma\frac{\partial^2}{\partial z^2} + (1 - \gamma k_{xy}^2)\right]\hat{v}^n \\ \hat{H}_z^n &= \left(\frac{3}{2}\hat{S}_z^n - \frac{1}{2}\hat{S}_z^{n-1}\right)\Delta t + \left[\gamma\frac{\partial^2}{\partial z^2} + (1 - \gamma k_{xy}^2)\right]\hat{w}^n\end{aligned}\quad (3.28)$$

introducing Eqs. (3.28,3.27) reads:

$$\left(\frac{\partial^2}{\partial z^2} - \lambda^2\right)\left(\frac{\partial^2}{\partial z^2} - k_{xy}^2\right)\hat{w}^{n+1} = \frac{1}{\gamma}\left[k_{xy}^2\hat{H}_z^n + \frac{\partial}{\partial z}(ik_x\hat{H}_x^n + ik_y\hat{H}_y^n)\right] \quad (3.29)$$

With  $\hat{H}_z^n = k_{xy}^2\hat{H}_z^n + \frac{\partial}{\partial z}(ik_x\hat{H}_x^n + ik_y\hat{H}_y^n)$ , the final form of the discretized Eq. (3.8) reaches to:

$$\left(\frac{\partial^2}{\partial z^2} - \lambda^2\right)\left(\frac{\partial^2}{\partial z^2} - k_{xy}^2\right)\hat{w}^{n+1} = \frac{\hat{H}_z^n}{\gamma}. \quad (3.30)$$

By defining the auxiliary variable  $\hat{\theta} = \left(\frac{\partial^2}{\partial z^2} - k_{xy}^2\right)\hat{w}^{n+1}$  the 4<sup>th</sup>-order equation can be split in two 2<sup>th</sup> order equations:

$$\left(\frac{\partial^2}{\partial z^2} - \lambda^2\right)\hat{\theta} = \frac{\hat{H}_z^n}{\gamma}. \quad (3.31)$$

$$\left(\frac{\partial^2}{\partial z^2} - k_{xy}^2\right)\hat{w}^{n+1} = \hat{\theta}. \quad (3.32)$$

By imposing the following boundary conditions Eq. (3.32) arrives:

$$\hat{w}^{n+1}(\pm 1) = 0, \quad \frac{\partial \hat{w}^{n+1}}{\partial z}(\pm 1) = 0, \quad (3.33)$$

Where they come from non-slip condition at the wall and from the continuity equation, which has been coupled with the non-slip condition at the wall. The solution of Eq. (3.32) needs a set of boundary conditions on  $\hat{\theta}$  that lack in the physical model definition. To find a way around this problem,  $\hat{\theta}$  will be as follows:

$$\hat{\theta} = \hat{\theta}_1 + \hat{A}\theta_2 + \hat{B}\theta_3, \quad (3.34)$$

Hence,  $\hat{A}$  and  $\hat{B}$  are complex constants needs to be determined in computation. The three components,  $\hat{\theta}_1$ ,  $\hat{\theta}_2$  and  $\hat{\theta}_3$  are the special solution and two homogeneous solution of Eq. (3.31), respectively. Their solution is obtained

as follows:

$$\left(\frac{\partial^2}{\partial z^2} - \lambda^2\right)\hat{\theta}_1 = \frac{\hat{H}^n}{\gamma} \quad \hat{\theta}_1(1) = 0, \quad \hat{\theta}_1(-1) = 0, \quad (3.35)$$

$$\left(\frac{\partial^2}{\partial z^2} - \lambda^2\right)\theta_2 = 0 \quad \theta_2(1) = 0, \quad \theta_2(-1) = 1, \quad (3.36)$$

$$\left(\frac{\partial^2}{\partial z^2} - \lambda^2\right)\theta_3 = 0 \quad \theta_3(1) = 1, \quad \theta_3(-1) = 0, \quad (3.37)$$

With similar procedure, also  $\hat{w}$  can be rewritten as a sum of a special solution  $\hat{w}_1$  and two homogeneous solutions  $\hat{w}_2, \hat{w}_3$ :

$$\hat{w}^{n+1} = \hat{w}_1 + \hat{A}w_2 + \hat{B}w_3. \quad (3.38)$$

Similar to the solution of  $\hat{\theta}$  the solution for  $\hat{w}_1, w_2$  and  $w_3$  can be obtained with imposing the no-slip BC:

$$\left(\frac{\partial^2}{\partial z^2} - \lambda^2\right)\hat{w}_1 = \hat{\theta}, \quad \hat{w}_1(1) = 0, \quad \hat{w}_1(-1) = 0, \quad (3.39)$$

$$\left(\frac{\partial^2}{\partial z^2} - \lambda^2\right)w_2 = 0, \quad w_2(1) = 0, \quad w_2(-1) = 0, \quad (3.40)$$

$$\left(\frac{\partial^2}{\partial z^2} - \lambda^2\right)w_3 = 0, \quad w_3(1) = 0, \quad w_3(-1) = 0, \quad (3.41)$$

The unknown constants  $\hat{A}$  and  $\hat{B}$  are determined applying the  $\frac{\partial \hat{w}}{\partial z} = 0$  and determined boundary conditions:

$$\begin{aligned} \frac{\partial \hat{w}_1}{\partial z}(1) + \hat{A} \frac{\partial w_2}{\partial z}(1) + \hat{B} \frac{\partial w_3}{\partial z}(1) &= 0, \\ \frac{\partial \hat{w}_1}{\partial z}(-1) + \hat{A} \frac{\partial w_2}{\partial z}(-1) + \hat{B} \frac{\partial w_3}{\partial z}(-1) &= 0. \end{aligned} \quad (3.42)$$

$\hat{w}^{n+1}$  will be obtained from Eq. (3.38). The solutions of Eqs. (3.35-3.37) and Eqs. (3.39-3.41) are obtained adopting the Chebysev-Tau method, which after transforming to Fourier series in the homogeneous directions. It will be reduced to a tridiagonal system with one full row after decoupling the even and odd modes of the Chebychev coefficients. which has been proposed by [51] and the resulting tridiagonal equations, system is solved adopting the Gauss elimination procedure.

### 3.5.2 Vorticity equation

The wall-normal vorticity component  $\hat{\omega}_z$  is obtained solving Eq. (3.37); following the discretization described in Sect. 3.5.1, Eq. (3.37) arrives:

$$\left(\frac{\partial^2}{\partial z^2} - \lambda^2\right)\hat{\omega}_z^{n+1} = \frac{1}{\gamma}[ik_x\hat{H}_y^n - ik_y\hat{H}_x^n], \quad (3.43)$$

The solution of Eq. (3.43) is obtained adopting the Chebyshev-Tau algorithm, which the boundary conditions are satisfied as:

$$\hat{\omega}_z^{n+1}(\pm 1) = ik_x\hat{v}^{n+1} - ik_y\hat{u}^{n+1} = 0. \quad (3.44)$$

The resulting tridiagonal equations system is then solved adopting a Gauss elimination technique. Once the wall-normal vorticity component  $\hat{\omega}_z$  is computed, the other two velocity components  $\hat{u}^{n+1}$  and  $\hat{v}^{n+1}$  can be obtained from the spectral form of the vorticity definition and the spectral form of the continuity equation:

$$ik_x\hat{v}^{n+1} - ik_y\hat{u}^{n+1} = \hat{\omega}_z^{n+1}, \quad (3.45)$$

$$-ik_x\hat{u}^{n+1} + ik_y\hat{v}^{n+1} = \frac{\partial\hat{\omega}_z^{n+1}}{\partial z}, \quad (3.46)$$

## 3.6 Cahn-Hilliard equation

Spectral methods are used to discretize Eq. (3.11), which shown in Sect. ?? and applied in Sect. 3.5.1 and Sect. 3.5.2:

$$\begin{aligned} \frac{\partial\hat{\phi}}{\partial t} &= \hat{S}_\phi + \frac{s}{Pe_\tau}\left(\frac{\partial^2}{\partial z^2} - k_{xy}^2\right)\hat{\phi} \\ &- \frac{Ch^2}{Pe_\tau}\left(\frac{\partial^2}{\partial z^2} - k_{xy}^2\right)\left(\frac{\partial^2}{\partial z^2} - k_{xy}^2\right)\hat{\phi}, \end{aligned} \quad (3.47)$$

There are many challenges for solving numerically the Cahn–Hilliard equation because of containing a fourth order derivative term and trying to circumvent the problem of the non-linearity coming from the double-well function  $f_0$  and keeping bounded solution.

In the case of periodic boundary conditions in one direction but aperiodic boundary conditions in the other, a Fourier spectral method along the former coordinate and a Chebyshev-Galerkin will be used along the latter, with a first-order Adams–Bashforth (*BDF*) for the time derivatives, here we follow the presented method by [113], which the fourth-order Cahn–Hilliard

equation has been decomposed into two Helmholtz equations [96], the algorithm is based on what has been explained in the work of [28] and the non-linear convective  $S_\phi$  term is discretized by adopting a 2<sup>th</sup> order Adams-Bashfort. The time-discretized form of Eq. (3.47) will be:

$$\begin{aligned} \frac{\hat{\phi}^{n+1} - \hat{\phi}^n}{\Delta t} &= \frac{3}{2}\hat{S}_\phi^n - \frac{1}{2}\hat{S}_\phi^{n-1} + \frac{s}{Pe_\tau} \left( \frac{\partial^2}{\partial z^2} - k_{xy}^2 \right) \hat{\phi}^{n+1} \\ &\quad - \frac{Ch^2}{Pe_\tau} \left( \frac{\partial^2}{\partial z^2} - k_{xy}^2 \right) \left( \frac{\partial^2}{\partial z^2} - k_{xy}^2 \right) \hat{\phi}^{n+1}, \end{aligned} \quad (3.48)$$

where  $s$  will be considered as a positive number and enhances stability, introducing the coefficient  $\gamma_\phi = \frac{\Delta t Ch^2}{Pe_\tau}$ , Eq. (3.48) will be:

$$\left[ \frac{1}{\gamma_\phi} - \frac{s}{Ch^2} \left( \frac{\partial^2}{\partial z^2} - k_{xy}^2 \right) + \left( \frac{\partial^2}{\partial z^2} - k_{xy}^2 \right)^2 \right] \hat{\phi}^{n+1} = \frac{\hat{H}_\phi}{\gamma_\phi} \quad (3.49)$$

where the historical term  $\hat{H}_\phi$  has been introduced :

$$\frac{\hat{H}_\phi}{\gamma_\phi} = \frac{1}{\gamma_\phi} \left( \hat{\phi}^n + \frac{3\Delta t}{2}\hat{S}_\phi^n - \frac{\Delta t}{2}\hat{S}_\phi^{n-1} \right) \quad (3.50)$$

Therefore by defining the auxiliary variable  $\theta_\phi = \lambda_\phi \phi + \nabla^2 \phi$  the 4<sup>th</sup> order Eq. (3.49) can be split in two 2<sup>th</sup> order equations:

$$\left( \frac{\partial^2}{\partial z^2} - k_{xy}^2 - \lambda_\phi - s \right) \hat{\theta}_\phi = \frac{\hat{H}_\phi}{\gamma_\phi}, \quad (3.51)$$

$$\left( \frac{\partial^2}{\partial z^2} - k_{xy}^2 - \lambda_\phi \right) \hat{\phi}^{n+1} = \hat{\theta}_\phi, \quad (3.52)$$

Such that  $\hat{\phi}^{n+1}$  will be cancelled from Eq. (3.49) and  $\hat{\theta}_\phi$  will be computed explicitly from  $\hat{\phi}^n$  and Eqs. (3.51, 3.52) will be solved through a Chebyshev-Tau algorithm.

In order to recovery Eq. (3.47), the two values of  $\lambda_\phi$  yields by solving the equation:

$$\gamma_\phi \lambda_\phi^2 - s \gamma_\phi \lambda_\phi + 1 = 0 \quad (3.53)$$

$$\lambda_{\phi 1,2} = -\frac{s}{2} \pm \sqrt{\frac{s^2 \gamma_\phi^2 - 4\gamma_\phi}{2\gamma_\phi}}, \quad (3.54)$$

To have real solution of Eq. (3.53), it will be required to:

$$s \geq \sqrt{\frac{4Pe_\tau}{\Delta t Ch^2}} = \sqrt{\frac{4}{\gamma_\phi}} \quad (3.55)$$

Therefore,  $\lambda_{\phi_1} = \lambda_{\phi_2} = -s/2 = \sqrt{\frac{Pe_\tau}{\Delta t Ch^2}}$ . Eq. (3.52) will be solved by imposing the following boundary conditions that appears in using no-flux condition for  $\phi$  and  $\mu$ :

$$\frac{\partial \hat{\phi}^{n+1}}{\partial z}(\pm 1) = 0, \quad \frac{\partial^3 \hat{\phi}^{n+1}}{\partial z^3}(\pm 1) = 0 \quad (3.56)$$

Again, here is necessary to set a BC that lack in physical model definition, which the procedure is same as Eq. (3.31). Chebyshev-Tau algorithm will be employed to solve Eq. (3.51) and Eq. (3.52).

### 3.6.1 Simulation parameters and accuracy

The Reynolds number can be set considering the flow field and the geometry; once the friction Reynolds number is fixed, the surface tension  $\sigma$  can be imposed through the Weber number. The interface thickness depends, in general, on the problem under analysis and it may assume values ranging several orders of magnitude; this work focuses on the study of immiscible binary mixtures, where the physical interface has a real thickness of  $O(Ch^{-9})$ . This interface thickness would require numerical resolutions beyond the current computational limits. As a result a fictitious enlargement of the interface is required and the the Cahn number should be set to the minimum value allowed by the numerical scheme adopted, that in general is at least of three mesh points.

In this analyses,  $Re$ ,  $We$ ,  $Ch$  and  $Pe_\tau$  are macroscopic input parameters defined considering the physical fluid properties, the flow regime, the simulated surface tension and the diffuse interface modelling. Once fixed the shear Reynolds number, the value of the surface tension will be chosen by the Weber number. When considering immiscible fluids, the interface thickness depends on the numerical algorithm only, thus the Cahn number can be fixed to the smallest possible value. To overcome this lack of physical meaning and keep the results independent from the interface thickness, a proper scaling between  $Ch$  and  $Pe_\tau$  should be adopted. Effective Peclete ( $Pe_\tau$ ) number of system is  $\frac{Ch}{\mathcal{M}}$ . In model of [69], which the sharp interface is replaced by a narrow transition layer across and the fluids may mix this ratio should be extremely small. Later on [40] showed while mobility affects the thickness and perturbation magnitude of the chemical potential

boundary layers to optimise that interface thickness reduces at a slower rate than the mesh size, so as to obtain a more and more accurate estimation of the interfacial  $\mathcal{M}$  applied in his solution with decreasing a power of the interface thickness. Three scaling compared by [47]:  $Pe_\tau \propto Ch$ ,  $Pe_\tau \propto Ch^2$  and  $Pe_\tau \propto Ch^{-1}$  and he mentioned further investigations are required to develop a scaling and can capture topological transitions.

Finding a consistent and practically useful theory of how these objectives can be achieved by suitable, intrinsically related choices of the parameters  $Ch$  and  $\mathcal{M}$  has been introduced by [71], which explains in following: Selecting large value of  $\mathcal{M}$  turns to excessive numerical dissipation while selecting small  $\mathcal{M}$  and  $Ch$ , but finite, the inner layer dynamics is kept alive in the complete diffuse-interface model, which leads to allow topological changes of the interface while retaining the correct interfacial dynamics away from such singular events, finally he showed choosing proper  $Pe_\tau$  like as  $Pe_\tau \propto Ch^{-1}$  results to the formal identification of the distinguished limit and correct surface tension will be provided for the solution.



---

# 4

## Results and Discussion

In this work we use Direct Numerical Simulation (DNS) to study the turbulent Poiseuille flow of two immiscible liquid layers inside a rectangular channel. A thin liquid layer (fluid 1) flows on top of a thick liquid layer (fluid 2), such that their thickness ratio is  $h_2/h_1 = 9$ . The two liquid layers have the same density but different viscosities (viscosity-stratified fluids). In particular, we consider three different values of the viscosity ratio  $\lambda = \nu_1/\nu_2$ :  $\lambda = 1$ ,  $\lambda = 0.875$  and  $\lambda = 0.75$ . Numerical Simulations are based on a Phase Field method to describe the interaction between the two liquid layers. In the following chapter, we first present a test case to validate the proposed numerical method, in Sect. 4.2 results of the interaction between the two liquid layers and turbulence modulation inside the channel has been discussed, where producing recirculation and inversion of the wall shear stress at top wall by the wall-interface interaction has shown in Sect. 4.3. Finally in Sect. 4.4 numerical Simulations of weak wave turbulence has been compared to theoretical results.

### 4.1 Benchmark

As a fundamental for applications to a series of numerical experiments in two phase flow simulation, the accuracy and the validity of the numerical methods considering the conservation laws of mass and energy in the computing domain has to be evaluated. In the following, the accuracy of the simulation is checked with comparing the evolution of the interface of capillary wave with theoretical values [87].

### 4.1.1 Analytical solution for capillary wave

Capillary waves are similar to gravity waves but, smaller scales in length and time has been involved for them, also computing of capillary waves is more difficult, because surface tension forces are based on the interface curvature, which needs more accuracy.

Two phase flow system is considered in analytical solution, if we consider a standing small-amplitude wave with surface displacement, elevation  $\eta$  is the distance between the water surface and the mean water depth  $H$  which is the height between the trough and the crest of the standing wave in the water depth  $d$  and  $L$  is the horizontal distance between two successive wave crests. if we consider a standing small-amplitude wave, with water surface elevation  $\eta$ :

$$\eta(x, t) = \frac{H}{2} \cos(ky) \cos(\omega t) \quad (4.1)$$

With  $\omega = \frac{2\pi}{T}$  is angular frequency and  $k$  is wave number at  $t = 0$  as shown in Fig. 4.1. also if we make attention to The limitation to small-amplitude requires that the ratio of the maximum elevation to the wavelength condition ( $\frac{H}{\lambda} \ll 1$ ) and with assumption of the linear wave theory, fluid is supposed to be homogeneous and incompressible.

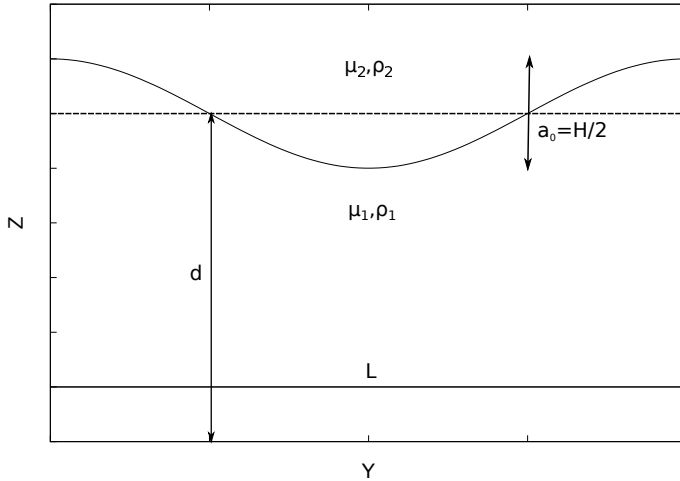


FIGURE 4.1 – Initial conditions for the liquid-liquid interface  $\eta(x, 0)$ .

For finite depth small capillary wave was predicted by [60] with a gen-

eralized analytical value of the frequency is defined by:

$$\omega_{th}^2 = \frac{\sigma k^3}{\rho_1 + \rho_2} \tanh(kd) \quad (4.2)$$

with  $\sigma$  is surface tension,  $\rho_1$  and  $\rho_2$  are densities of two phases and  $k$  is wave number. Later on the effects of the viscosity on the evolution of the amplitude of a capillary wave calculated by [87] for two phase flow with equal kinematic viscosities  $\nu = \nu_2 = \nu_1$ , with introducing frequency of wave  $\omega_{th}^2 = \frac{\sigma k^3}{\rho_1 + \rho_2}$ , while he considered a dimensionless viscosity, which is defined by  $\epsilon$ :

$$\epsilon = \frac{\nu k^2}{\omega_{th}} \quad (4.3)$$

in his calculation amplitude of the considered capillary wave  $a(t)$  is:

$$a(t) = \frac{\eta(x, t)}{\eta(x, 0)} \quad (4.4)$$

with considering  $\tau = \omega_{th} t$ , this amplitude is given by:

$$\frac{a(\tau)}{a_0} = \frac{4(1-4\beta)\epsilon^2}{8(1-4\beta)\epsilon^2 + 1} \operatorname{erfc}(\sqrt{\epsilon\tau}) + \sum_{i=4}^4 \frac{z_i}{Z_i} \frac{\omega_{th}}{z_i^2 - \epsilon\omega_{th}} \exp\left((z_i^2 - \epsilon\omega_{th}) \frac{\epsilon}{\omega_{th}}\right) \operatorname{erf}\left(z_i \sqrt{\frac{\tau}{\omega_{th}}}\right), \quad (4.5)$$

$\operatorname{erfc}$  is complementary error function.  $z_i$  are the four roots of the algebraic following equation:

$$z^4 - 4\beta(k^2\nu)^{\frac{1}{2}} z^3 + 2(1-6\beta)k^2\nu z^2 + 4(1-3\beta)(k^2\nu)^{\frac{3}{2}} z + (1-4\beta)\nu^2 k^4 + \omega^2 = 0 \quad (4.6)$$

The coefficient  $Z_1$  is given by  $Z_1 = (z_2 - z_1)(z_3 - z_1)(z_4 - z_1)$ , and the other coefficients  $Z_2$ ,  $Z_3$  and  $Z_4$  are obtained by circular permutation of the indices. The dimensionless parameter  $\beta$  is:

$$\beta = \frac{\rho_1 \rho_2}{(\rho_1 + \rho_2)^2} \quad (4.7)$$

#### 4.1.2 Non-viscous and viscous fluids

With considering two fluids which viscosities values are negligible  $\nu = \nu_1 = \nu_2 = 0$  capillary waves will not be damped and will oscillate with a constant frequency as followed in Eq. (4.2).

But, when the viscosities of two phases considered by  $\nu_1, \nu_2$  the evolution

of the interface at a fixed position should be compared with the viscous effect when a decay rate  $\gamma$  is expected [60].

$$\gamma = 2\nu_1 k^2 \quad (4.8)$$

### 4.1.3 Test case

Simulations are run at a reference Reynolds number  $Re_\tau = 100$  (defined based on the physical properties of fluid 1), and at Weber number  $We = 0.1$ . The value of the viscosity ratio are selected:  $\lambda = 1$ , while we consider a matched density for two fluids,  $\frac{\rho_2}{\rho_1} = 1$ .

We set  $Ch = 0.036$ , which guarantees that the interface between the two fluids is described using a minimum of 3 points in each direction, and  $Pe = 83.33$ , which minimizes the mass leakage (always below 2%).

$2D$  computational domain as square box used in our simulations has dimensions  $2h \times 2h$  along the spanwise ( $x$ ), and wall-normal ( $z$ ) directions, and is discretized using  $256 \times 257$  grid nodes. Periodic boundary conditions are used in the spanwise direction. In the wall normal direction ( $z$ ), no slip conditions are imposed for upper and lower boundaries, whereas a normal contact angle (and a zero-flux of the chemical potential) is used for  $\phi$ , with a time step  $dt = 1 \times 10^{-4}$ .

We used perturbed interface of with a sinusoidal wave, with zero initial velocity. The initial amplitude of the perturbed interface is  $H_0 = .05$  and capillary wave length will be equal to dimension of spanwise direction  $\lambda_y$ , giving  $\omega_{th} = 12.441$ , the initial condition is shown in Fig. 4.2 a), with an position of interface:

$$z = -100 + H_0 \cos(ky), \quad k = \frac{2\pi}{\lambda_y} = \pi \quad (4.9)$$

Fig. 4.2b) shows time histories of capillary waves with comparison between simulation results and the exact analytic solution, which numerical results agree with exact solution and confirms numerical method is clearly capable of accuracy simulation in the oscillatory behaviour.

Fig. 4.2b) shows time histories of capillary waves with comparison between simulation results and the exact analytic solution, which numerical results agree with exact solution and confirms numerical method is clearly capable of accuracy simulation in the oscillatory behaviour, we should mention that the difference between numerical simulation and analytical is result of considering viscosity ratio in our test case.

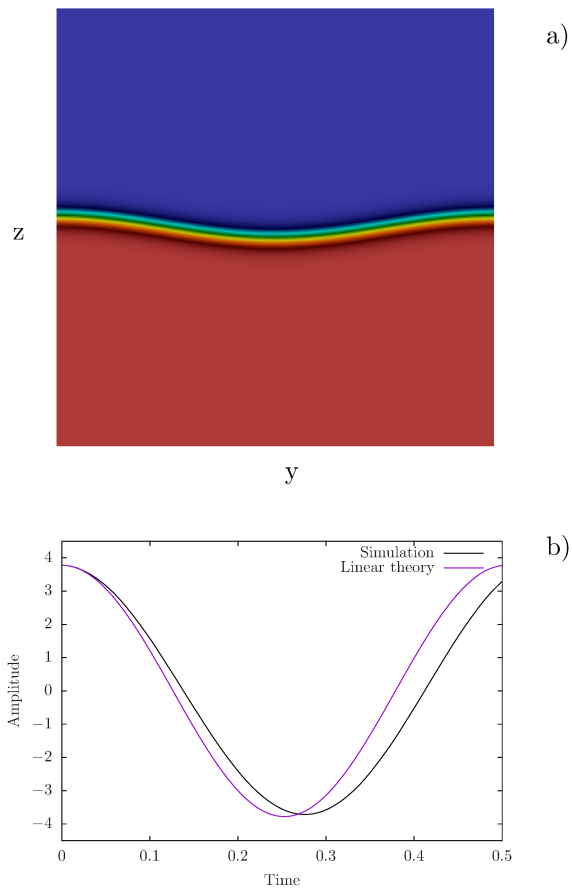


FIGURE 4.2 – Capillary wave test case in  $(z-y)$  plane ; a): Initial position of interface ; b): Computed amplitude of capillary wave, simulation versus linear theory.

## 4.2 Turbulent drag reduction

Direct Numerical Simulation (DNS) of turbulent flows has become an essential tool for the field of turbulence research and allow engineers to consider complex situations, which theoretical ideas about confined flows of cocurrent immiscible fluids are often observed in the process and petroleum industry. Important examples include oil-water separators and hydrocarbon transportation pipelines. In these situations, two-immiscible phases (typically oil and water) are driven inside pipelines/channels and interact modifying the overall mass, momentum and heat transfer properties of the system. To optimize the design of these systems it is crucial to determine whether the two phases remain separate (due to density and viscosity stratification) or form emulsions (which are difficult to process/separate). From a practical standpoint, the stratified condition (or even the core annular flow condition) is preferred for two main reasons: the required power to transfer the oil/water flow is lower (due to the lower viscosity of water wetting a wall compared to that of the oil) and oil can be easily separated from water (whereas more complex oil/water separators must be designed when water is dispersed within the oil phase).

In the present study, we want to use Direct Numerical Simulations (DNS) to analyze the dynamics of a turbulent viscosity-stratified liquid-liquid flow moving inside a flat channel. For the first time, a Phase Field approach (Cahn-Hilliard equation) is employed here to describe the liquid-liquid interaction in such configuration. The governing balance equations are solved through a pseudo-spectral method for a given value of the reference shear Reynolds number ( $Re_\tau = 100$ ) and for three different values of the viscosity ratio  $\lambda$  between the two liquid-layers ( $\lambda = 1$ ,  $\lambda = 0.875$  and  $\lambda = 0.75$ ).

Compared with the case of a single phase flow driven by the same pressure gradient, the viscosity stratified liquid-liquid flow is characterized by a larger volume flowrate, as a direct consequence of the conversion of mean kinetic energy into work to deform the liquid-liquid interface. These effects become stronger with increasing the viscosity difference between the two liquid layers.

We consider the case of two immiscible fluid layers flowing inside a rectangular channel, with the upper part of the channel occupied by fluid 1 and the lower part of the channel occupied by fluid 2 (as sketched in fig. 4.3). The interface between the two fluid is located in the upper part of the channel, and the film thickness ratio is  $h_2/h_1 = 9$ . The two fluids have the same density ( $\rho_1 = \rho_2 = \rho$ , i.e gravity is negligible), but different

viscosities ( $\nu_1 \neq \nu_2$ ). As a consequence, a viscosity ratio  $\lambda = \nu_1/\nu_2$  can be defined. To model the mixture of two immiscible, incompressible and Newtonian fluids we use a Phase Field approach. The fluid dynamics of the system is described by the dimensionless equations [40, 113, 6, 94] as also was mentioned in Sect. 2.4.

### 4.2.1 Numerical Simulation

Governing equations (Eqs. 2.18-2.20) are solved using a pseudo-spectral method (characterized by a negligible numerical dissipation and dispersion) based on transforming the field variables into wavenumber space through Fourier series in the homogeneous directions ( $x$  and  $y$ ) and Chebyshev polynomials in the wall-normal direction ( $z$ ). Integration in time is achieved using an implicit Crank-Nicolson scheme for the uniform part of the diffusive terms, and using an explicit Adams-Bashforth scheme for both the non-uniform part of the diffusive terms (in Eqs. 2.19) and the nonlinear terms. In particular, the nonlinear terms are first computed in the physical space and then transformed in the wavenumber space using a de-aliasing procedure based on the 2/3 rule; derivatives are evaluated directly in the wavenumber space to maintain spectral accuracy. The dimensionless value of the time step is  $dt = 1 \times 10^{-4}$ .

The computational domain used in our simulations has dimensions  $4\pi h \times 2\pi h \times 2h$  along the streamwise ( $x$ ), spanwise ( $y$ ) and wall-normal ( $z$ ) directions, and is discretized using  $512 \times 256 \times 257$  grid nodes, while three factors

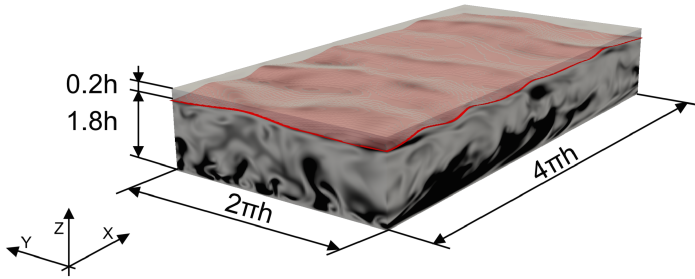


FIGURE 4.3 – Sketch of the computational domain with details of the flow configuration. A thin liquid layer with smaller viscosity (fluid 1) flows on top of a thick liquid layer with larger viscosity (fluid 2). The thickness ratio between the two liquid layers is  $h_2/h_1 = 9$ . The distribution of Turbulent Kinetic Energy (TKE) and the deformed liquid-liquid interface are also shown for visualization purposes.

influence computational grid. First, mesh size should consider small enough to resolve the important scales of motion in the flow. Second, it should be large enough that artificialities caused by boundary conditions don't impact on the statistics of the solution. Third, depends on the availability of computer resource [74]. Periodicity is applied along  $x$  and  $y$  for both  $\mathbf{u}$  and  $\phi$ . In the wall normal direction ( $z$ ), no slip conditions are enforced for  $\mathbf{u}$ , whereas a normal contact angle (and a zero-flux of the chemical potential) is used for  $\phi$ .

Simulations are run at a reference Reynolds number  $Re_\tau = 100$  (defined based on the physical properties of fluid 2, i.e. the thicker fluid layer), and at Weber number  $We = 0.1$ . This value of  $We$  has been selected to be representative of an oil-water interface [93].

Three different values of the viscosity ratio are selected:  $\lambda = 1$ ,  $\lambda = 0.875$  and  $\lambda = 0.75$ . This means that the viscosity of the thin fluid layer (fluid 1) is lower than the reference viscosity of the thick fluid layer (fluid 2). The value of  $Ch$  and  $Pe$  numbers comes from a combined physical-numerical consideration. For immiscible fluids, the interface thickness is of the order of molecular length scales, hence  $Ch \rightarrow 0$ . This would require a numerical resolution that is far beyond current computational possibilities. For this reason, we set  $Ch = 0.02$ , which guarantees that the interface between the two fluids is described using a minimum of 3 points in each direction.

Then we assumed  $Pe \propto Ch^{-1}$  to obtain a correct evaluation of the interface dynamics [93]. In the present case, we chose  $Pe = 150$ , which minimizes the mass leakage (always below 2%).

The procedure we followed to run our numerical simulations of a viscosity-stratified channel is the following:

- we run a preliminary simulation of a single phase turbulent channel flow at a given shear Reynolds number ( $Re_\tau = 100$ );
- we start the simulation of the two phase system (distribution of  $\phi$ ) initializing the order parameter such that the interface is initially located close to the upper boundary ( $h_2/h_1 = 9$ );
- turbulence adapts itself to the new physical configuration (transient behaviour) and finally reaches a new statistically steady state condition;
- after the statistically steady state condition is reached, results are collected for a long enough time window to ensure statistical convergence.

From the procedure outlined above, it is apparent that we do not need to generate turbulence or to impose a specific velocity profile in the two

liquid layers.

### 4.2.2 Turbulence statistics

All presented results in Sect. 4.2 in this thesis are in statistical situation, which are useful to better understand some of the statistical, the following visualizations are the result of direct numerical simulations of fully developed turbulence. Calculation are based on collocation points by spectral interpolation until flow reaches a statistically steady state, which can be identified by a linear profile of total shear stress,  $u'_{x,rms}u'_{z,rms} + \frac{1}{Re} \frac{\partial \bar{u}}{\partial z}$  [51]. Once the velocity field reaches the statistically steady state, the equations will be integrated further in time to achieve a running time average of the various statistical correlations. The statistical sample mostly has been obtained by averaging over streamwise and spanwise directions.

Simulations are run starting from a single phase turbulent flow at  $Re_\tau = 100$ . The order parameter  $\phi$  is initialized such that the interface is initially flat and locate at  $h_2/h_1 = 9$  (close to the upper boundary). The development of the two-phase flow at three different values of the viscosity ratio  $\lambda = 1$ ,  $\lambda = 0.875$  and  $\lambda = 0.75$  is studied. Turbulence adjusts to the new physical configuration( transient behaviour) and finally reaches a new statistically steady state condition,after which results are collected for along enough time window to ensure statistical configuration of the results.

### 4.2.3 Flow rate

We start our analysis by looking at the time evolution of the mean volume flowrate  $Q$  of the thicker fluid layer (fluid 2) across the channel section. Results, which are shown in Fig. 4.4, are normalized by the reference volume flowrate for the single phase case ( $Q_{SP}$ ) at the same reference  $Re_\tau$  ( $Re_\tau = 100$ ). Here time is in wall units,  $t^+ = t^* u_\tau^2 / \nu_2$  (with  $t^*$  the physical time expressed in seconds). We clearly observe that, even for  $\lambda = 1$ , the presence of a deformable interface (characterized by a specific surface tension) separating the two fluid layers induces an overall increase of the volume flowrate (up to  $\simeq 4\%$ ). This indicates that the wall normal transport of momentum is reduced, with a significant proportion of the mean flow energy being lost into interface deformation. For reducing  $\lambda$ , the volume flowrate further increases (up to  $\simeq 10\%$  for  $\lambda = 0.75$ ). This is a direct consequence of the presence of a thin liquid layer with lower viscosity that reduces the mean shear stress at the upper wall. Since our simulations are run with an imposed pressure gradient, reducing the wall stress produces an increase of the mean volume flowrate. The explicit computation of the wall shear stress

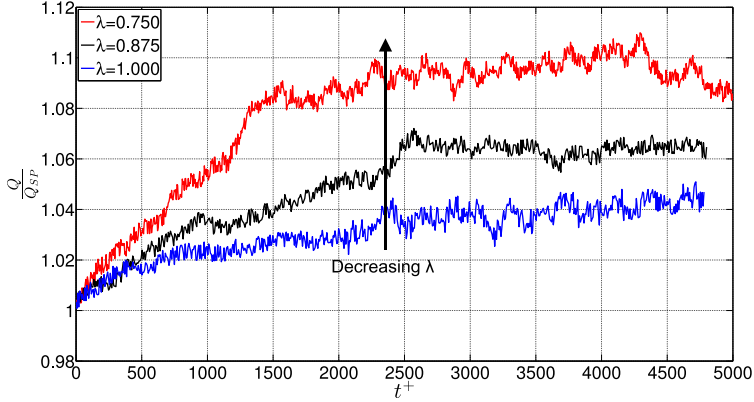


FIGURE 4.4 – Time evolution of the volume flowrate  $Q$ , normalized by the reference volume flowrate for the single phase flow  $Q_{SP}$ , for the viscosity stratified liquid-liquid flow at  $Re_\tau = 100$  and different viscosity ratios  $\lambda$ :  $\lambda = 1$ ,  $\lambda = 0.875$  and  $\lambda = 0.75$ . The arrow points in the direction of decreasing  $\lambda$  (i.e. increasing of the viscosity difference between the two fluid layers).

for the different simulations (at both the bottom and the top wall), as well as the corresponding value of the mean volume flowrate  $Q/Q_{SP}$ , is summarized in Tab. 4.1. Specifically, even for  $\lambda = 1$ , we observed an increase of the shear stress at the bottom wall [3], and a corresponding decrease of the shear stress at the top wall, such that the resulting friction is reduced. This observation supports the idea that the turbulent drag reduction is not only due to the reduced viscosity, but it is indeed due to the interaction between the interface (with a surface tension) with the near wall activity.

Simulations	$\tau_{w,2}$	$\tau_{w,1}$	$Q/Q_{SP}$
SP (Single Phase)	1	1	1
$\lambda = 1$	1.267	0.736	1.035
$\lambda = 0.875$	1.281	0.722	1.062
$\lambda = 0.75$	1.314	0.683	1.093

TABLE 4.1 – Measurements of the shear stress at the bottom wall  $\tau_{w,2}$  and the top wall  $\tau_{w,1}$  for the different flow configurations ( $\lambda = 1$ ,  $\lambda = 0.875$  and  $\lambda = 0.75$ ). Results from the single phase simulation (SP) are also shown. The value of the dimensionless volume flowrate  $Q/Q_{SP}$  corresponding to each specific simulation is also shown.

#### 4.2.4 Mean streamwise velocity profile

Linked to the observed changes of the volume flowrate, we expect large modification of the mean streamwise velocity. In Fig. 4.5 we explicitly show

the wall-normal behavior of the mean streamwise velocity  $\langle u_x \rangle$  for the three different values of  $\lambda$  considered in this study ( $\lambda = 1, \lambda = 0.875, \lambda = 0.75$ ). The wall-normal coordinate is expressed in wall units,  $z^+ = z^* u_\tau / \nu_2$  (with  $z^*$  the physical position expressed in meters). In the following, the superscript  $+$  will be dropped for ease of notation. Angular brackets  $\langle \cdot \rangle$  denote averaging in time and over the homogeneous directions. Note that the reference position of the interface is explicitly shown by the thick vertical line. Statistics in this figure, as well as in the following figures, are averaged over a time window of  $\Delta t^+ = 2000$ , after a steady state condition is reached (as visible in Fig. 4.4 for  $t^+ > 3000$ ). Where explicitly shown, arrows inside figures point in the direction of decreasing  $\lambda$  (i.e. increasing the viscosity difference between the two fluid layers). Compared to the reference case of a single phase flow (—), the presence of two different fluid layers separated by a deformable interface alters the symmetry of the profile: larger values of the velocity characterize the thick fluid layer ( $0 < z < 180$ ), whereas smaller values of the velocity characterize the thin fluid layer ( $180 < z < 200$ ). The lower is the viscosity of the thin layer in contact with the upper wall (i.e. the lower is  $\lambda$ ), the larger are the values of the mean streamwise velocity. This is consistent with the observed behavior of  $Q/Q_{SP}$  (Fig. 4.4) and indicates that the presence of two different fluid layers separated by a deformable interface suppresses the wall-normal transport of momentum compared to the case of a single phase flow at the same  $Re_\tau$ .

The suppression of wall-normal momentum transport is the consequence of the conversion of kinetic energy into work to deform the liquid-liquid interface (potential energy). Although all the simulations are run with the same driving pressure gradient (i.e. with the same reference shear Reynolds number  $Re_\tau$ ), the presence of a deformable interface separating the two liquid layers alters the slope of the mean velocity at the wall (i.e. alters the viscous wall stress). The presence of a viscosity difference between the two layers ( $\lambda \neq 1$ ) alters further the symmetry of the profile. The lower is  $\lambda$ , (i.e. the lower the viscosity of the thin layer), the larger is the mean velocity, since the rate of change of  $\langle u_x \rangle$  with  $z$  is directly linked to the local value of the viscosity. It is interesting to note that the mean streamwise velocity  $\langle u_x \rangle$  presents an inflection point at the location of the interface. This is explicitly demonstrated in Fig. 4.6 by looking at the curvature of the mean streamwise velocity profile,  $\partial^2 \langle u_x \rangle / \partial z^2$ . Differently from the case of a single phase flow where the curvature is always negative, for the liquid-liquid flow the curvature of the profile is always negative but in a thin region close to the fluid-fluid interface ( $170 < z < 180$ ), where it becomes positive (i.e.

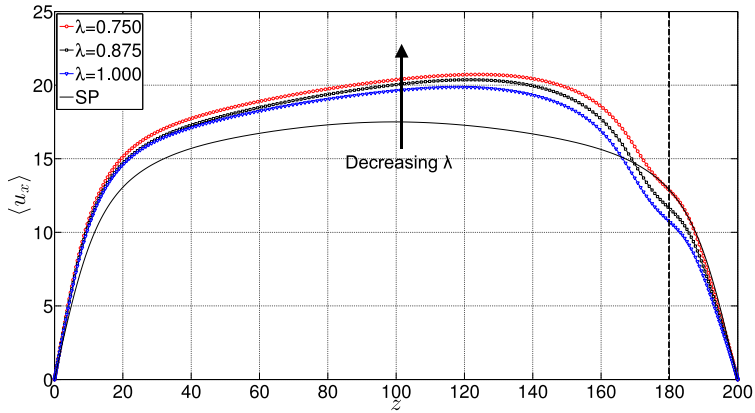


FIGURE 4.5 – Mean fluid streamwise velocity  $\langle u_x \rangle$  for the viscosity stratified liquid-liquid flow at  $Re_\tau = 100$ . Comparison between simulations at different viscosity ratios  $\lambda$ :  $\lambda = 1$  ( $-\nabla-$ ),  $\lambda = 0.875$  ( $-\square-$ ) and  $\lambda = 0.75$  ( $-\circ-$ ) Results from simulation of single phase flow at the same reference shear Reynolds number (SP,  $-$ ) are also included for comparison.

change of curvature). This behavior is primarily due to the shear exerted by the layers at the interface and will be further analyzed below within the discussion of turbulence fluctuations.

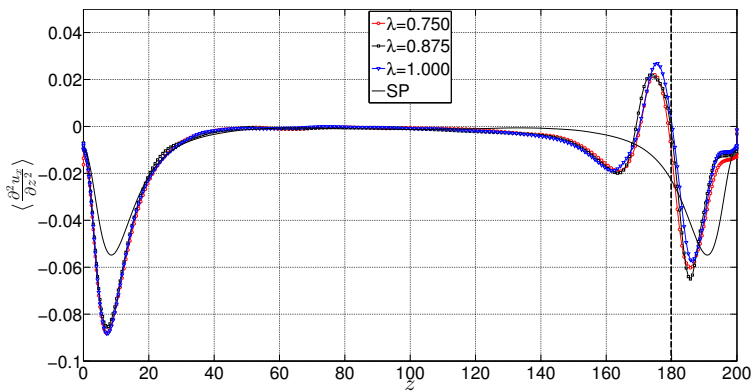


FIGURE 4.6 – Curvature of the mean fluid streamwise velocity,  $\partial^2 \langle u_x \rangle / \partial z^2$  for the viscosity stratified liquid-liquid flow at  $Re_\tau = 100$ . Lines as in Fig. 4.5.

### 4.2.5 Rms statistics

To analyze the effect of the viscosity stratification on the behavior of turbulence. The rms of the  $i$  component velocities velocity is defined as:

$$rms(u_i) = \frac{1}{u_\tau} \sqrt{(u_i - \bar{u}_i)^2} \quad (4.10)$$

we compute the root mean square (rms) of the streamwise, spanwise and wall-normal fluid velocity fluctuations as a function of the wall normal coordinate  $z$ . Results are shown in fig. 4.7. We will consider first the behavior of  $\langle u'_{x,rms} \rangle$ , panel a) in Fig. 4.7. Regardless of the value of  $\lambda$ , we clearly see that velocity fluctuations are only slightly modified (increased) near the lower wall ( $0 < z^+ < 100$ ), where typical near wall-turbulence is maintained.

The situation remarkably changes near the top wall ( $100 < z^+ < 200$ ). A first comparison is made between results from the single phase flow (solid line,  $-$ ) and results from the two-phase flow at  $\lambda = 1$  (symbols, *triangledown*). Turbulence is substantially suppressed compared to the case of a single phase flow, since in that region of the channel the deformable interface converts the kinetic energy of the mean flow into potential energy (interface deformation with considering Korteweg force). Note that a local minimum of  $\langle u'_{x,rms} \rangle$  is observed when approaching the location of the interface ( $z^+ \simeq 180$ ). The effect of decreasing  $\lambda$  is particularly pronounced in the proximity of the interface ( $140 < z^+ < 190$ ) and is twofold: it decreases turbulence fluctuations in the thin layer with lower viscosity ( $180 < z^+ < 190$ ) while decreasing it in the thick layer with larger viscosity.

For completeness, we also compute the behaviour of spanwise ( $\langle u'_{y,rms} \rangle$ , Fig. 4.7b) and wall normal velocity fluctuations ( $\langle u'_{z,rms} \rangle$ , Fig. 4.7c). A decrease of turbulence intensities is observed for both  $\langle u'_{y,rms} \rangle$  and  $\langle u'_{z,rms} \rangle$  in the liquid-liquid interface region (near the upper wall, for  $z > 120$ ). This finding agrees with the observation that the presence of the interface reduces the transport of momentum (in particular in the wall-normal direction) by converting the kinetic energy of the flow into potential energy (interface deformation). In the meantime, turbulence intensities are increased near the bottom wall, as a consequence of the increased shear rate therein ( Fig. 4.8). Note that the shape of the  $\langle u'_{y,rms} \rangle$  and  $\langle u'_{z,rms} \rangle$  profiles for different  $\lambda$  is qualitatively similar, although a clear increase of turbulence fluctuations is observed near the lower wall for decreasing  $\lambda$  (as explicitly shown in Fig. 4.7). With similar arguments, we can also explain the behavior of  $\langle u'_{x,rms} \rangle$  for different  $\lambda$ .

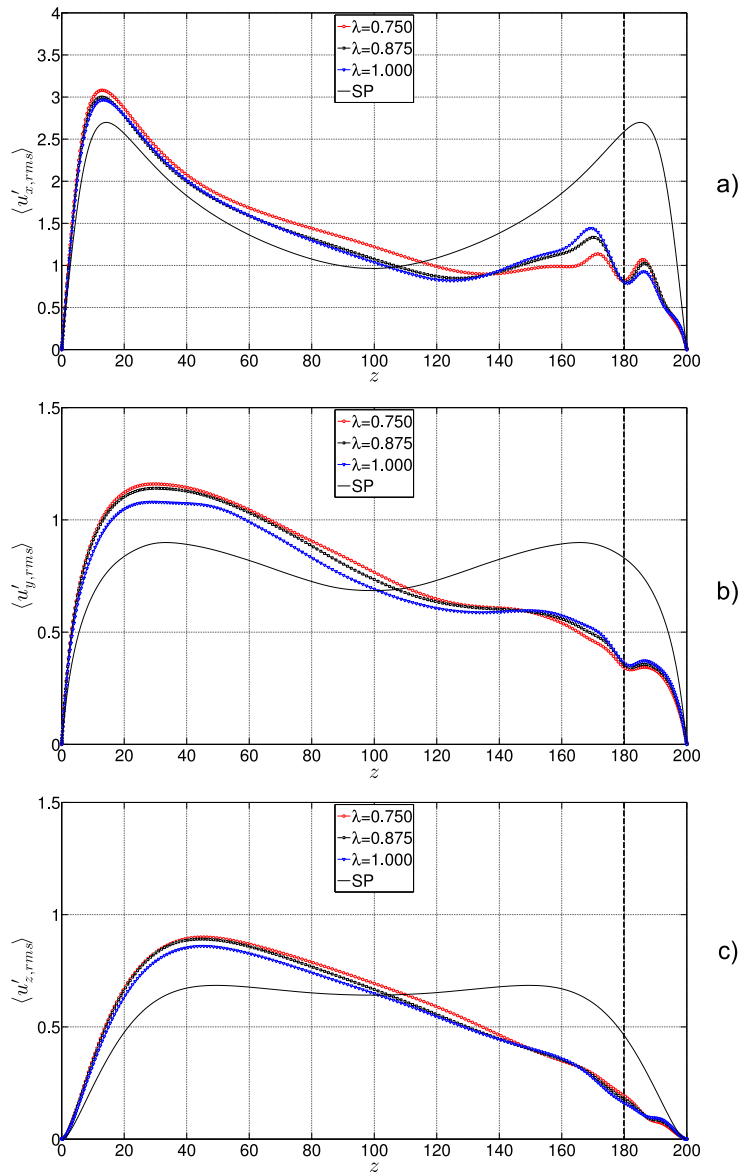


FIGURE 4.7 – Root mean square of fluid velocity fluctuations,  $\langle u'_{i,rms} \rangle$ , for the viscosity stratified liquid-liquid flow at  $Re_\tau = 100$ : a) streamwise component,  $\langle u'_{x,rms} \rangle$ ; b) spanwise component,  $\langle u'_{y,rms} \rangle$ , a) wall-normal component,  $\langle u'_{z,rms} \rangle$ . Lines as in Fig. 4.5.

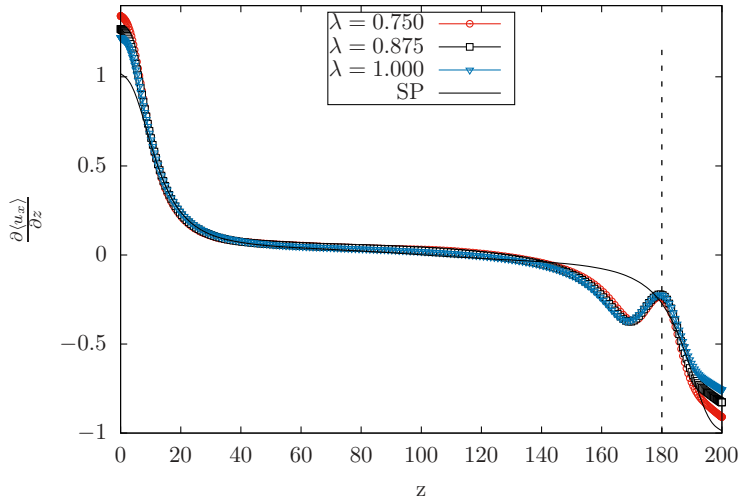


FIGURE 4.8 – Wall-normal behavior of the mean strain rate,  $\gamma_{xz} = \partial \langle u_x \rangle / \partial z$  for the viscosity stratified liquid-liquid flow at  $Re_\tau = 100$ . Lines as in Fig. 4.5.

### 4.2.6 Strain rate

With computing our simulation to examine stress profile, we found a link can be drawn between the behavior of the turbulent fluctuations in the streamwise direction and the behavior of the mean flow strain rate  $\gamma_{xz} = \partial \langle u_x \rangle / \partial z$ , which is shown in Fig. 4.8. As far as the mean strain rate  $\gamma_{xz}$  is concerned, the behavior in the single phase flow (– in Fig. 4.8) is well known:  $|\gamma_{xz}|$  decreases sharply in the near wall regions while attaining an almost constant value  $|\gamma_{xz}| \simeq 0$  in the core of the channel. Compared to the single phase flow, for the case of the viscosity stratified liquid-liquid layer  $|\gamma_{xz}|$  is increased near the bottom wall ( $z^+ = 0$ ) and decreased near the top wall ( $z^+ = 200$ ). From a vis-a-vis analysis of  $\langle u'_{x,rms} \rangle$  and  $\gamma_{xz}$  we can infer the following: larger strain rates enhance the production of turbulent kinetic energy through the increase of the production term in the corresponding balance equation, whereas smaller strain rates reduce it.

In the thin liquid layer, for decreasing  $\lambda$  we observe an increase of  $|\partial \langle u_x \rangle / \partial z|$ , which is in turn associated to an increase of turbulence fluctuations. By contrast, when crossing the interface into liquid layer 2,  $|\partial \langle u_x \rangle / \partial z|$  decreases for decreasing  $\lambda$ , which corresponds to a decrease of turbulence fluctuations.

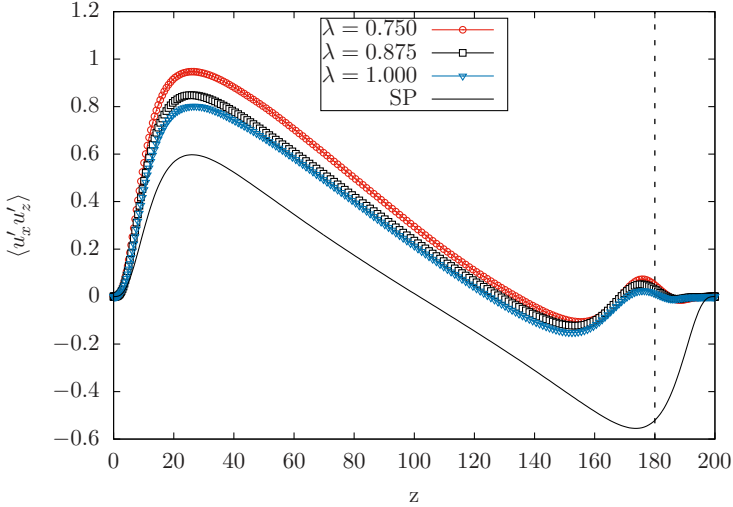


FIGURE 4.9 – Wall-normal behavior of the Reynolds stress,  $\langle u'_x u'_z \rangle$  for the viscosity stratified liquid-liquid flow at  $Re_\tau = 100$ . Lines as in Fig. 4.5.

#### 4.2.7 Reynolds stress

It has been assumed by [37] that Reynolds stress is a diffusive phenomena which is concerning to generalize of molecular transport models. The main target of Reynolds stress analysis in turbulent flow is to explain transport mechanism of fluid motion which linked to vortical structures in the wall and during these transport new generation of vortices maintains the Reynolds stress [9].

In the wall-normal direction, the Reynolds shear stress producing alternative events near the wall, which their intensity can be quantified using the non-dimensional Reynolds stress  $\langle u'_x u'_z \rangle$  will be computed in  $x - z$  plane. All the profiles indicate that average Reynolds stress profile reached to equilibrium shape which balances the mean pressure gradient, which has shown in Fig. 4.9.

#### 4.2.8 Total shear stress without capillary tensor

In our simulation, we have computed  $\langle u'_x u'_z \rangle + \lambda \frac{\partial \langle u_x \rangle}{\partial z}$ . While  $\lambda$  parameter will be applied to thin layer, where viscosity ratio changes across interface, and called viscous shear stress,  $\frac{\partial \langle u_x \rangle}{\partial z}$  is the mean strain rate  $\gamma_{xz}$ . As already shown in Fig. 4.10a), the shape of total shear stress is not what is similar for single phase simulation at  $Re_\tau = 100$  and it comes from the capillary tensor

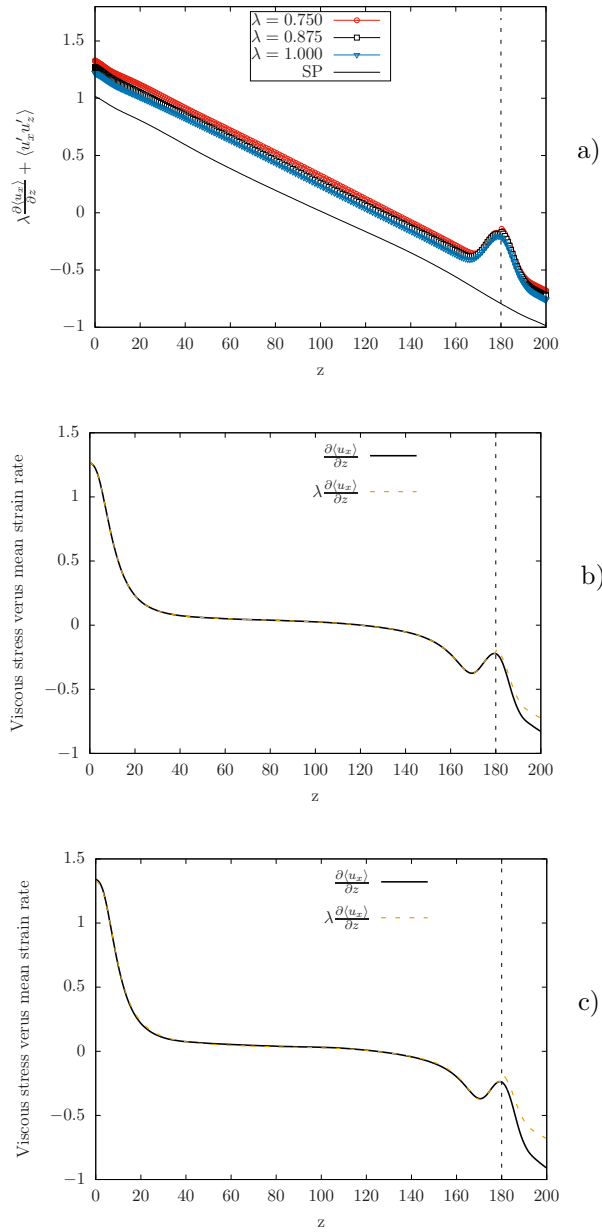


FIGURE 4.10 – a) Wall-normal behaviour of the shear stress (without Korteweg stress),  $\langle u'_x u'_z \rangle + \lambda \frac{\partial \langle u_x \rangle}{\partial z}$  for the viscosity stratified liquid-liquid flow, lines as in Fig. 4.5; b) Wall-normal behaviour of the viscous shear stress (yellow-dashed line),  $\lambda \frac{\partial \langle u_x \rangle}{\partial z}$ , and the mean strain rate (Solid line),  $\frac{\partial \langle u_x \rangle}{\partial z}$ ,  $\lambda = .875$ ; c) Wall-normal behaviour of the viscous shear stress (yellow-dashed line),  $\lambda \frac{\partial \langle u_x \rangle}{\partial z}$ , and the mean strain rate (Solid line),  $\frac{\partial \langle u_x \rangle}{\partial z}$ ,  $\lambda = 0.75$ : at  $Re_\tau = 100$ .

(Korteweg stress);  $\tau_c = (|\nabla\phi|^2 \mathbf{I} - \nabla\phi \otimes \nabla\phi)$ , which we have explained in Sect. 2.3 and this kind of stress tensor has to be added to Navier-Stokes equations to achieve total shear stress. It is clear that, both viscous shear stress and mean strain rate reach their peak value right at two walls. The viscous stress, however attains a lower value due to the decrease of viscosity ratio  $\lambda = 0.75, \lambda = 0.875$  in thin layer (liquid layer 2) in Fig. 4.10b-c), with similar arguments, we can also explain this mechanism is same as what has been mentioned in Sect. 4.2.5.

#### 4.2.9 Spanwise vorticity

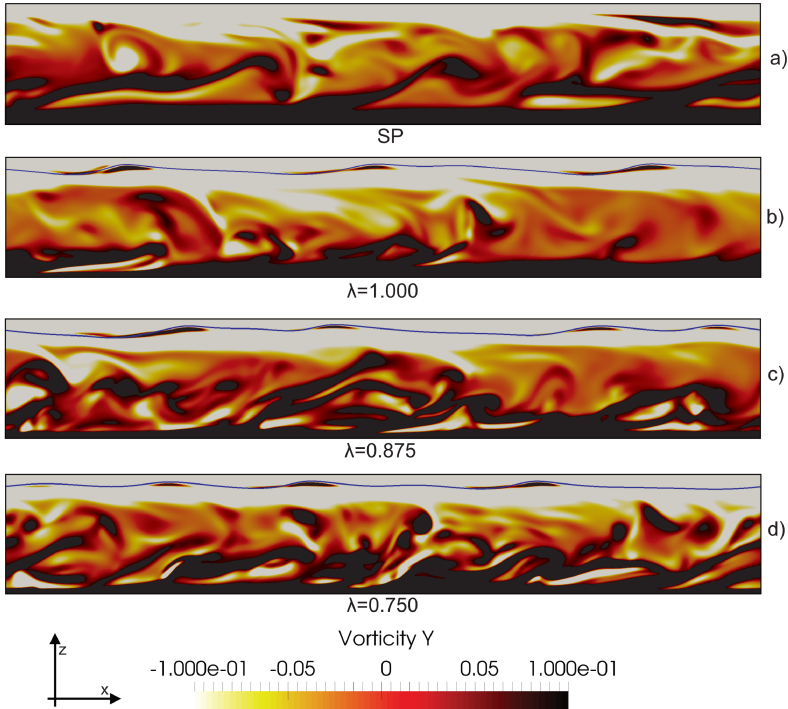


FIGURE 4.11 – Contour maps of the spanwise vorticity  $\langle \omega_y \rangle$  for the viscosity stratified liquid-liquid flow at  $Re_\tau = 100$  and different viscosity ratio  $\lambda$ . Panels: a) Single Phase flow; b) liquid-liquid flow at  $\lambda = 1$ ; c) liquid-liquid flow at  $\lambda = 0.875$ ; d) liquid-liquid flow at  $\lambda = 0.75$ . The location of the interface is explicitly indicated (thin black line) for clarity.

We continue our analysis on turbulence modulation in viscosity stratified liquid-liquid flow by computing the spanwise vorticity  $\omega_y = \partial u_z / \partial x -$

$\partial u_x / \partial z$ , whose behavior is intimately linked to that of  $\gamma_{xz}$  just described. Instantaneous maps of  $\omega_y$  for the different cases considered in this work are shown in Fig. 4.11. For the single phase flow (panel a), the vorticity distribution is almost symmetric and is characterized by long streaky structures emitted from both the bottom and top walls and reaching the core of the channel. In the case of viscosity stratified liquid-liquid layers with equal ( $\lambda = 1$ , Fig. 4.11b) or different viscosity ( $\lambda \neq 1$ , Fig. 4.11c-d), the flow symmetry is lost. In particular, turbulence is promoted far from the interface (near the bottom wall in Fig. 4.11), while it is reduced close to the interface (near the top wall in Fig. 4.11). Interestingly, we note the production of counterrotating rolls induced by the shear at the liquid-liquid interface (black patches attached at the liquid-liquid interface). Their size and strength depends primarily on the surface tension at the interface and on the value of  $\lambda$ , with the intensity of the rolls decreasing with decreasing  $\lambda$  due to the reduced interfacial friction.

### 4.3 Turbulence Near-wall region

Since, in current simulation we have considered two walls and we are in turbulent regime, we should know about transfer mechanism and structures near wall, actually there have been numerous researches [52, 42, 99, 51, 83, 35, 107, 108] to explain coherent streaky structures of the near-wall. In wall bounded turbulence there is a mechanism which the streaky structures goes toward wall direction and they also lifted from wall, which called sweep and ejection and leads to new streamwise vortices that generate new streaky motions this is “bursting“ process, which introduced in [91]. The process called self-sustaining cycle [35] explains turbulence structures of temporally quasi-cyclic process of regeneration. In each cycle streamwise vortices is reinforced into streaks through ejection, then these streaks goes down in the consequence of instability, and again nonlinear interaction of unstable waves generate the streamwise vortices, the cycle has been shown in Fig. 4.12, and main concept is nonlinear solutions of the Navier-Stokes equation which numerically are in agreement with the [43], where turbulent structure near wall amplified even in the quenched situation of outer motions.

Near wall region is filled by smoke areas and border of them has been determined with penetration of non-turbulent fluid, which influenced the outer region, these  $\delta$  scale structures has been called “large-scale motions“ (*LSM*) or turbulent bulges. It has been confirmed that ejection and sweep events have been separated by shear layer [77, 2], ejection will be determined with low movement and negative streamwise fluctuating velocity and

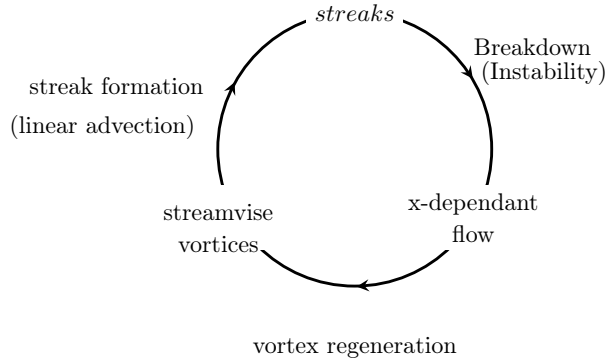


FIGURE 4.12 – Schematic diagram of the self-sustaining cycle [35]

positive vertical fluctuating velocity:  $u'w' < 0$  (second quadrant) , but vice versa Sweep events have higher movement and positive streamwise fluctuating velocity and negative vertical fluctuating velocity:  $u'w' < 0$  (fourth quadrant). Pattern of coherent structure in wall turbulence in a fully developed channel flow exactly distinguish boundaries between clear areas and filled smoky areas before and after bursting as shown in work of [1] with analysing events in quadrant method and finding events in second quadrant, they are starting to generate immediately and their duration is longer than forth quadrant while also moving in group, which are in agreement with that burst are result of stronger group ejections rather than solitary ones [12, 103].

### 4.3.1 Boundary layer separation

About describing the line of separation we know that the actual position of this line of the surface of body will be determined by the properties of the boundary layer, from mathematical point of view we can show the line of separation is a line which points are singular points of the solution of motion equation in boundary layer. With knowledge of the properties of the separation line, there will be a surface which extends into the fluid and marks off the region of turbulent flow. Flow is rotational throughout the turbulent region, but in absence of the separation it would be rotational only in the boundary layer, where the viscosity has important role; the curl of velocity will be zero in main stream and we can say the separation cause

this quantity to penetrate from the boundary layer into the fluid. By considering the conservation of the circulation this kind of penetration can only occur near the surface (in the boundary layer), which called separation of boundary layer and is shown in Fig. 4.13.

Regarding to designing many aerodynamic devices, investigation of separation and reattachment of turbulent flows is important. In spite of the many experimental studies on separated flows, only a limited number of numerical works on separated flows over a flat plate are available, and still the structure of the separated region needs to be understood. An experimental and theoretical study about separating and reattaching two-dimensional turbulent boundary layer on a flat surface has done by [85] and presents interaction between the vortical region and the irrotational free stream outside the separation bubble the interaction between the boundary-layer leads to separation process.

A separated turbulent boundary layer over a flat plate performed a direct numerical simulation confirms that, Reynolds shear stresses and their gradients are large away from the wall and thus the largest pressure fluctuations occur in the middle of the shear layer, while flow de attached from wall [75]. Subject to a strong adverse pressure gradient, another direct numerical simulation has been presented by [98] over the separation bubble concluded that the turbulent kinetic energy increases as the Reynolds shear stress, which this mechanism is coming from a lift-up of turbulent fluid from the wall region that weakens the blocking effect of the wall, which helps to understanding of many of the complex interactions with essential role in any turbulent separated flow.

### 4.3.2 Flow near line of separation

If we consider equation of motion in the boundary layer, the streamline velocity component ( $u_x$ ) is larger compared to normal velocity ( $u_z$ ), by this assumption;  $u_z \ll u_x$  it leads to fluid moves along the surface, and from the wall moves slightly and no septation can occurs. Actually this line of separation As usual,  $x$  is the coordinate along the surface in the stream direction, ad  $z$  is the distance from the surface. If we have a line of separation in  $x - z$  plane, we will consider a point of in this plane with  $x \equiv x_0, z = 0$ .

According to separation we have:

$$u_z(x_0, z) = \infty \quad (4.11)$$

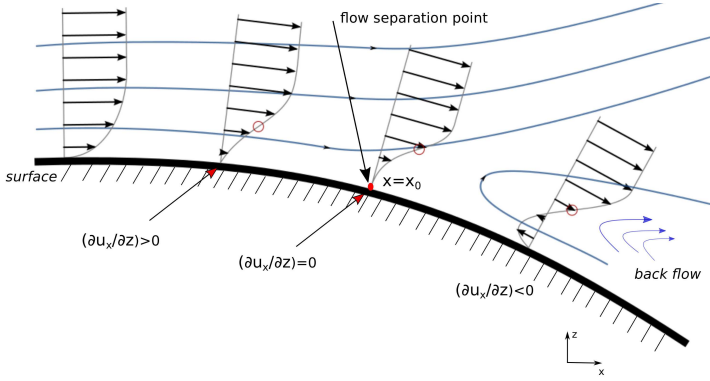


FIGURE 4.13 – Velocity profile in the boundary layer over a covered surface, last profile represents reverse flow which is related to separated flow.

It is obvious from Eq. (4.11) that the derivative  $\partial u_z/\partial z$  goes to infinity at  $x = x_0$ , from continuity we have:

$$\frac{\partial u_x}{\partial x} + \frac{\partial u_z}{\partial z} = 0, \quad (4.12)$$

Which means that  $(\partial u_x/\partial x)_{x=x_0}$  is infinite, or

$$\partial x/\partial u_x = 0 \quad (4.13)$$

Since, near separation point difference between  $u_x - u_0$  and  $x - x_0$  are small, from Eq. (4.13), we can expand as  $x_0 - x = f(z)(u_x - u_0)^2$ , or:

$$u_x = u_0 + \alpha(z)\sqrt{(x_0 - x)} \quad (4.14)$$

From Eq. (4.12) we have:

$$\frac{\partial u_z}{\partial z} = -\frac{\partial u_x}{\partial x} = \frac{\alpha(z)}{2\sqrt{(x_0 - x)}} \quad (4.15)$$

Hence,  $v_z$  will be:

$$v_z = \frac{\beta(z)}{\sqrt{(x_0 - x)}} \quad (4.16)$$

With referring to Navier-Stokes Equation:

$$v_x \frac{\partial u_x}{\partial x} + v_z \frac{\partial u_x}{\partial z} = \nu \frac{\partial^2 u_x}{\partial z^2} - \frac{1}{\rho} \frac{dp}{dx}. \quad (4.17)$$

By looking at Eq. (4.12), the derivative  $\frac{\partial^2 v_x}{\partial z^2}$  doesn't go to infinite in separation point, which same is for  $dp/dx$ , it follows to the both terms in left-hand site of Eq. (4.17) becomes infinite, so we can rewrite:

$$u_x \frac{\partial u_x}{\partial x} + u_z \frac{\partial u_x}{\partial z} = 0 \quad (4.18)$$

With the aid of Eq. (4.12):

$$u_x \frac{\partial u_z}{\partial z} - u_z \frac{\partial u_x}{\partial z} = u_x^2 \frac{\partial}{\partial z} \left( \frac{u_z}{u_x} \right) = 0. \quad (4.19)$$

From Eq. 4.15 and Eq. (4.16) we can define:

$$\frac{u_z}{u_x} = \frac{\beta(z)}{u_0(z) \sqrt{(x_0 - x)}} \quad (4.20)$$

If we want that Eq. (4.20) will a function of  $x$  it should be  $\beta(z) = \frac{1}{2} A u_0(z)$ , where  $A$  is constant value. Finally, we can obtain  $u_x$  and  $u_z$  as a function of  $x$  near separation point:

$$u_z = \frac{A u_0(z)}{2 \sqrt{(x_0 - x)}} \quad (4.21)$$

And,

$$u_x = u_0(z) + A (du_0/dz) \sqrt{(x_0 - x)}. \quad (4.22)$$

From Eq. (4.21) we will find while  $x \rightarrow x_0$  and  $u_z$  becomes infinite. With considering boundary condition at the wall surface we must have  $u_x = u_z = 0$  at  $z = 0$ . By referring to Eq. (4.21) and Eq. (4.23) it reaches to:

$$u_0(0) = 0, \quad (du_0/dz)_{z=0} = 0. \quad (4.23)$$

Here we should mention at the point of separation not only  $u_x = 0$  the derivation  $\partial u_x / \partial z = 0$ , by looking at Eq. (4.21) if  $A$  becomes zero then  $u_z(x_0, z) \neq \infty$  and there fore we don't have any separation point and for  $x > x_0$  we have  $(\partial u_x / \partial z)_{z=0} < 0$ . When fluid moves away from the wall  $u_x$  becomes negative, while the absolute magnitude is increasing. Boundary layer thickness is really thin and fluid beyond the  $x = x_0$  moves in the

opposite direction of the main stream, which called “back-flow“. We should mention it is not necessary condition for separation that  $\partial u_x / \partial z = 0$  which is happening in back-flow.

To see properties of pressure in separation point from Eq. (4.17) we found left-hand side is zero.

$$\nu \left( \frac{\partial^2 u_x}{\partial z^2} \right)_{z=0} = \frac{1}{\rho} \frac{dp}{dx} \quad (4.24)$$

It confirms the sign of  $\frac{dp}{dx}$  is same as  $\left( \frac{\partial^2 u_x}{\partial z^2} \right)_{z=0}$ . We know that  $u_x$  is increasing from the wall and in front of separation. At separation point where  $\frac{\partial u_x}{\partial z} = 0$  we have  $\left( \frac{\partial^2 u_x}{\partial z^2} \right)_{z=0} > 0$ , thus we can conclude:

$$\left( \frac{1}{\rho} \frac{dp}{dx} \right)_{x=x_0} > 0, \quad (4.25)$$

Which means near the separation point fluid moves from lower pressure to the higher pressure and since gradient pressure is related to main stream velocity  $U_x$  therefore:

$$\left( \frac{dU}{dx} \right)_{x=x_0} < 0, \quad (4.26)$$

i.e Velocity of  $U$  decreases in the direction of the flow near the separation point.

### 4.3.3 Waves and shear stress at walls

Waves and streaks observed in our numerical simulations. Fig. 4.14a-c) shows contour distributions of the interface elevation  $\eta^+(x, y, t)$  and the shear stress  $\frac{\partial u_x}{\partial z}$  at top wall and bottom wall, the representative time instances is  $t^+ = 1825$ . The results show that the streaks are observed for interface elevation are similar to what we see for shear stress at top wall, but for bottom wall the shear stress contour distribution is totally different, which means since interface has been located close to top wall the influence of them on shear stress is more highlighted at top wall.

### 4.3.4 Near wall Mechanism

As we discussed in Sect. 4.2.3, for all considered  $\lambda$ , we find a slight increase of the shear stress at the bottom wall, counterbalanced by a corresponding decrease of the shear stress at the top wall [3], such that the overall friction is reduced. This observation supports the idea that the turbulent drag reduction observed here is not only due to the reduced viscosity, but it is indeed due to the presence of a liquid-liquid interface that converts the

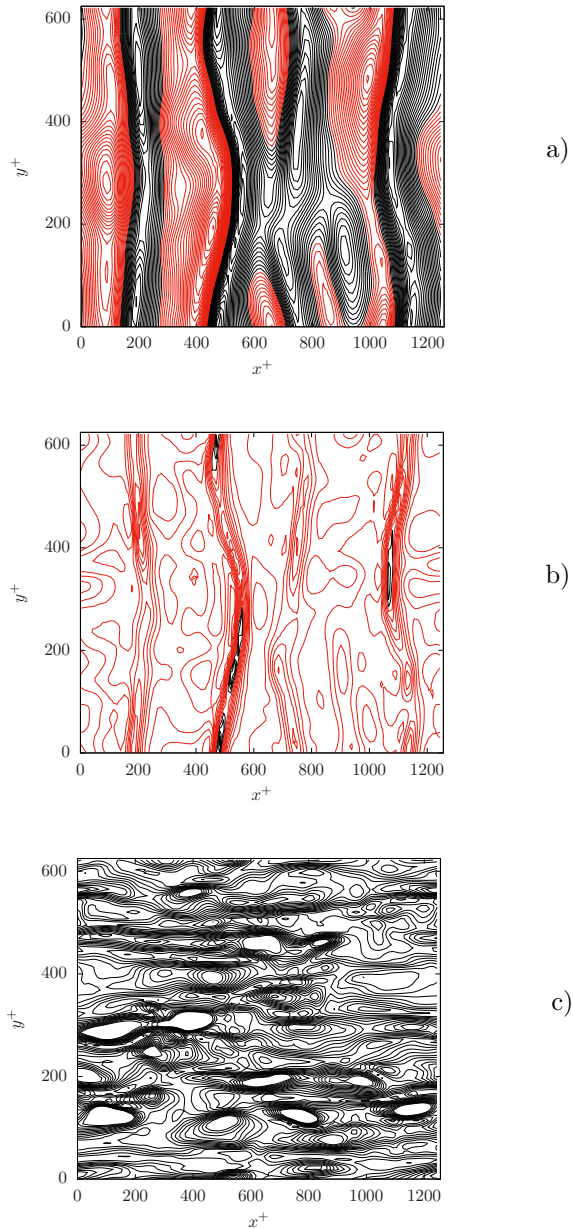


FIGURE 4.14 – Snapshots of the instantaneous liquid-liquid interface for elevation and shear stress at top and bottom wall: a) interface elevation; b) shear stress at top wall; c) shear stress at bottom wall at a given time instant ( $t^+ = 1825$ ), (black line are related to negative and red line are for positive value, respectively).

Turbulent Kinetic Energy (TKE) produced close to the wall into potential energy of interface deformation.

To characterize better the influence of the liquid-liquid interface on the near wall activity, we compute the Probability Density Function (PDF) of the wall shear stress at the top and bottom wall for the different cases. In particular, we consider the normalized deviation of the wall shear stress with respect to the mean value at the corresponding wall, i.e.  $\tau_w' = (\tau_w - \langle \tau_w \rangle) / \langle \tau_w \rangle$ . Results, which are plot in semi-logarithmic scale, are shown in Fig. 4.15. Symbols refer to the two-phase flow simulations at different  $\lambda$ , whereas the solid line indicates the single phase case.

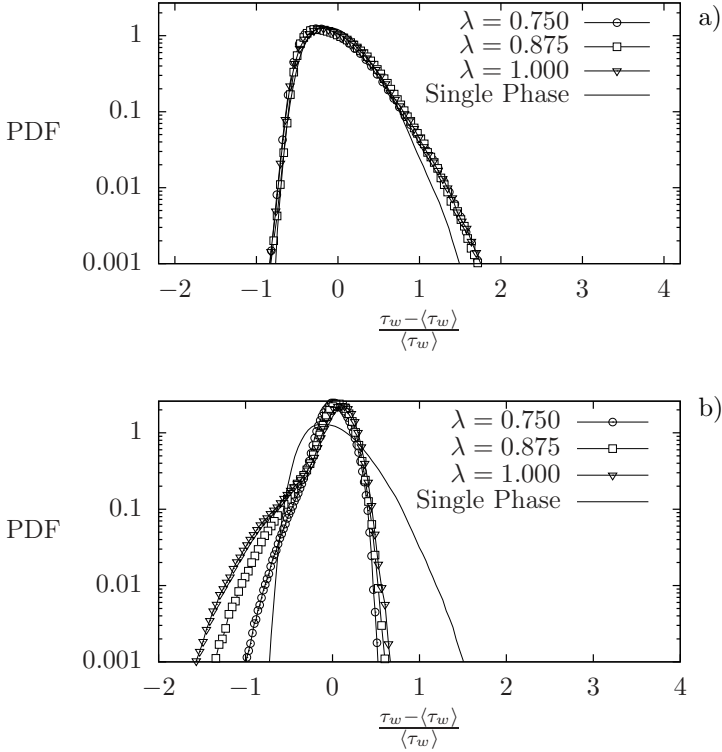


FIGURE 4.15 – Probability Density Function (PDF) of the normalised wall shear stress fluctuation  $\tau_w' = (\tau_w - \langle \tau_w \rangle) / \langle \tau_w \rangle$  for all the simulated cases. Panel a) refers at the bottom wall ( $z^+ = 0$ ) while the panel b) refers at the top wall ( $z^+ = 200$ ). The profile for the two phase cases (resp. single phase case) are shown with symbols (resp. solid line).

At the top wall, the situation changes remarkably. As expected, only for the single-phase case is the PDF( $\tau'_w$ ) identical to that observed at the bottom wall (there is no statistical difference between the two walls for the single phase case). For all the other cases, the PDF shape is completely different. In particular, we notice that for decreasing  $\lambda$  (symbols) PDF ( $\tau'_w$ ) become taller and narrows around the most probable value  $\tau'_w = 0$ . This indicates that the wall shear stress fluctuations are largely reduced by the presence of the liquid-liquid interface, which indeed weakens the turbulent generation cycle and reduces the wall shear stress fluctuations. We interestingly notice that, while for the single phase case the PDF( $\tau'_w$ ) is positively skewed, for the multiphase cases it is negatively skewed. Yet, we observe the existence of an explosive separation among the PDF profiles of the multiphase cases (symbols) for  $\tau'_w \leq -0.3$ . In particular, the probability of observing large negative values of  $\tau'_w$  ( $\tau'_w < -1$ ) increases for increasing  $\lambda$ . This is extremely important, because the appearance of  $\tau'_w < -1$  events indicates the presence of regions characterized by a local value of the shear stress  $\tau_w$  that changes sign compared to the mean value measured at that wall. Such shear inversions are a clear footprint of local flow recirculation patterns. Note that the onset and persistency of recirculation patterns is specifically linked to the presence of a liquid-liquid interface (characterized by a finite value of the surface tension) that interacts with the near wall turbulence modifying its dynamics. By contrast, these recirculation patterns depend only slightly on the value of the liquid viscosity, with a larger effect observed for  $\lambda = 1$  (i.e. recirculation patterns have a reduced strength when the viscosity of the thin layer is reduced, i.e. when  $\lambda < 1$ ). This observation is consistent with the possibility of turbulence reactivation mechanisms due to the reduced viscosity of the thin liquid layer (layer 1).

To understand the reason why we observe such a peculiar structure of the wall shear stress at the top wall, we now focus on the behavior of the interface dynamics. Our intuition is that the deformation of the liquid-liquid interface can induce a large turbulence modulation characterized also by the appearance of regions of local flow recirculation. To this aim, we calculate the PDF of the liquid-liquid interface elevation  $\eta^+$ , expressed in wall units and computed as the difference between the actual position of the deformed interface and the initial position. Results are shown in Fig.4.16.

Positive values of  $\eta^+$  indicate an interface crest, whereas negative values of  $\eta^+$  indicate an interface throat. We observe that the PDF( $\eta^+$ ) has a characteristic shape, regardless of the value of  $\lambda$ . The most probable values of the interface elevation range between  $-5 < \eta^+ < 5$ , with maximum at

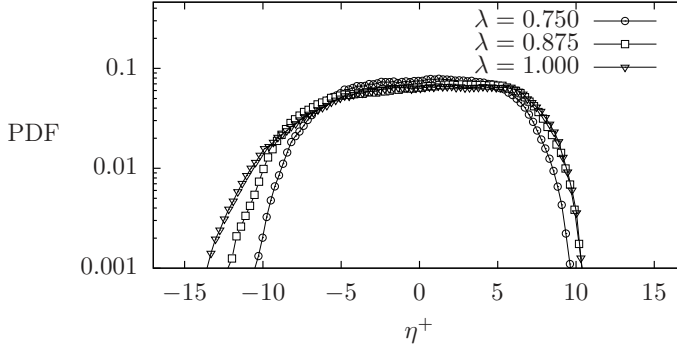


FIGURE 4.16 – Probability Density Function (PDF) of the interface elevation  $\eta^+$  for all the simulated cases (different values of  $\lambda$ ).

$\eta^+ \simeq 10$  and minimum at  $\eta^+ \simeq -15$ . This means that the interface deforms but it does not reach the wall (for which it should be  $\eta^+ \simeq 20$ ) and it does not break. We interestingly note that decreasing  $\lambda$  increases the probability of having  $-5 < \eta^+ < +5$  while reducing the probability of having large positive ( $\eta^+ > 5$ ) and negative ( $\eta^+ < -5$ ) events. This reflects the observation that for  $\lambda = 1$  the interface is smoother, yet characterized by higher crests and deeper throats. For this reason, and without loss of generality, in the following we will focus on the case  $\lambda = 1$ , because the modulation of wall turbulence (induced by the liquid-liquid interface dynamics) we wish to discuss is emphasized at this value of  $\lambda$ .

### 4.3.5 Instantaneous profiles and distributions

In Fig. 4.17 we focus on the instantaneous distribution of the shear stress at the top wall ( $z^+ = 200$ ).

We remark that the mean shear is negative at this wall, i.e.  $\langle \tau_w \rangle < 0$ . Yellow regions indicate regions of negative  $\tau_w$  (i.e. aligned with the mean shear) whereas red regions indicate regions of positive  $\tau_w$  (i.e. at odds with the mean shear). The presence of regions in which  $\tau_w$  changes sign compared to its mean value indicates the presence of a separation point in the boundary layer and a corresponding flow recirculation region. One of such recirculation regions is shown more closely in Fig. 4.17b) and corresponds to the square highlighted in Fig. 4.17a) and labelled A-A. As mentioned

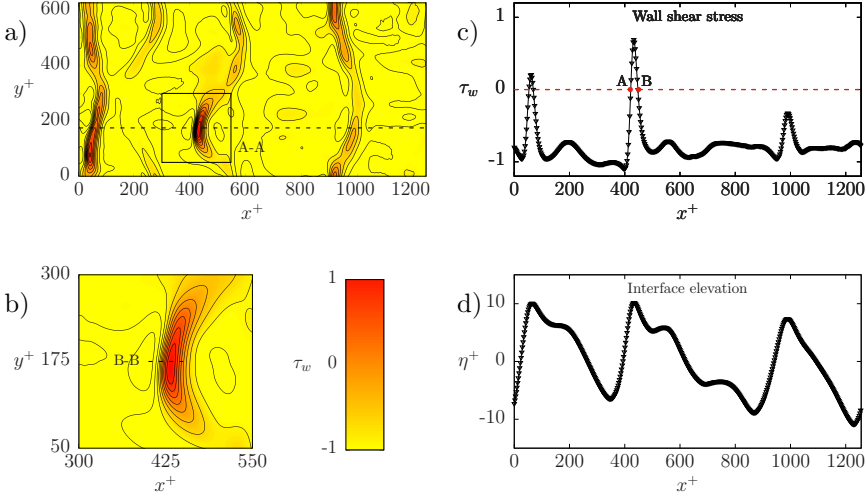


FIGURE 4.17 – Panel a): Instantaneous wall shear stress distribution  $\tau_w$  at the top wall ( $z^+ = 200$ ) computed at  $t^+ = 3650$  for the simulation with  $\lambda = 1$ . Red regions identify positive areas of shear stress, i.e. opposite to the direction of the mean stress at that wall ( $\langle \tau_w \rangle < 0$ ). Panel b): detailed inspection of the shear stress distribution in the square region A-A identified in panel a). Panels c-d): Streamwise distribution of the shear stress (panel c) and of the interface elevation (panel d) computed at  $y^+ = 175$ .

above, recirculation regions associated to the boundary layer separation are intimately linked to the dynamics of the underlying liquid-liquid interface. To draw this link, in Fig. 4.17c-d) we present a vis-a-vis comparison between  $\tau_w$  and  $\eta^+$  measured along the dashed line shown in Fig. 4.17a) (and located at  $y^+ = 175$ ). Fig. 4.17c) refers to the behavior of  $\tau_w$ , whereas Fig. 4.17d) refers to the behavior of  $\eta^+$ . In Fig. 4.17c) the threshold  $\tau_w = 0$  is explicitly shown using a red dashed line. The correlation between  $\tau_w$  and  $\eta^+$  is apparent. When  $\eta^+$  develops a peak, the corresponding value of  $\tau_w$  trespasses the threshold line  $\tau_w = 0$  and favors the appearance of a recirculation region. This happens twice at the selected time and  $y^+$  position, namely at  $x^+ \simeq 50$  and  $x^+ \simeq 420$ . A further extreme event for  $\eta^+$  occurs at  $x^+ \simeq 1000$ , but in this case the interface elevation is not sufficiently large to induce the boundary layer separation.

To understand more closely the reason why the boundary layer separates when the liquid-liquid interface develops a peak, we consider more closely the dynamics inside the region labelled A-A in Fig. 4.17a). Results, which are shown in Fig. 4.19 refer to a  $x^+ - z^+$  plane taken at a spanwise location  $y^+ = 175$  and ranging between  $400 < x^+ < 450$  and  $170 < z^+ < 200$ . In this picture, the recirculation region is explicitly visualized through the use

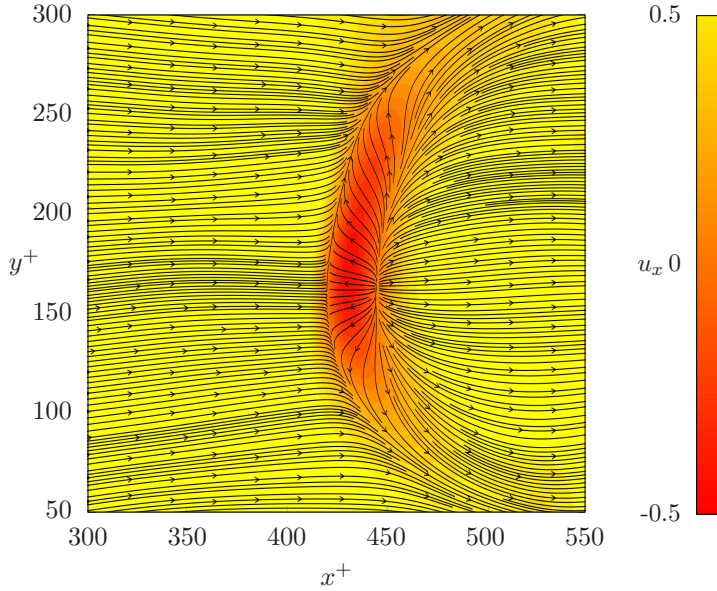


FIGURE 4.18 – Instantaneous flow streamlines corresponding to the region labelled A-A in Fig. 4.17a). The  $x^+ - y^+$  plane is located close to the top wall, at  $z^+ = 199.5$ . Contour maps of the streamwise velocity are also shown: red regions correspond to regions of negative streamwise velocity (flow recirculation) whereas yellow regions correspond to regions of positive streamwise velocity.

of instantaneous flow streamlines.

To understand more closely the reason why the boundary layer separates when the liquid-liquid interface develops a peak, we consider more closely the dynamics inside the region labelled A-A in Fig. 4.17a). Results, which are shown in Fig. 4.19 refer to a  $x^+ - z^+$  plane taken at a spanwise location  $y^+ = 175$  and ranging between  $400 < x^+ < 450$  and  $170 < z^+ < 200$ . In this picture, the recirculation region is explicitly visualized through the use of instantaneous flow streamlines. Points A and B correspond to those highlighted in Fig. 4.17c). Together with the flow streamlines, we also plot the value of the streamwise velocity (background color map) and of the interface elevation (solid thick black line). By looking at this picture we notice that the maximum interface elevation occurs at  $x^+ \simeq 425$ , whereas the recirculation region ranges between  $420 < x^+ < 445$  and has a thickness of roughly 5 wall units in the wall-normal direction. To further investigate on the structure of the recirculation region, we propose a top view of the flow streamlines on the square region labelled A-A in Fig. 4.17a). The new visualization, proposed in Fig. 4.18, shows the instantaneous flow streamline on a  $x - y$  plane between  $300 < x^+ < 550$  and  $50 < y^+ < 300$  and taken at  $z^+ = 199.5$  (i.e. very close to the top wall). Together with the flow

streamlines, we also plot a counter map of the streamline velocity (red regions indicates recirculation). We observe that the recirculation region has a crescent-shaped structure delimited by two curved stagnation lines (which include points A and B when  $y^+ = 175$ , which have explained the mechanism in Sect. 4.3.1).

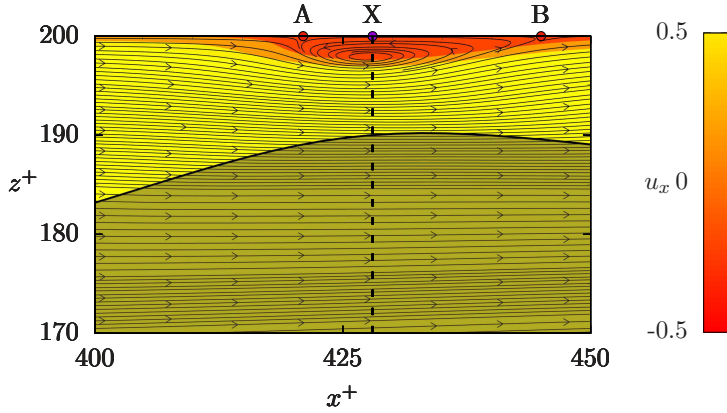


FIGURE 4.19 – Instantaneous flow streamlines corresponding to the region labelled B-B in Fig. 4.17. The  $x^+ - z^+$  plane is located at  $y^+ = 175$ . Contour maps of the streamwise velocity are also shown: red regions correspond to regions of negative streamwise velocity (flow recirculation) whereas yellow regions correspond to regions of positive streamwise velocity. Note that the position of the interface is explicitly indicated by the solid black line.

To explain such a peculiar structure, we computed the contour map of the two dimensional divergence

$$\nabla_{2D} = \frac{\partial u_x^+}{\partial x^+} + \frac{\partial u_y^+}{\partial y^+} = -\frac{\partial u_z^+}{\partial z^+}. \quad (4.27)$$

close to the top wall, at  $z^+ = 199.5$ . Results are shown in Fig. 4.20. Upwards motions of fluids impinging on the wall (i.e. velocity sources usually called upwellings) are characterized by positive values of  $\nabla_{2D}$ , whereas downwards motions of fluid leaving the wall (i.e. velocity sinks usually called downwellings) are characterized by negative values of  $\nabla_{2D}$ . Results clearly indicate that there is a strong upwelling region ( $420 < x^+ < 440$ ) that slightly precedes a strong downwelling region ( $440 < x^+ < 460$ ). Based on our results, we envision the following mechanism. When the interface devel-

ops a peak, (for instance at  $x^+ = 425$ , see Fig. 4.20) a lump of fluid in the thin liquid layer is pushed towards the top wall. Since it has a small (but not negligible) streamwise velocity, it impact the wall producing a stagnation point at  $x^+ \simeq 445$ . Upon impaction with the top wall, the lump of fluid is split into two branches: one branch moves downstream (towards larger  $x^+$ ) while one branch moves upstream (towards smaller  $x^+$ ) and produces a recirculation region. However, due to the small inertia of this second branch, the recirculation region extends up to  $x^+ = 420$  and cannot move further upstream. When the incoming stream reaches the recirculation region, it is forced to move sideways (blockage effect of the recirculation region) generating the peculiar crescent shape.

We look at two instantaneous profiles of the streamwise velocity. In

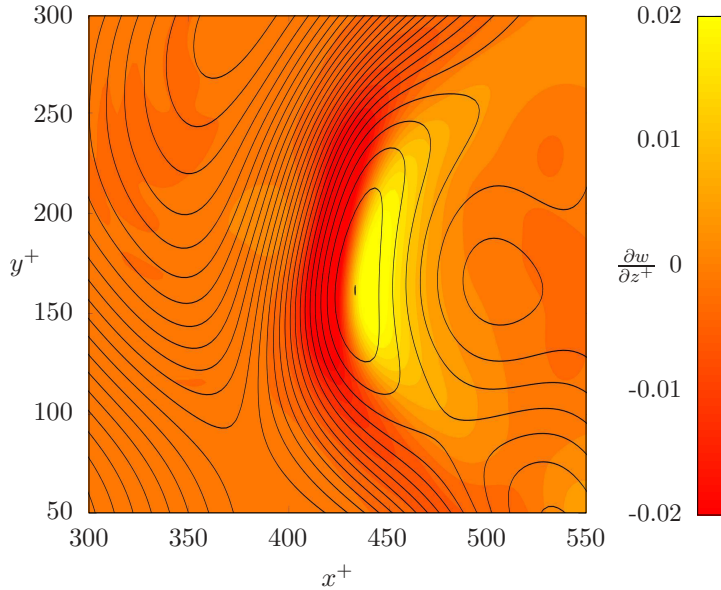


FIGURE 4.20 – Contour plot of the two dimensional flow divergence,  $\nabla_{2D} = -\frac{\partial u_x^+}{\partial z^+}$  for the square area labelled A-A indicated in Fig. 4.17. The horizontal slice is located at  $z^+ = 199.5$ . Red regions identify upwellings while yellow regions identify downwellings. Contour lines (solid black lines) of the interface elevation  $\eta^+$  are also shown for comparison.

Fig. 4.21 two velocity profiles extracted at  $t^+ = 3650$  are shown. The red profile refers to the position  $x^+ = 630$ ,  $y^+ = 175$ , in this position  $\eta^+ \simeq 0$  (Fig. 4.17 and  $\tau_w$  and  $\langle \tau_w \rangle$  at the top wall ( $z^+ = 200$ ) have the same sign. By opposite the black line identify the velocity profile along the dashed line of Fig. 4.19, the line start from the point X of the same figure and which is located at  $x^+ = 430$  w.u. and  $y^+ = 175$  w.u., between the two stagnation points. Comparing the two profile we can observe that for the red profile

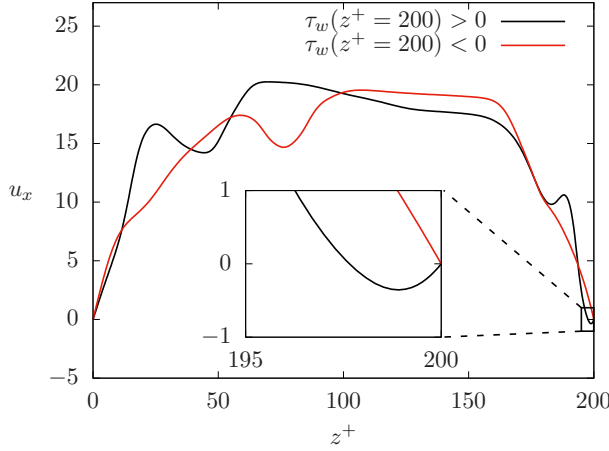


FIGURE 4.21 – Instantaneous profiles of the streamwise velocity along the  $z^+$  direction. The red line show an instantaneous streamwise velocity profile at  $x^+ = 630$  and  $y^+ = 175$  along the  $z^+$  direction, wall shear stress at the top wall ( $z^+ = 200$ ) are negative and  $u_x > 0$  across all the channel. By opposite black line show the instantaneous velocity profile at  $x^+ = 430$  and  $y^+ = 175$ , wall shear stress at the top wall are positive, a recirculation phenomena is present and in a small portion of the  $z^+$  axis  $u_x < 0$ .

the wall shear stress at  $z^+ = 200$  are positive whereas for the profile which pass through the recirculation zone the wall shear stress at the top wall are positive. Furthermore we can observe that the recirculation involve only a small portion of the  $z^+$  axis, approximately  $\simeq 2 - 3 w.u.$

### 4.3.6 Correlation between the interface deformation and the shear stress

To quantify more closely the correlation between the interface deformation and the shear stress inversions at the wall (recirculation), we finally present a joint probability density function between the normalized interface deformation  $\eta^+/\eta_{max}^+$  and the corresponding shear stress deviation  $\tau_w' = (\tau_w - \langle \tau_w \rangle)/\langle \tau_w \rangle$ . Results, which are shown in Fig. 4.22, refers to the top wall (panel a) and to the bottom wall (panel b). The most interesting situation is observed at the top wall (Fig. 4.22a). For negative values of  $\eta^+/\eta_{max}^+$  (i.e. for interface throats), the interface deformation and the wall shear stress are essentially uncorrelated. The effect of the interface is in this case limited to an effective shear stress modulation that narrows the

distribution shear stress distribution around  $\tau'_w = 0$ . The situation changes remarkably when we consider positive values of  $\eta^+/\eta_{max}^+$  (i.e. for interface crests). In this case, we observe a strong correlation between  $\eta^+/\eta_{max}^+$  and  $\tau'_w$ . In particular, when  $\eta^+/\eta_{max}^+$  increases, then  $\tau'_w$  becomes progressively larger in magnitude (but with negative sign). In particular, when  $\eta^+/\eta_{max}^+ \rightarrow 1$ ,  $\tau'_w < -1$ . These events represent exactly the generation of shear stress inversions with the appearance of flow recirculation regions. This plot undoubtedly demonstrate the strong correlation between the presence of wave crests and the flow recirculation close to the wall. By contrast, at the bottom wall (far from the interface, Fig. 4.22b) the correlation between  $\eta^+/\eta_{max}^+$  and  $\tau'_w$  is completely different. Specifically, we observe that the joint PDF has in this case a broader area, typical of uncorrelated variables ( $\tau'_w$  changes almost independently of  $\eta^+/\eta_{max}^+$ ). Yet, no shear stress inversions (i.e. no  $\tau'_w < -1$ ) are observed.

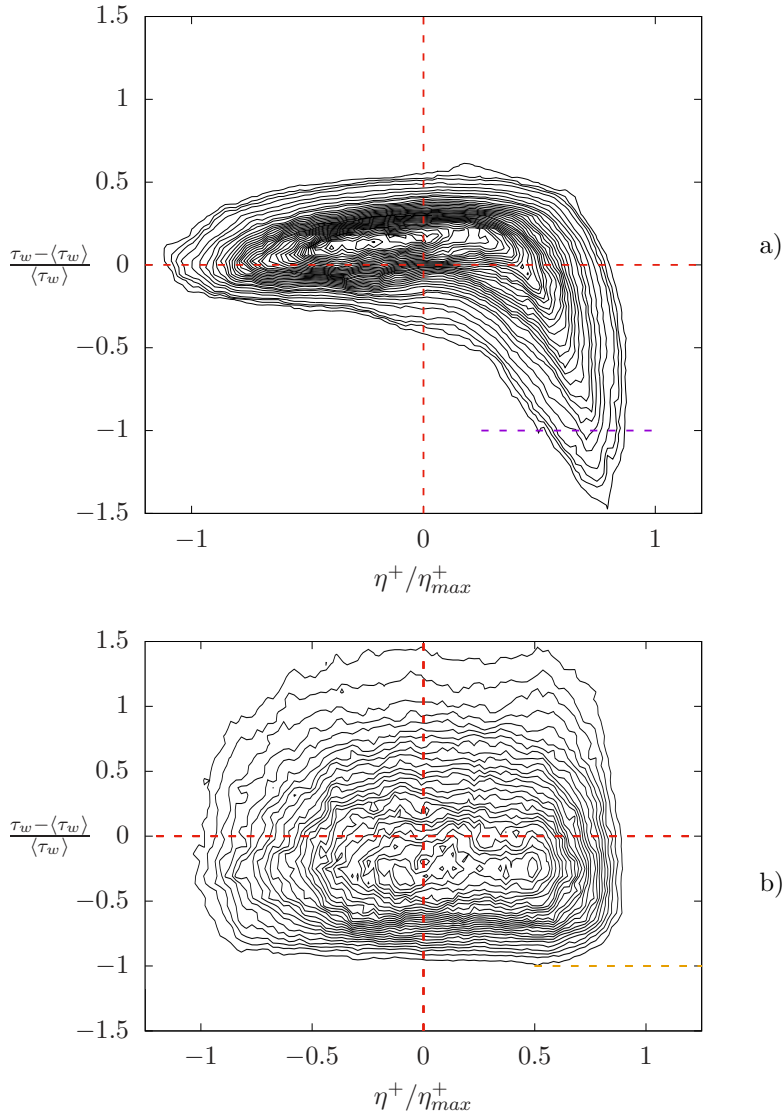


FIGURE 4.22 – Joint Probability Density Function (PDF) between the normalized interface deformation  $\eta^+ / \eta_{max}^+$  and the corresponding shear stress deviation  $\tau_w' = (\tau_w - \langle \tau_w \rangle) / \langle \tau_w \rangle$ . Panel a) refers to the top wall ( $z^+ = 200$ , i.e. close to the interface). Panel b) refers to the bottom wall ( $z^+ = 0$ , i.e. far from the interface).

## 4.4 Wave turbulence

The object of this section is to show the wavenumber spectra and discuss their features in the context of Weak Turbulence Theory (WTT), a statistical theory describing weakly interacting random waves.

Focusing on the specific case of capillary waves, WTT is based on the inviscid and irrotational equations of motion (Laplace equation with suitable boundary conditions on the free surface), which, under the hypothesis of homogeneity and weak nonlinearity, leads to an evolution equation for the wave spectrum. This equation is known as the kinetic equation. In the presence of forcing and dissipation, the kinetic equation has isotropic solutions, known as Kolmogorov–Zakharov solutions [117], due to the similarity with Kolmogorov solution in fluid turbulence.

Although WTT is developed under a number of restrictions (weak nonlinearity, homogeneity, isotropy and separation of scales between forcing and dissipation), it has already been observed in [8] that some theoretical predictions can hold even if such hypotheses are not fully met. Further confirmations of WTT have also been obtained in a number of experimental works [109, 53, 30, 36, 27, 70].

In a recent Numerical study [122], it has been also shown that WTT can be recovered even if waves are forced by turbulence over a broad range of length scales, hence preventing from a clear definition of a scale separation between forcing and dissipative scales. These results can be important in possibly clarifying the issue related to the role of viscous dissipation in the capillary wave range.

In the capillary regime, the theory predicts a direct cascade of energy  $E(k) \sim k^{-15/4}$ , with  $k = \sqrt{k_x^2 + k_y^2}$ . In the following, we will try to compare the theoretical predictions given by WTT with the results of our simulations in the statistically stationary regime.

### 4.4.1 Dimensional derivation of capillary wave

Capillary waves has been the subject of many investigations, for better understand of these mechanism in following: we will show relation between frequency and wave number with a prototype of [76].

First of all we find the physical dimension of the energy spectrum for general d-dimensional wave systems. Let us suppose that that the d-dimensional energy density,  $E$ , is finite in physical space. Here is a short cut way of finding the energy spectrum dimension. For an incompressible fluid, simply

we can use  $\rho = 1$ , which means that we have chosen the system of units where  $m$  and  $V$  have the same physical dimension and the dimension of mass can be  $l^3$ , if we deal in isotropic system related spectral energy density:  $E_k = \omega_k \eta_k$  only depends on the wave number ( $k$ ), for physical dimension of the energy in such system we can write:

$$[E] = \left[\frac{1}{2}mv^2\right] = \frac{[l]^5}{[t]^2} \quad (4.28)$$

For energy density (energy per unit volume or area or length) it will be:

$$\frac{[E]}{[l^d]} = \left[\int E_k^{(1D)} dk\right] = E_k^{(1D)} [l^{-1}] \quad (4.29)$$

By substituting in Eq. (4.28) we reach to:

$$[E_k^{(1D)}] = \frac{[l]^{6-d}}{t^2} \quad (4.30)$$

If we want to know about energy flux dimension, by considering energy balance equation it will be:

$$\dot{E}^{1D} + \partial_k \epsilon = 0 \quad (4.31)$$

Where  $\epsilon$  is energy dissipation rate and its dimension is:

$$[\epsilon] = \frac{[l]^{5-d}}{t^3} \quad (4.32)$$

In the case of considering a physical wave system characterized by a single dimensional parameter, which is valid for all related systems, we can define  $\lambda_k$  from dispersion relation, where its dimension depends on  $\alpha$ :

$$[\omega_k] = \lambda_k^\alpha \quad (4.33)$$

Dimension of  $\lambda_k$  arrives to:

$$[\lambda_k] = [\omega][k]^{-\alpha} = [t]^{-1}[l]^\alpha \quad (4.34)$$

From above relation, the original physical constant like: surface tension will then be uniquely determined in terms of  $k$ . In a system by  $N$  wave processes from Eq. (4.31) we have:

$$\epsilon \sim \dot{E} \sim E^{N-1} \quad (4.35)$$

Relation of Eq. (4.35) and expressions Eq. (3.6) and Eq. (4.34) make the scaling for the energy spectrum as:

$$E_k \sim \lambda_k^x \epsilon^{\frac{1}{N-1}} k^y \quad (4.36)$$

Keeping in mind that dimension of  $\epsilon$  goes to:  $[\epsilon] = [\frac{u^2}{t}] = \frac{l^2}{t^3}$  and By Eq. (4.28) and Eq. (4.34) we will obtain:

$$x = \frac{2N-5}{N-1} \quad y = (d-6+2\alpha) + \frac{5-d-3\alpha}{N-1} \quad (4.37)$$

For capillary wave, wave system is dealing with  $N = 3, d = 2$  and  $\omega = \sigma^{\frac{1}{2}} k^{\frac{3}{2}}$ ,  $\sigma$  is surface tension and thus  $\alpha = \frac{3}{2}$ , which is in agreement with what we have mentioned in Sect. 4.1.1, Eq. (4.36) and leads to find the Zakharov-Filonenko spectrum [116].

## 4.5 Wave growth

The dynamics of the deformable interface is coming from the interaction between external forcing (pressure/velocity fluctuations and large-scale coherent structures) and restoring forces (surface tension). For more discussion about wave growth in our numerical method, we have calculated root-mean-square (r.m.s.) of the interface amplitude in time,  $\eta_{rms} = \langle \eta(t) \rangle^{1/2}$ , by selecting one case study:  $\lambda = 1.0$ , with reference to Fig. 4.23, the interface dynamics is changing by time and wave growth has a linear expression in the principal stage of development and this result confirms growth rate of  $\eta_{rms}(t)$  is independent of the physical parameters in the simulations and capillary effects are always dominate, which has been discussed by [122], as we see in Fig. 4.23 after passing transient  $\eta_{rms}$  reaches to an asymptotic value, indicating a saturation for the growth of the interface amplitude.

### 4.5.1 WTT of capillary waves

With considering WTT, infinite domain and dissipation at only high wavenumbers for capillary waves underlying [89, 100] shows the isotropic spectrum of surface elevation reaches to a closed-form stationary solution and energy supply at larger scales will be balanced by energy dissipation at smaller scales:

If we consider isotropic solutions for capillary regime like as [117], direct cascade of energy should follow:

$$E_k \sim k^{-\frac{15}{4}} \quad (4.38)$$

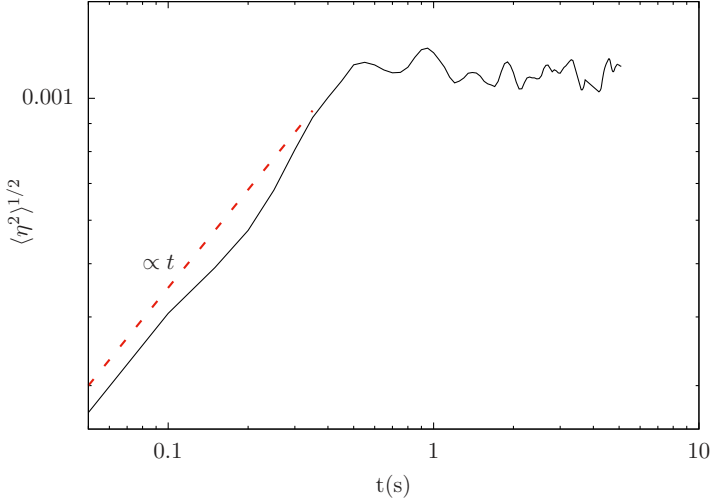


FIGURE 4.23 – Time evolution of the  $\eta_{rms} = \langle \eta(t) \rangle^{1/2}$  for the simulation  $\lambda = 1.0$  (black line), initial stage wave growth as a linear function of  $t$  (dashed line).

Here, we use  $k$  to represent vector wavenumber, where  $k = k_x^2 + k_y^2$ . The validity of Eq. 4.38 have investigated numerically in consistent with the theoretical value [88, 89, 30, 26], but in some experiments deviations are reported such as [109, 15].

Kinetic equation (KE) is a way to check weak-turbulence theory [88], which can be determined by direct numerical solution of the nonlinear equation and wave interaction, which later confirmed by experiments [104], while some results only related to isotropic [115] and some other are presenting for anisotropic [104]. Still, there is long way to better understand of the problem regarding the discrete capillary wave turbulence in the framework of the KE, and is not directly applicable. In following, we are going to examine our direct numerical simulation for checking weak turbulence theory.

### 4.5.2 Spatial spectrum

The first application of the numerical simulation is to investigate isotropic turbulence of capillary waves, and evaluate the validity of WTT. We analyzed the turbulent regime by using Fourier analysis, for capillary waves the wavelength is very short and surface tension acts on the surface boundary condition, we compute the two dimensional Fourier transform in a time of  $\eta(k_x, k_y)$  to obtain the  $E(k_x, k_y, t) = \int \eta(k_x, k_y, t) e^{-i2\pi(k_x + k_y)} dk_x dk_y$  for

three simulations:  $\lambda = 1.0$ ,  $\lambda = 0.875$  and  $\lambda = 0.75$  at one time snapshot  $t^+ = 1850$ , where is in fully developed turbulent zone, selected results in Fig. 4.24 exhibits wave energy is distributed at certain selected wave components, which confirms angular properties of spectrum is relevant to strong anisotropy [121, 66]. The spread of the energy around the dissipation is much wider means stronger nonlinearities [5] and this nonlinearity is due to larger amplitude. Wider spread of energy shown in Fig. 4.24b) and Fig. 4.24c) compare to Fig.4.24a), as expected a high energy wave is characterized by a high amplitude; a low energy wave is characterized by a low amplitude, which smaller amplitude of waves can be observed in  $\lambda = 0.75$ .

We are looking for consistency with theoretical predictions in weak turbulence theory, so by computing time-averaged wavenumber spectrum  $E(k_x) = \frac{1}{\Delta t} \int_t \eta(k_x, k_y, t) \int_{k_y} dk_y dt$  of interface structure over a period  $\Delta t = 15(s)$ , coming spectrum results as a function of the wavenumber in the streamwise direction  $k_x$  in Fig. 4.25 shows: the range scale is in following of  $k_x^{-\frac{19}{4}}$ , which is in the good agreement between DNS and wave turbulence theory [88], these spectra are in range scale as  $k_x^{-\frac{19}{4}}$  instead of  $k_x^{-\frac{15}{4}}$  due to averaging over  $y$  direction [121], we clearly observe results are almost similar in three cases of simulations, which is related to small difference in viscous ratio, and also it is clear that energy is transferred from large scale (injection) to small scale (viscous dissipation), if we look at Fig. 4.25a-c) our results are similar to what expected from [25], where for small viscosity (i.e., low dissipation) power-law exponent will be what was expected from theory.

In this Section, by presented results from direct numerical simulations of capillary wave turbulence. Under the WTT assumptions, the unsteady solution of the KE leads to a time-varying spectral amplitude proportional to time and we were able to confirm the WTT with  $k^{-19/4}$  scaling. These results also confirms, even waves are in anisotropy situation, it does not play a significant role in the estimation of the spatial spectrum exponent [36], which is in contrary with [86]. We also should consider damping assumption regarding considering viscosity in three cases of simulations, but in our numerical simulation viscosity is small and viscous stress has a small influence on damping [60, 64, 41].

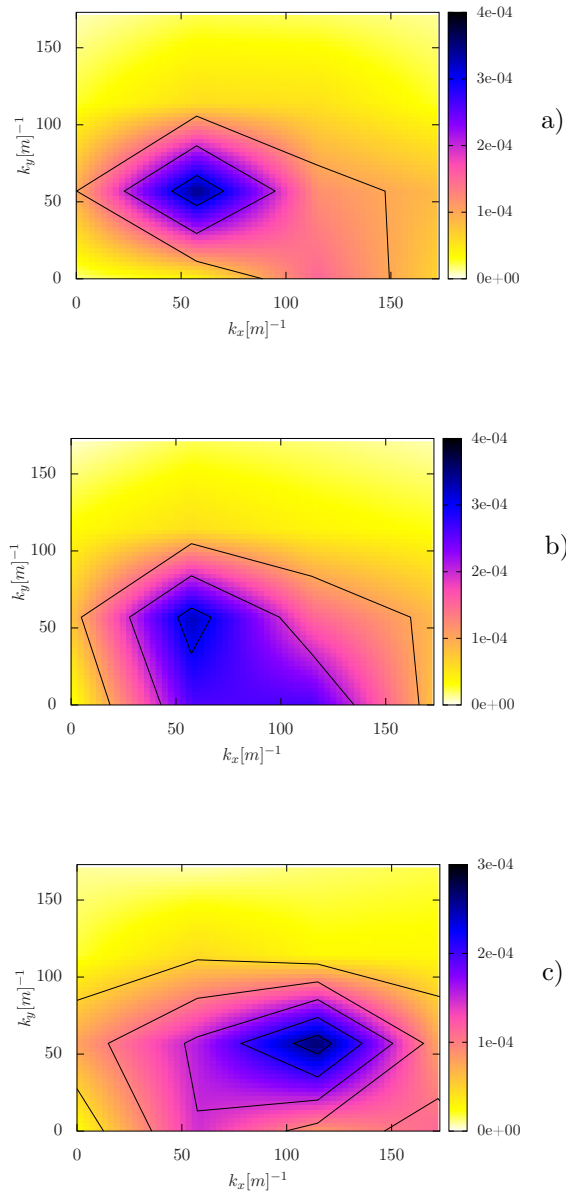


FIGURE 4.24 – Two dimensional wavenumber spectrum  $E(k_x, k_y, t)$  for one time snapshot: at time  $t^+ = 1850$  for three simulations, a)  $\lambda = 0.75$  ; b)  $\lambda = 0.875$  ; c)  $\lambda = 1.0$ , which illustrates the anisotropy in the  $(k_x, k_y)$  space.

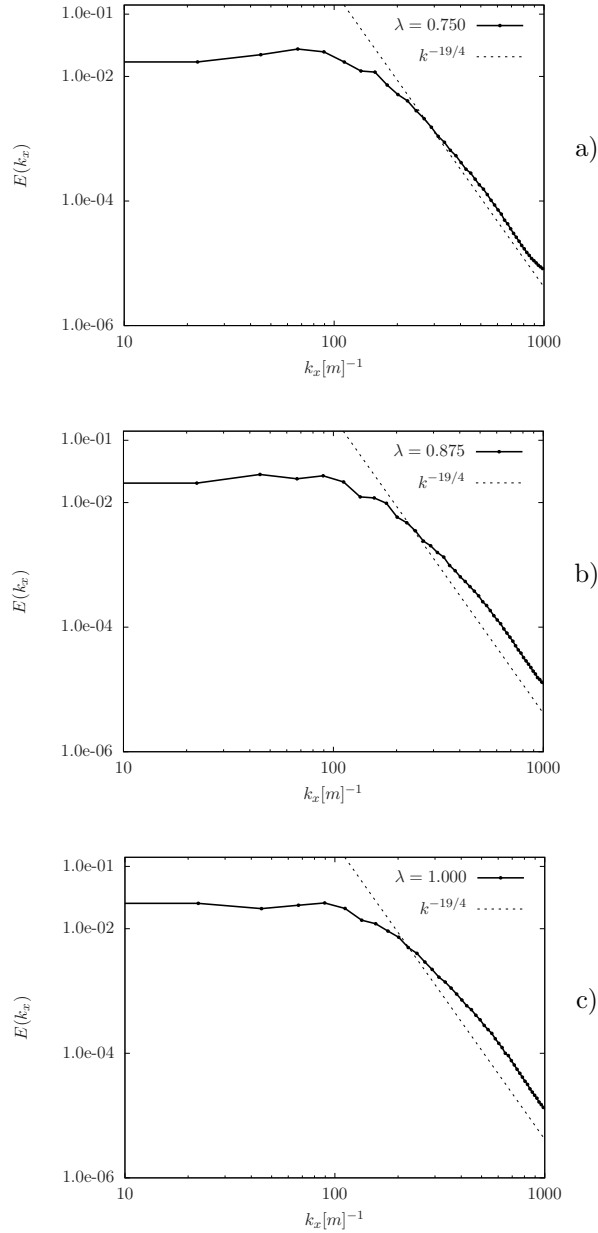


FIGURE 4.25 – Time-averaged wavenumber spectrum  $E(k_x) = \frac{1}{\Delta t} \int_t \eta(k_x, k_y, t) \int_{k_y} dk_y dt$  of interface structure over a period  $\Delta t = 15(s)$  for three simulations: a)  $\lambda = 0.75$  ; b)  $\lambda = 0.875$  ; c)  $\lambda = 1.0$ , in steady state situation. Dashed lines have slopes  $-19/4$ .

## 4.6 Conclusions

In this chapter Direct Numerical Simulation (DNS) has been used to study the turbulent Poiseuille flow. A thin low viscosity layer flows on the top of a thick fluid layer. The two liquids are separated by a deformable interface and flow in a rectangular channel. The layers have matched density,  $\rho_1 = \rho_2$ , but different viscosity  $\nu_1 \neq \nu_2$ . Three different values of the viscosity ratio has been considered:  $\lambda = \nu_1/\nu_2$ :  $\lambda = 1$ ,  $\lambda = 0.875$  and  $\lambda = 0.75$ . Compared to the single phase flow, the presence of a liquid-liquid interface altered significantly the overall fluid dynamics of the system. Regardless of the value of  $\lambda$ , the volume flowrate across the channel section increased, indicating a significant turbulence reduction due to the conversion of the mean kinetic energy into potential energy at the deformed liquid-liquid interface (work is spent to deform the interface, where Korteweg force effects). These effects increased for decreasing  $\lambda$ .

Compared to a single phase flow at the same shear Reynolds number ( $Re_\tau = 100$ ), in the two phase flow case we observed a decrease of the wall-shear stress and a strong turbulence modulation in particular in the proximity of the interface.

We focused more closely on the interaction between the interface dynamics and the near wall turbulence, in particular, we find that the modulation of turbulence induced by the liquid-liquid interface is so important that wall shear stress inversions and local recirculation regions can be observed. These findings have been properly quantified and have been linked to the topology of the flow and of the deformed interface. The liquid-liquid interface interact with the near-wall turbulence structures modifying them. These modifications can be quantified considering the Probability Density Function (PDF) of the wall shear stress at the top wall, large positive fluctuations are inhibited whereas large negative fluctuations are promoted. The increased probability of negative fluctuations determine the presence of recirculations, regions characterized by a local value of the wall shear stress  $\tau_w$  that changes sign compared to the mean value measured at that wall. These events are strongly correlated with the interface elevation as shown by the joint probability density function of wall shear stress and interface elevation. The observed results depend primarily on the interface deformability and on the viscosity ratio between the two fluids ( $\lambda$ ).

Furthermore direct numerical simulation applied to analyze the weak turbulence theory in capillary wave turbulence, after flow reaches to steady state computed wave spectrum was in agreement with the predicted wave turbulence, these numerical results confirms two dimensional wavenumber spectrum interface is deforming in anisotropic turbulence.

---

## Conclusions and future work

The major topic of this thesis is study of Direct Numerical Simulation (DNS) for turbulent Poiseuille flow. A thin low viscosity layer flows on the top of a thick fluid layer. The two liquids are separated by a deformable interface and flow in a rectangular channel. The layers have matched density,  $\rho_1 = \rho_2$ , but different viscosity  $\nu_1 \neq \nu_2$ . We consider three different values of the viscosity ratio  $\lambda = \nu_1/\nu_2$ :  $\lambda = 1$ ,  $\lambda = 0.875$  and  $\lambda = 0.75$ . Simulations are run at a reference Reynolds number  $Re_\tau = 100$  (defined based on the physical properties of fluid 2, i.e. the thicker fluid layer), leading to a fully developed turbulent flow; namely the bulk Reynolds number based on the mean flow velocity  $u_b$  is  $Re_b = 2u_b h/\nu = 2500$ ; and for the two phase system (distribution of  $\phi$ ) initializing the order parameter such that the interface is initially located close to the upper boundary ( $h_2/h_1 = 9$ ); turbulence adjusts to the new physical configuration (transient behaviour) and finally reaches a new statistically steady state condition; after a statistically steady state condition is reached, results are collected for a long enough time window to ensure statistical convergence of the results. Numerical Simulations are based on a Phase Field Method (PFM) approach to track the interface position and describe the spatial and temporal evolution of it.

Compared to the single phase flow, the presence of a liquid-liquid interface altered significantly the overall fluid dynamics of the system. Regardless of the value of  $\lambda$ , the volume flowrate across the channel section increased, indicating a significant turbulence reduction due to the conversion of the mean kinetic energy into potential energy at the deformed liquid-liquid interface (work is spent to deform the interface). These effects increased for decreasing  $\lambda$ .

The presence of a liquid-liquid interface altered significantly the overall fluid dynamics of the system. For all the values of  $\lambda$  tested, an increase of the flow rate of the thicker layer is observed. The liquid-liquid interface in-

teract with the near-wall turbulence structures modifying them . These modifications can be quantified considering the Probability Density Function (PDF) of the wall shear stress at the top wall, large positive fluctuations are inhibited whereas large negative fluctuations are promoted. The increased probability of negative fluctuations determine the presence of recirculations, regions characterized by a local value of the wall shear stress  $\tau_w$  that changes sign compared to the mean value measured at that wall. These events are strongly correlated with the interface elevation as shown by the joint probability density function of wall shear stress and interface elevation.

Presented results is also important to understand nonlinear wave dynamics within a two-layer fluid with the study of Weak Turbulence Theory (WTT) of capillary waves. The main objective of this investigation was to obtain a clear development of the power-law spectrum, while a direct comparison is consistent with the theoretical value. It also opens new challenge in order to better understand wave turbulence and the influence of the oil and water flow.

The stronger effect on the flow field in the liquid-liquid flow is due to the present of the interface. However, changing the viscosity ratio (even only slightly) has definitely a non-negligible effect. Note that simulating smaller value of  $\lambda$  ( $\lambda \propto 10^{-1} \div 10^{-3}$ ) would require large computational resources (the local Reynolds number increases for decreasing  $\lambda$ ) that at present cannot be afforded. We believe that this is the first 3D Direct Numerical Simulation on the present issue, and serves as a proof of concept. In the future we plan to extend the present study to larger values of  $\lambda$  to investigate more accurately the role played by viscosity in the dynamics of a liquid-liquid confined flow. Note that one of the main objective of this thesis was to evaluate the influence of the liquid-liquid interface (characterized by a given surface tension) and of the viscosity ratio on the average properties of the flow (chiefly the mass flowrate and the skin friction). To achieve this goal, we have also shown the influence of the interface surface tension  $\sigma$  on the average strain, vorticity and velocity fluctuations and the interaction between the interface dynamics and the near wall turbulence. (in Chap. 4). Obtaining accurate estimates for the relative importance of the different terms of the Navier-Stokes equations is very important to understand the dynamics of turbulent transport in a liquid-liquid channel flow. This will be the subject of a future work, in which Turbulent Kinetic Energy (TKE) budgets will be computed and discussed to evaluate the contribution of the different terms of Navier-Stokes into the overall energy balance.

---

# A

## Appendix A

### A.1 Aliasing errors

Such errors has bee discussed first time by [79] which called  $\frac{2}{3}$  in numerical turbulence studies. For partial differential equations, for non-linear terms high frequency will be created and for NS equations this these terms called convective are of quadratic order, we follow the methods explained by [105] if we consider a product between two functions  $u$  and  $v$ . By transforming to Chebyshev space  $N^{th}$  order will be:

$$U_j = \sum_{m=0}^N \hat{u}_m T_m(x_j) \leq j \leq N \quad (\text{A.1})$$

$$V_j = \sum_{n=0}^N \hat{v}_n T_n(x_j)$$

By following Gauss-Lobatto grid rules:

$$x_j = \cos(\pi j N), \quad T_m(x_j) = \cos(m\pi j/N) \quad (\text{A.2})$$

Then for product term  $Z_j = U_j \Delta V_j$  Chebyshev expansion will be:

$$\hat{z}_k = \frac{1}{\gamma_k} \sum_{j=0}^N Z_j T_k(x_j) w_j, \quad (\text{A.3})$$

Where Eq. (A.3) is a convolution sum, If we normalized factors after weighting it gives:

$$w_j = \begin{cases} \pi/2N & j = 0, N \\ \pi/N & 1 \leq j \leq N-1 \end{cases} \quad \gamma_k = \begin{cases} \pi & k = 0, N \\ \pi/2 & 1 \leq k \leq N-1 \end{cases} \quad (\text{A.4})$$

By substituting Eq. (A.1) into Eq. (A.3) it reads:

$$\begin{aligned} \hat{z}_k &= \frac{1}{\gamma_k} \sum_{j=0}^N \sum_{m=0}^N \sum_{n=0}^N \hat{u}_m T_m(x_j) \hat{v}_n T_n(x_j) T_k(x_j) w_j \\ &= \frac{1}{4\gamma_k} \sum_{j=0}^N w_j \sum_{m=0}^N \sum_{n=0}^N \hat{u}_m \hat{v}_n \cos(a_j(m-n+k)) + \cos(a_j(m-n-k)) \\ &\quad + \cos(a_j(m-n+k)) + \cos(a_j(m+n+k)) + \cos(a_j(m+n-k)), \end{aligned} \quad (\text{A.5})$$

Where  $a_j = \pi j/N$ , orthogonality properties of Chebyshev Polynomials gives:

$$\frac{1}{N+1} \sum_{j=0}^N T_p(x_j) = \frac{1}{N+1} \sum_{j=0}^N \cos(\pi j/N) = \begin{cases} 1 & \text{if } p = 2Nm \quad m = 0, \pm 1 \\ 0 & \text{else} \end{cases} \quad (\text{A.6})$$

Then Eq. (A.5) leads to:

$$\begin{aligned} \hat{z}_k &= \frac{\pi}{4\gamma_k} \left[ \sum_{m-n+k=0} \hat{u}_m \hat{v}_n + \sum_{m-n-k=0} \hat{u}_m \hat{v}_n + \sum_{m-n-k=0} \hat{u}_m \hat{v}_n + \right. \\ &\quad \left. \sum_{m+n-k=0} \hat{u}_m \hat{v}_n \right] + \left[ \sum_{m-n+k=2NP} \hat{u}_m \hat{v}_n + \sum_{m-n-k=2NP} \hat{u}_m \hat{v}_n + \right. \\ &\quad \left. \sum_{m-n-k=2NP} \hat{u}_m \hat{v}_n + \sum_{m+n+k=2NP} \hat{u}_m \hat{v}_n \right] \end{aligned} \quad (\text{A.7})$$

Here,  $p = 0, \pm 1, \dots$  if you look at Eq. (A.7) the second pair inside bracket are aliasing errors, we are looking for minimum  $M$  to choose high frequency number to zero, for instance if  $m+n+k = 2M$ , regarding to when  $m = n = k$  will be worse case, the best value for  $k$  is locating outside the useful range, so  $k = N + 1$ .

In conclusion, a convenient value of  $M$  for eliminating alias term in pseudospectral method is:

$$M \geq \frac{3(N+1)}{2} - 1 \quad (\text{A.8})$$

which in this kind of transformation from physical space only  $M = 3(N + 1)/2 - 1$  points are chosen but only  $N$  chebyshev modes are keeping in spectral space, and the rest will be padded with zero, which called de-aliasing technique and is sometimes referred to as the 2/3-rule. By computing derivative of coefficients of product in Chebyshev Space:

$$Z'(x_j) = \sum_m^N \hat{z}_m^{(1)} T_m(x_j)$$

Actually, derivative in Chebyshev mode will follows [18], if you look at last formula above we have:

$$\hat{z}_m^{(1)} = \frac{2}{c_m} \sum_{\substack{p=m+1 \\ p+m \text{ odd}}} p \hat{z}_p, \quad c_m = \begin{cases} 2 & \text{if } m = 0 \\ 1 & \text{else} \end{cases} \quad (\text{A.9})$$

When we take derivative orders will decreased in a recurrence relation, which means chebyshev truncation and interpolation do not commute with differentiation [18], so after applying 3/2 rule when data passed to spectral space truncation should be used, which preventing coefficients that cause aliasing in the range of  $N + 1 \leq k \leq M$  from useful range:  $0 \leq k \leq N$ .



---

# B

## Publications, courses and projects

### B.1 Referred Journals

- J1 **Ahmadi, S.**, Roccon, A. , Zonta, F. and Soldati, A. (2016). Turbulent drag reduction in channel flow with viscosity stratified fluids, *Computers & Fluids*, [3].
- J2 **Ahmadi, S.**, Roccon, A. , Zonta, F. and Soldati, A.(2017). Turbulent drag reduction by a near wall surface tension active interface *Flow, Turbulence and Combustion* (submitted).

### B.2 Referred Conferences

- C4 Ahmadi, S., Roccon, A., Zonta, F. and **Soldati A.<sup>†</sup>**, (2017) Turbulence annihilation in surface tension stratified flow. *APS-DFD Annual Meeting*, Denver (CO, USA), November 19-21, 2017.
- C3 Ahmadi, S., Roccon, A., Zonta, F. and **Soldati A.<sup>†</sup>**, (2016) Viscosity stratified fluids in turbulent channel flow. *APS-DFD Annual Meeting*, Portland (OR, USA), November 20-22, 2016.
- C2 **Ahmadi, S.<sup>†</sup>**, Roccon, A., Zonta, F. and Soldati A., (2016) Effects of viscosity stratified fluids on turbulent channel flow. *ERCOFTAC ADA Pilot Centre Meeting*, Linz (Austria), November 11, 2016.
- C1 **Ahmadi, S.<sup>†</sup>**, Roccon, A., Zonta, F. and Soldati A., (2016) Turbulent modulation in double layer multiphase flow. *International Conference on Multiphase Flow*, Florence (Italy), May 22-27, 2016.

## B.3 Advanced Courses

- A5 **Wall-Bounded Turbulence**, International Centre for Mechanical Sciences (CISM), Udine (Italy), July, 2016. Coordinated by: Prof. S. Pirozzoli (Sapienza University of Rome, Roma, Italy).
- A4 **Small Scale Modeling and Simulation of Turbulent Multi-phase Flows**, International Centre for Mechanical Sciences (CISM), Udine (Italy), May, 2016. Coordinated by: Prof. S. Vincent (Paris-Est Marne-La-Vallée University, Marne-La-Vallée, France) and Prof. J. L. Estivalezes (ONERA, Toulouse, France).
- A3 **Mixing and Dispersion in Flows Dominated by Rotation and Buoyancy**, International Centre for Mechanical Sciences (CISM), Udine (Italy), July, 2015. Coordinated by: Prof. G. J. van Heijst (Eindhoven University of Technology, The Netherlands) and Prof. H. Clercx (Eindhoven University of Technology, The Netherlands).
- A2 **Dynamic of Bubbly flows**, International Centre for Mechanical Sciences (CISM), Udine (Italy), June, 2015. Coordinated by: Prof. F. Risso (CNRS and Université de Toulouse, France) and Prof. C. Sun (University of Twente, The Netherlands).
- A1 **Simulation of dispersed flows at the particle level**, University of Udine, Udine (Italy), December, 2015. Coordinated by: Prof. J. Derksen (University of Aberdeen, United Kingdom).

---

# Bibliography

- [1] R. Adrian. Hairpin vortex organization in wall turbulence a. *Phys. Fluids A*, 19(4):041301, 2007.
- [2] R. Adrian and Z. Liu. Observation of vortex packets in direct numerical simulation of fully turbulent channel flow. *J. Visualization*, 5(1):9–19, 2002.
- [3] S. Ahmadi, A. Roccon, F. Zonta, and A. Soldati. Turbulent drag reduction in channel flow with viscosity stratified fluids. *Comput. Fluids*, 2016.
- [4] D. M. Anderson, G. B. McFadden, and A. A. Wheeler. Diffuse-interface methods in fluid mechanics. *Annu. Rev. Fluid Mech.*, 30(1):139–165, 1998.
- [5] Q. Aubourg and N. Mordant. Nonlocal resonances in weak turbulence of gravity-capillary waves. *Phys. Rev. Lett.*, 114(14):144501, 2015.
- [6] V. E. Badalassi, H. D. Cenicerros, and S. Banerjee. Computation of multiphase systems with phase field models. *J. Comput. Phys.*, 190(2):371–397, 2003.
- [7] R. Bai, K. Chen, and D. D. Joseph. Lubricated pipelining: stability of core—annular flow. part 5. experiments and comparison with theory. *J. Fluid Mech.*, 240:97–132, 1992.
- [8] M. Berhanu and E. Falcon. Space-time-resolved capillary wave turbulence. *Phys. Rev. E*, 87(3):033003, 2013.
- [9] P. Bernard, J. Thomas, and R. Handler. Vortex dynamics and the production of reynolds stress. *J. Fluid Mech.*, 253:385–419, 1993.
- [10] P. J. Blennerhassett. On the generation of waves by wind. *Philosophical Transactions of the Royal Society of London. Series A*, 298:451–494, 1980.
- [11] W. J. Boettinger, J. Warren, C. Beckermann, and A. Karma. Phase-field simulation of solidification. *Annu. Rev. Mater. Res.*, 32(1):163–194, 2002.

- [12] D. Bogard and W. Tiederman. Burst detection with single-point velocity measurements. *J. Fluid Mech.*, 162:389–413, 1986.
- [13] J. Boyd. *Chebyshev and Fourier spectral methods*. Courier Corporation, 2001.
- [14] A. Bray. Theory of phase-ordering kinetics. *Adv. Phys.*, 51(2):481–587, 2002.
- [15] M. Brazhnikov, G. Kolmakov, A. Levchenko, and L. Mezhov-Deglin. Observation of capillary turbulence on the water surface in a wide range of frequencies. *EPL (Europhys. Lett)*, 58(4):510, 2002.
- [16] J. W. Cahn and J. E. Hilliard. Free energy of a nonuniform system. i. interfacial free energy. *J. Chem. Phys.*, 28(2):258–267, 1958.
- [17] J. W. Cahn and J. E. Hilliard. Free energy of a nonuniform system. iii. nucleation in a two-component incompressible fluid. *J. Chem. Phys.*, 31(3):688–699, 1959.
- [18] C. Canuto, M. Hussaini, A. M. Quarteroni, A. Thomas Jr, et al. *Spectral methods in fluid dynamics*. Springer Science & Business Media, 2012.
- [19] A. Celani, A. Mazzino, P. Muratore-Ginanneschi, and L. Vozella. Phase-field model for the rayleigh–taylor instability of immiscible fluids. *J. Fluid Mech.*, 622:115–134, 2009.
- [20] R. Chella and J. Viñals. Mixing of a two-phase fluid by cavity flow. *Phys. Rev. E*, 53(4):3832, 1996.
- [21] K. Chen, R. Bai, and D. D. Joseph. Lubricated pipelining. part 3 stability of core-annular flow in vertical pipes. *J. Fluid Mech.*, 214:251–286, 1990.
- [22] L. Chen. Phase-field models for microstructure evolution. *Annu. Rev. Mater. Res.*, 32(1):113–140, 2002.
- [23] L. Chen and J. Shen. Applications of semi-implicit fourier-spectral method to phase field equations. *Comput. Phys. Commun.*, 108(2-3):147–158, 1998.
- [24] K. Cheng, C. Wang, S. Wise, and X. Yue. A second-order, weakly energy-stable pseudo-spectral scheme for the cahn–hilliard equation and its solution by the homogeneous linear iteration method. *J. Sci. Comput.*, 69(3):1083–1114, 2016.

- [25] L. Deike, M. Berhanu, and E. Falcon. Energy flux measurement from the dissipated energy in capillary wave turbulence. *Phys. Rev. E*, 89(2):023003, 2014.
- [26] L. Deike, D. Fuster, M. Berhanu, and E. Falcon. Direct numerical simulations of capillary wave turbulence. *Phys. Rev. Lett.*, 112(23):234501, 2014.
- [27] P. Denissenko, S. Lukaschuk, and S. Nazarenko. Gravity wave turbulence in a laboratory flume. *Phys. Rev. Lett.*, 99(1):014501, 2007.
- [28] S. Dong and J. Shen. A time-stepping scheme involving constant coefficient matrices for phase-field simulations of two-phase incompressible flows with large density ratios. *J. Comput. Phys.*, 231(17):5788–5804, 2012.
- [29] D. Eyre. Unconditionally gradient stable time marching the cahn-hilliard equation. *MRS Online Proceedings Library Archive*, 529, 1998.
- [30] E. Falcon, C. Laroche, and S. Fauve. Observation of gravity-capillary wave turbulence. *Phys. Rev. Lett.*, 98(9):094503, 2007.
- [31] H. Fasel. Investigation of the stability of boundary layers by a finite-difference model of the navier—stokes equations. *J. Fluid Mech.*, 78(2):355–383, 1976.
- [32] P. Fischer and A. Patera. Parallel simulation of viscous incompressible flows. *Annu. Rev. Fluid Mech.*, 26(1):483–527, 1994.
- [33] D. Gottlieb and S. Orszag. *Numerical analysis of spectral methods: theory and applications*. SIAM, 1977.
- [34] R. Guo and Y. Xu. Efficient solvers of discontinuous galerkin discretization for the cahn–hilliard equations. *J. Sci. Comput.*, 58(2):380–408, 2014.
- [35] J. Hamilton, J. Kim, and F. Waleffe. Regeneration mechanisms of near-wall turbulence structures. *J. Fluid Mech.*, 287:317–348, 1995.
- [36] E. Herbert, N. Mordant, and E. Falcon. Observation of the nonlinear dispersion relation and spatial statistics of wave turbulence on the surface of a fluid. *Phys. Rev. Lett.*, 105(14):144502, 2010.
- [37] J. Hinze. 0. 1975 turbulence, 1938.

- [38] H. H. Hu, T. S. Lundgren, and D. D. Joseph. Stability of core-annular flow with a small viscosity ratio. *Phys. Fluids A: Fluid Dynamics (1989-1993)*, 2(11):1945–1954, 1990.
- [39] J. Isaac and J. Speed. Method of piping fluids, 1904. US Patent 759,374.
- [40] D. Jacqmin. Calculation of two-phase navier–stokes flows using phase-field modeling. *J. Comput. Phys.*, 155(1):96–127, 1999.
- [41] U. Jeng, L. Esibov, L. Crow, and A. Steyerl. Viscosity effect on capillary waves at liquid interfaces. *J. Phys.: Condens. Matter*, 10(23):4955, 1998.
- [42] J. Jiménez and P. Moin. The minimal flow unit in near-wall turbulence. *J. Fluid Mech.*, 225:213–240, 1991.
- [43] J. Jiménez and A. Pinelli. The autonomous cycle of near-wall turbulence. *J. Fluid Mech.*, 389:335–359, 1999.
- [44] D. Joseph and Y. Renardy. *Fundamentals of Two-fluid Dynamics: Lubricated transport, drops, and miscible liquids*. Springer-Verlag, 1993.
- [45] D. D. Joseph, M. Renardy, and Y. Renardy. Instability of the flow of two immiscible liquids with different viscosities in a pipe. *J. Fluid Mech.*, 141:309–317, 1984.
- [46] T. W. Kao and C. Park. Experimental investigations of the stability of channel flows. part 2. two-layered co-current flow in a rectangular channel. *J. Fluid Mech.*, 52:401–423, 1972.
- [47] V. V. Khataavkar, P. D. Anderson, and H. E. H. Meijer. On scaling of diffuse–interface models. *Chem. Eng. Sci.*, 61(8):2364–2378, 2006.
- [48] J. Kim. A numerical method for the cahn–hilliard equation with a variable mobility. *Commun. Nonlinear Sci. Numer. Simul.*, 12(8):1560–1571, 2007.
- [49] J. Kim. Phase-Field Models for Multi-Component Fluid Flows. *Comm. Comput. Phys.*, 12(3):613–661, 2012.
- [50] J. Kim, K. Kang, and J. Lowengrub. Conservative multigrid methods for cahn–hilliard fluids. *J. Comput. Phys.*, 193(2):511–543, 2004.
- [51] J. Kim, P. Moin, and R. Moser. Turbulence statistics in fully developed channel flow at low reynolds number. *J. Fluid Mech.*, 177:133–166, 1987.

- [52] S. Kline, W. Reynolds, F. Schraub, and P. Runstadler. The structure of turbulent boundary layers. *J. Fluid Mech.*, 30(4):741–773, 1967.
- [53] G. Kolmakov, A. Levchenko, M. Brazhnikov, L. Mezhov-Deglin, A. Silchenko, and P. McClintock. Quasiadiabatic decay of capillary turbulence on the charged surface of liquid hydrogen. *Phys. Rev. Lett.*, 93(7):074501, 2004.
- [54] S. Komori, R. Kurose, K. Iwano, T. Ukai, and N. Suzuki. Direct numerical simulation of wind-driven turbulence and scalar transfer at sheared gas–liquid interfaces. *J. Turbul.*, 11:1–20, 2010.
- [55] D. Korteweg. Sur la forme que prennent les équations du mouvements des fluides si l’on tient compte des forces capillaires causées par des variations de densité considérables mais connues et sur la théorie de la capillarité dans l’hypothèse d’une variation continue de la densité. *Archives Néerlandaises des Sciences exactes et naturelles*, 6:1–24, 1901.
- [56] T. Korvola, A. Kupiainen, and J. Taskinen. Anomalous scaling for three-dimensional cahn-hilliard fronts. *Communications on Pure and Applied Mathematics*, 58(8):1077–1115, 2005.
- [57] I. Kostin, M. Marion, R. Texier-Picard, and V. Volpert. Modelling of miscible liquids with the korteweg stress. *ESAIM: Mathematical Modelling and Numerical Analysis*, 37(5):741–753, 2003.
- [58] C. Kouris and J. Tsamopoulos. Dynamics of axisymmetric core-annular flow in a straight tube. i. the more viscous fluid in the core, bamboo waves. *Phys. Fluids (1994-present)*, 13(4):841–858, 2001.
- [59] H. Ku, R. Hirsh, and T. Taylor. A pseudospectral method for solution of the three-dimensional incompressible navier-stokes equations. *J. Comput. Phys.*, 70(2):439–462, 1987.
- [60] H. Lamb. *Hydrodynamics*. Cambridge university press, 1932.
- [61] A. Lamorgese, R. Mauri, and L. Sagis. Modeling soft interface dominated systems: A comparison of phase field and gibbs dividing surface models. *Physics Reports*, 675:1–54, 2017.
- [62] A. G. Lamorgese, D. Molin, and R. Mauri. Phase field approach to multiphase flow modeling. *Milan Journal of Mathematics*, 79(2):597–642, 2011.

- [63] P. Leo, J. Lowengrub, and H. Jou. A diffuse interface model for microstructural evolution in elastically stressed solids. *Acta Mater.*, 46(6):2113–2130, 1998.
- [64] V. Levich. *Physicochemical hydrodynamics*. Prentice hall, 1962.
- [65] J. Li and Y. Renardy. Direct simulation of unsteady axisymmetric core–annular flow with high viscosity ratio. *J. Fluid Mech.*, 391:123–149, 1999.
- [66] M. Lin, C. Moeng, W. Tsai, P. Sullivan, and S. Belcher. Direct numerical simulation of wind-wave generation processes. *J. Fluid Mech.*, 616:1–30, 2008.
- [67] M. Lin, C. Moeng, W. Tsai, P. P. Sullivan, and S. E. Belcher. Direct numerical simulation of wind-wave generation processes. *J. Fluid Mech.*, 616:1–30, 2008.
- [68] M. Looman. Method of conveying oil., 1916. US Patent 1,192,438.
- [69] J. Lowengrub and L. Truskinovsky. Quasi-incompressible cahn–hilliard fluids and topological transitions. In *Proceedings of the Royal Society of London A: Mathematical, Physical and Engineering Sciences*, volume 454, pages 2617–2654. The Royal Society, 1998.
- [70] S. Lukaschuk, S. Nazarenko, S. McLelland, and P. Denissenko. Gravity wave turbulence in wave tanks: space and time statistics. *Phys. Rev. Lett.*, 103(4):044501, 2009.
- [71] F. Magaletti, F. Picano, M. Chinappi, L. Marino, and C. M. Casciola. The sharp-interface limit of the cahn–hilliard/navier–stokes model for binary fluids. *J. Fluid Mech.*, 714:95–126, 2013.
- [72] R. Mauri, R. Shinnar, and G. Triantafyllou. Spinodal decomposition in binary mixtures. *Phys. Rev. E.*, 53(3):2613, 1996.
- [73] P. Moin and J. Kim. On the numerical solution of time-dependent viscous incompressible fluid flows involving solid boundaries. *J. Comput. Phys.*, 35(3):381–392, 1980.
- [74] P. Moin and J. Kim. Numerical investigation of turbulent channel flow. *J. Fluid Mech.*, 118:341–377, 1982.
- [75] Y. Na and P. Moin. Direct numerical simulation of a separated turbulent boundary layer. *J. Fluid Mech.*, 370:175–201, 1998.

- [76] S. Nazarenko. *Wave turbulence*, volume 825. Springer Science & Business Media, 2011.
- [77] I. Nezu. Turbulence in open-channel flows. 1993.
- [78] R. Oliemans and G. Ooms. Core-annular flow of oil and water. *Multiphase science and technology*, 2(1-4), 1986.
- [79] S. Orszag. On the elimination of aliasing in finite-difference schemes by filtering high-wavenumber components. *J. Atmos. Sci.*, 28(6):1074–1074, 1971.
- [80] S. Orszag and M. Israeli. Numerical simulation of viscous incompressible flows. *Annu. Rev. Fluid Mech.*, 6(1):281–318, 1974.
- [81] J. Osher, Sand Sethian. Fronts propagating with curvature-dependent speed: algorithms based on hamilton-jacobi formulations. *J. Comput. Phys.*, 79(1):12–49, 1988.
- [82] S. Osher and R. Fedkiw. Level set methods: an overview and some recent results. *J. Comput. Phys.*, 169(2):463–502, 2001.
- [83] R. Panton. Overview of the self-sustaining mechanisms of wall turbulence. *Prog. Aerosp. Sci.*, 37(4):341–383, 2001.
- [84] D. Peng, B. Merriman, S. Osher, H. Zhao, and M. Kang. Fronts propagating with curvature-dependent speed: algorithms based on hamilton-jacobi formulation. *J. Comput. Phys.*, 155:410–438, 1999.
- [85] A. Perry and B. Fairlie. A study of turbulent boundary-layer separation and reattachment. *J. Fluid Mech.*, 69(4):657–672, 1975.
- [86] V. Polnikov. Numerical modeling of the constant flux spectra for surface gravity waves in a case of angular anisotropy. *Wave Motion*, 33(3):271–282, 2001.
- [87] A. Prosperetti. Motion of two superposed viscous fluids. *Phys. Fluids.*, 24(7):1217–1223, 1981.
- [88] A. Pushkarev and V. Zakharov. Turbulence of capillary waves. *Phys. Rev. Lett.*, 76(18):3320, 1996.
- [89] A. Pushkarev and V. E. Zakharov. Turbulence of capillary waves—theory and numerical simulation. *Physica D: Nonlinear Phenomena*, 135(1):98–116, 2000.

- 
- [90] M. Renardy and Y. Renardy. Derivation of amplitude equations and the analysis of sideband instabilities in two-layer flows. *Phys. Fluids A.*, 5:2738–2762, 1993.
- [91] S. Robinson. Coherent motions in the turbulent boundary layer. *Annu. Rev. Fluid Mech.*, 23(1):601–639, 1991.
- [92] R. Rogallo. An illiac program for the numerical simulation of homogeneous incompressible turbulence. 1977.
- [93] L. Scarbolo, F. Bianco, and A. Soldati. Coalescence and breakup of large droplets in turbulent channel flow. *Phys. Fluids*, 27:073302, 2015.
- [94] L. Scarbolo, D. Molin, P. Perlekar, M. Sbragaglia, A. Soldati, and F. Toschi. Unified framework for a side-by-side comparison of different multicomponent algorithms: Lattice boltzmann vs. phase field model. *J. Comput. Phys.*, 234:263–279, 2013.
- [95] L. Scarbolo and A. Soldati. Turbulence modulation across the interface of a large deformable drop. *J. Turbul.*, 14:27–43, 2013.
- [96] J. Shen. Efficient spectral-galerkin method ii. direct solvers of second- and fourth-order equations using chebyshev polynomials. *SIAM J. Sci. Comput*, 16(1):74–87, 1995.
- [97] J. Shen and X. Yang. Numerical approximations of allen-cahn and cahn-hilliard equations. *Discrete Contin. Dyn. Syst*, 28(4):1669–1691, 2010.
- [98] M. Skote and D. Henningson. Direct numerical simulation of a separated turbulent boundary layer. *J. Fluid Mech.*, 471:107–136, 2002.
- [99] C. Smith and S. Metzler. The characteristics of low-speed streaks in the near-wall region of a turbulent boundary layer. *J. Fluid Mech.*, 129:27–54, 1983.
- [100] M. Stiassnie, Y. Agnon, and L. Shemer. Fractal dimensions of random water surfaces. *Physica D: Nonlinear Phenomena*, 47(3):341–352, 1991.
- [101] Y. Y. Su and B. Khomami. Numerical solution of eigenvalue problems using spectral techniques. *J. Comput. Phys.*, 100:297–305, 1992.

- [102] M. Sussman, E. Fatemi, P. Smereka, and S. Osher. An improved level set method for incompressible two-phase flows. *Computers & Fluids*, 27(5):663–680, 1998.
- [103] S. Tardu. Characteristics of single and clusters of bursting events in the inner layer. *Exp. Fluids.*, 20(2):112–124, 1995.
- [104] Y. Toba. Local balance in the air-sea boundary processes. *J. Oceanogr.*, 29(5):209–220, 1973.
- [105] M. Uhlmann. *The need for de-aliasing in a Chebyshev pseudo-spectral method*. Potsdam Institute for Climate Impact Research, 2000.
- [106] J. van der Waals. Verhandel. konink. akad. weten. amsterdam (sect. 1); see rowlinson, js 1979 translation of jd van der waals’\the thermodynamic theory of capillarity under the hypothesis of a continuous variation of density.”. *J. Stat. Phys*, 20(197-244):3, 1893.
- [107] F. Waleffe. Hydrodynamic stability and turbulence: Beyond transients to a self-sustaining process. *Stud. Appl. Math.*, 95(3):319–343, 1995.
- [108] F. Waleffe. On a self-sustaining process in shear flows. *Phys. Fluids*, 9(4):883–900, 1997.
- [109] W. Wright, R. Budakian, and S. Putterman. Diffusing light photography of fully developed isotropic ripple turbulence. *Phys. Rev. Lett.*, 76(24):4528, 1996.
- [110] Y. Xia. A fully discrete stable discontinuous galerkin method for the thin film epitaxy problem without slope selection. *J. Comput. Phys.*, 280:248–260, 2015.
- [111] F. Xie, X. Zheng, M. Triantafyllou, Y. Constantinides, Y. Zheng, and G. Em Karniadakis. Direct numerical simulations of two-phase flow in an inclined pipe. *J. Fluid Mech.*, 825:189–207, 2017.
- [112] S. G. Yiantsios and B. G. Higgins. Linear stability of plane poiseuille flow of two superposed fluids. *Phys. Fluids*, 31:3225–3238, 1988.
- [113] P. Yue, J. J. Feng, C. Liu, and J. Shen. A diffuse-interface method for simulating two-phase flows of complex fluids. *J. Fluid Mech.*, 515:293–317, 2004.

- 
- [114] P. Yue, C. Zhou, and J. Feng. Spontaneous shrinkage of drops and mass conservation in phase-field simulations. *J. Comput. Phys.*, 223(1):1–9, 2007.
- [115] V. Zakharov and N. FILONENK. Energy spectrum for stochastic oscillations of surface of a liquid. *Doklady Akademii Nauk SSSR*, 170(6):1292, 1966.
- [116] V. Zakharov and N. Filonenko. Weak turbulence of capillary waves. *J. Appl. Mech. Tech. Phys.*, 8(5):37–40, 1967.
- [117] V. Zakharov, V. L’vov, and G. Falkovich. Kolmogorov spectra of turbulence i. wave turbulence. series in nonlinear dynamics. *Springer-Verlag, Berlin*, 10:22, 1992.
- [118] X. Zheng, H. Babae, S. Dong, C. Chrysostomidis, and G. Karniadakis. A phase-field method for 3D simulation of two-phase heat transfer. *Int. J. Heat Mass Transfer.*, 82:282–298, 2015.
- [119] F. Zonta, C. Marchioli, and A. Soldati. Modulation of turbulence in forced convection by temperature-dependent viscosity. *J. Fluid Mech.*, 697:150–174, 2012.
- [120] F. Zonta, M. Onorato, and A. Soldati. Turbulence and internal waves in stably-stratified channel flow with temperature-dependent fluid properties. *J. Fluid Mech.*, 697:175–203, 2012.
- [121] F. Zonta, M. Onorato, and A. Soldati. Decay of gravity-capillary waves in air/water sheared turbulence. *Int. J. Heat Fluid Flow*, 61:137–144, 2016.
- [122] F. Zonta, A. Soldati, and M. Onorato. Growth and spectra of gravity–capillary waves in countercurrent air/water turbulent flow. *J. Fluid Mech.*, 777:245–259, 2015.